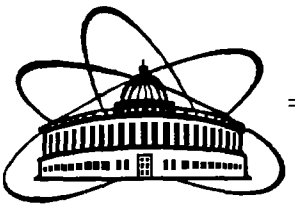

# ПИСЬМА В ЭЧАЯ

# PARTICLES AND NUCLEI, LETTERS

4[113]-2002



Издательский отдел ОИЯИ ДУБНА

JINR Publishing Department DUBNA

Объединенный институт ядерных исследований
Joint Institute for Nuclear Research

4[113]-2002

# ПИСЬМА О ФИЗИКЕ ЭЛЕМЕНТАРНЫХ ЧАСТИЦ И АТОМНОГО ЯДРА

# PHYSICS OF PARTICLES AND NUCLEI, LETTERS

Дубна 2002

В журнале *«Письма о физике элементарных частиц и атомного ядра»*, кратко — *«Письма в ЭЧАЯ»*, публикуются статьи, содержащие результаты оригинальных теоретических, экспериментальных, научно-технических, методических и прикладных исследований. Содержание публикуемых статей определяется тематикой научных исследований в ОИЯИ: теоретическая физика, физика элементарных частиц, релятивистская ядерная физика, физика атомного ядра и связанные вопросы общей физики, нейтронная физика, физика конденсированных сред, физика низких температур и криогенная техника, физика и техника ускорителей, методика физического эксперимента, компьютерные технологии в физике, прикладные работы по всем перечисленным разделам физики, включая радиобиологию, экологию и ядерную медицину.

Журнал зарегистрирован в Министерстве Российской Федерации по делам печати, телерадиовещания и средств массовых коммуникаций. Издателем журнала является Объединенный институт ядерных исследований. Журнал выходит шесть раз в год.

The journal *PHYSICS of PARTICLES and NUCLEI, LETTERS*, brief name *PARTICLES and NUCLEI, LETTERS*, publishes the articles with results of the original theoretical, experimental, scientific-technical, methodical and applied research. Subject-matter of articles covers the principal fields of research at JINR: theoretical physics, elementary particle physics, relativistic nuclear physics, nuclear physics and related problems in other branches of physics, neutron physics, condensed matter physics, physics and technique at low temperature, physics and technique of accelerators, physical experimental instruments and methods, physical computer experiments, applied research in these branches of physics and radiology, ecology and nuclear medicine.

The journal is registered in the Ministry of the Russian Federation for Press and is published bimonthly by the Joint Institute for Nuclear Research.

References to the articles of the *PHYSICS of PARTICLES and NUCLEI, LETTERS* should contain:

— names and initials of authors,
— title of journal,
— year of publication,
— publication index,
— page number.

For example:

*Alexeev G. D.* // Part. Nucl., Lett. 2000. No. 5[102]. P. 5.

## СОДЕРЖАНИЕ
## CONTENTS

Письма в ЭЧАЯ. 2002. №4[113] Particles and Nuclei, Letters. 2002. No.4[113]

УДК 539.172.12

# THERMAL MULTIFRAGMENTATION, NUCLEAR FOG AND CRITICAL TEMPERATURE FOR THE LIQUID–GAS PHASE TRANSITION

*V. A. Karnaukhov* [a1], *H. Oeschler* [b], *S. P. Avdeyev* [a], *E. V. Duginova* [a], *V. K. Rodionov* [a], *A. Budzanowski* [c], *W. Karcz* [c], *O. V. Bochkarev* [d], *E. A. Kuzmin* [d], *L. V. Chulkov* [d], *E. Norbeck* [e], *A. S. Botvina* [f]

[a] Joint Institute for Nuclear Research, Dubna

[b] Institut für Kernphysik, Darmstadt University of Technology, Darmstadt, Germany

[c] H. Niewodniczanski Institute of Nuclear Physics, Cracow, Poland

[d] Kurchatov Institute, Moscow

[e] University of Iowa, Iowa City, USA

[f] GSI, Darmstadt, Germany

Thermal multifragmentation of hot nuclei is interpreted as the nuclear liquid–fog phase transition. The charge distribution of the intermediate mass fragments produced in $p$ (8.1 GeV) + Au collisions is analyzed in the framework of the statistical multifragmentation model with the nuclear critical temperature for the liquid–gas phase transition $T_c$ as a free parameter. It is found (from the best fit of the calculations and data) that $T_c = (20 \pm 3)$ MeV (90 % CL).

Тепловая мультифрагментация горячих ядер интерпретируется как фазовый переход жидкость–туман в ядерном веществе. Зарядовое распределение фрагментов промежуточной массы, возникающих в соударениях $p$ (8,1 ГэВ) + Au, анализируется в рамках статистической модели мультифрагментации. При этом критическая температура для фазового перехода жидкость–газ $T_c$ используется в качестве свободного параметра. Из наилучшего согласия расчетов с экспериментом найдено, что $T_c = (20 \pm 3)$ МэВ (при уровне достоверности 90 %).

## 1. THE NUCLEAR EQUATION OF STATE AND THERMAL MULTIFRAGMENTATION

The investigation of the decay properties of the very hot nuclei is one of the most challenging topics of nowaday nuclear physics. The excitation energy of the hot nuclei (500–700 MeV) is comparable with the total binding energy. They disintegrate via a new multibody decay mode — thermal multifragmentation. This process is characterized by the copious emission of intermediate mass fragments (IMF, $2 < Z \leq 20$) which are heavier than alpha particles but lighter than fission fragments. Such multibody disintegration is not an exotic but the main decay channel of a very hot nuclear system.

The development of this field for the last two decades has been strongly stimulated by an idea that this process is related to the nuclear liquid–gas phase transition. One of the

[1] e-mail: karna@nusun.jinr.ru

first nuclear models, suggested by N. Bohr, K. Weizsäcker and Ya. I. Frenkel 65 years ago, is the liquid-drop model, which is alive now. The liquid–gas phase transition in the nuclear matter was predicted much later [1–3] on the basis of the similarity between van der Waals and nucleon–nucleon interactions. In both cases the attraction between particles is replaced by repulsion at a small interaction range. As a result, the equations of the state are similar for so different systems. It is well seen in the phase diagram (Fig. 1) taken from [2]. The figure shows the isotherms for pressure as a function of volume calculated for the van der Waals system and the Fermi gas of nucleons interacting through Skyrme forces. The scales are the same for both cases due to the use of dimensionless variables: pressure, volume and temperature are given as ratios to the critical values $P_c$, $V_c = 1/\rho_c$ ($\rho_c$ is the critical density) and $T_c$. The very steep part of the isotherms (on the left) corresponds to the liquid phase. The gas phase is presented by the right parts of the isotherms, where pressure is changing smoothly with increasing volume. A point of peculiar interest is the part of the diagram below the hatched line, where the isotherms correspond to negative compressibility. The density here is significantly reduced as compared to the liquid phase. This is a spinodal region characterized by the phase instability. One can imagine that a hot nucleus expands due to thermal pressure and enters into unstable region. Due to density fluctuations, a homogeneous system converts into the phase mixed state, consisting of droplets (IMFs) surrounded by nuclear gas (nucleons and light composite particles). In fact, the final state of this transition is a nuclear fog [3]. The neutrons fly away with the energies corresponding to the system temperature, while the charged particles are additionally accelerated in the Coulomb field of the system.

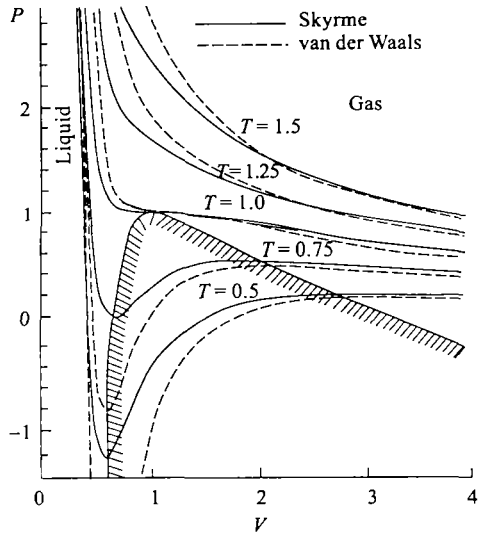


Fig. 1. Comparison of the equation of state for a van der Waals gas and for a nuclear system interacting through a Skyrme force (relative units are used)

An effective way to produce hot nuclei is collision of heavy ions with energies of up to hundreds of MeV per nucleon. But in this case heating of nuclei is accompanied by compression, strong rotation and shape distortion, which may essentially influence the decay properties of hot nuclei. One gains simplicity, and the picture becomes clearer when light relativistic projectiles (first of all, protons, antiprotons, pions) are used. In contrast to heavy ion collisions, fragments are emitted by the only source — the slowly moving target spectator. Its excitation energy is almost entirely thermal. Light relativistic projectiles provide therefore a unique possibility of investigating «thermal multifragmentation», which is governed by the thermodynamic properties of a hot nuclear system.

The disintegration time is determined by the time scale of the density fluctuations and is expected to be very short ($\approx$ 30 fm/$c$). This is a scenario of the thermal nuclear multifragmentation as a spinodal decomposition, considered in a number of theoretical and experimental papers (see, for example, [4–12] and review papers [13, 14]). It was proved experimentally

that thermal fragmentation takes place at reduced (3–4 times) density [15–17] and the decomposition time is short (less than 100 fm/$c$) [18–20]. The spinodal decomposition is, in fact, the liquid–fog phase transition in nuclear system.

## 2. THE CRITICAL TEMPERATURE FOR THE LIQUID–GAS PHASE TRANSITION

An important model parameter of this scenario is the critical temperature for the nuclear liquid–gas phase transition $T_c$ at which the isotherm in the phase diagram has an inflection point. The surface tension vanishes at $T_c$, and only the gas phase is possible above this temperature. There are many calculations of $T_c$ for finite nuclei. In Refs. [1,2,21,22], for example, it is done by using a Skyrme effective interaction and the thermal Hartree–Fock theory. The values of $T_c$ were found to be in the range 10–20 MeV depending on the chosen Skyrme interaction parameters and the details of the model. There are still no reliable experimental data for $T_c$, though this is claimed in a number of papers (see table).

**The experimental data on the critical temperature for nuclei**

| Ref. | [23] | [24] | [25] | [26] | [27] |
|---|---|---|---|---|---|
| $T_c$, MeV | $\sim 5$ | 11–12 | $6.7 \pm 0.2$ | $7.8 \pm 0.2$ | $> 10$ |
| Method | $Y(A_{\mathrm{IMF}})$, Fisher's model | | | | $\sigma_{\mathrm{fission}}(T)$ |

The main source of the experimental information for $T_c$ is the fragment yield. In some statistical models of nuclear multifragmentation the shape of the IMF charge (or mass) distribution $Y(Z)$ is sensitive to the ratio $T/T_c$. The charge distribution is well described by the power law $Y(Z) \sim Z^{-\tau}$ for a wide range of the colliding systems [28]. In earlier studies on multifragmentation [3,23] the power-law behavior of the IMF yield was interpreted as an indication of the proximity of the excited system to the critical point for the liquid–gas phase transition. This was stimulated by the application of Fisher's classical droplet model [29], which predicted a pure power-law droplet-size distribution with the minimal value of $\tau = 2-3$ at the critical point.

In Ref. [23] Hirsch et al. estimate $T_c$ to be $\sim 5$ MeV simply from the fact that the mass distribution is well described by a power law for IMFs produced in the collision of $p$ (80–350 GeV) with Kr and Xe targets. In fact, the fragment mass distribution is not exactly described by the power law, therefore Panagiotou et al. [24] suggested the use of the term $\tau_{\mathrm{app}}$, an apparent exponent, to stress that the exact power-law description takes place only at the critical temperature. In paper [24] the experimental data were gathered for different colliding systems to get the temperature dependence of $\tau_{\mathrm{app}}$. As a temperature, the inverse slope of the fragment energy spectra was taken in the range of the high-energy tail. The minimal value of $\tau_{\mathrm{app}}$ was obtained at $T = 11-12$ MeV, which was claimed as $T_c$. The later data smeared out this minimum. Moreover, it became clear that the «slope» temperature for fragments does not coincide with the thermodynamical one, which is several times smaller.

A more sophisticated use of Fisher's droplet model for the estimation of $T_c$ has been recently made by Elliott, Moretto et al. [25,26]. The model was modified by including

the Coulomb energy release when a particle moves from the liquid to the vapor. The multifragmentation data from the Indiana Silicon Sphere collaboration for $\pi(8\ \mathrm{GeV}/c) + \mathrm{Au}$ collisions were analyzed with this refined model [25]. The extracted critical temperature is $T_c = (6.7 \pm 0.2)$ MeV. In the recent paper [26] the same analysis technique is applied to the data for the multifragmentation in collisions of Au, La, Kr (at 1.0 GeV per nucleon) with a carbon target (EOS collaboration). The extracted values of $T_c$ are $(7.6 \pm 0.2)$, $(7.8 \pm 0.2)$ and $(8.1 \pm 0.2)$ MeV respectively.

There is only one paper in which $T_c$ is estimated by using data other than the fragmentation ones. In Ref. [27] it is done by the analysis of the temperature dependence of the fission probability for $^4\mathrm{He} + ^{184}\mathrm{W}$ collisions [30]. It was concluded that $T_c > 10$ MeV in contrast to the result of Refs. [25,26].

It should be noted that in some papers the term «critical temperature» is not used in the strict thermodynamical sense given above. In Ref. [31] multifragmentation in $\mathrm{Au} + \mathrm{Au}$ collisions at 35 $A$·MeV was analyzed with the so-called Campi plots to prove that the phase transition takes place in the spinodal region. The characteristic temperature for that process was denoted as $T_{\mathrm{crit}}$ and found to be equal to $(6.0 \pm 0.4)$ MeV. In the recent paper [32] the bond percolation model is used to interpret 10.2 GeV/$c$ $p + \mathrm{Au}$ multifragmentation data. The critical value of the percolation parameter $p_c = 0.65$ was found from the analysis of the IMF charge distribution. The corresponding «critical temperature» of $(8.3 \pm 0.2)$ MeV is estimated by using the model relation between the percolation control parameter «$p$» and the excitation energy. The more appropriate term for this particular temperature is «break-up» or «crack» temperature, as suggested in Ref. [33]. This temperature corresponds to onset of the fragmentation of the nucleus entering the phase coexistence region.

Having in mind the shortcomings of Fisher's model [34,35], we have made an attempt to estimate the critical temperature in the framework of the statistical multifragmentation model (SMM) [36].

## 3. ESTIMATION OF $T_c$ USING SMM

Within this model one considers a microcanonical ensemble of all break-up channels composed of nucleons and excited fragments of different masses. It is assumed that an excited nucleus expands to a certain volume and then breaks up into nucleons and hot fragments. It is also assumed that at the break-up time the nucleus is in thermal equilibrium characterized by the channel temperature $T$ determined from the energy balance. The probability $W_j$ of a decay channel $j$ is proportional to its statistical weight:

$$W_j \sim \exp S_j(E_x, A_0, Z_0), \tag{1}$$

where $S_j$ is the entropy of the system in a state corresponding to the decay channel $j$. The excitation energy, mass and charge of the decaying system are denoted by $E_x$, $A_0$ and $Z_0$, respectively. The fragments with mass number $A > 4$ are treated as heated nuclear liquid drops.

Channels are characterized by the multiplicities, $N_{AZ}$, of fragments ${}^AZ$. The channels

entropy is obtained by summing the entropies of all the particles in a given channel:

$$S_j = \sum N_{AZ} S_{AZ}, \quad S_{AZ} = -\left(\frac{\partial F_{AZ}}{\partial T}\right)_V. \tag{2}$$

The fragment free energy $F_{AZ}$ is a sum of volume, surface, symmetry, Coulomb and translational terms:

$$F_{AZ} = F^V_{AZ} + F^S_{AZ} + F^{\rm sym}_{AZ} + F^C_{AZ} + F^t_{AZ}. \tag{3}$$

The surface energy term, $F^S_{AZ}$, depends on the critical temperature, so the fragment charge distribution is sensitive to the value of $T_c$. The following expression is used in the SMM for $F^S_{AZ}$:

$$F^S_{AZ} = a_s(T)A^{2/3}, \quad a_s(T) = a_s(0)\left(\frac{T_c^2 - T^2}{T_c^2 + T^2}\right)^{5/4}, \tag{4}$$

with $a_s(T) = 4\pi r_0^2 \sigma(T)$, where $\sigma(T)$ — temperature-dependent coefficient of the surface tension. This equation was obtained in Ref. [38], devoted to the theoretical study of thermodynamical properties of a plane interface between two phases of nuclear matter (liquid and gas) in equilibrium. This parameterization is succesfully used by the SMM for describing the multifragment decay of hot finite nuclei.

The comparison of the measured and calculated fragment charge distributions is the way to estimate the critical temperature $T_c$.

Statistical model describes well the properties of the thermal fragmentation of the target spectators produced in the collision of the light relativistic ions. As an example, Fig. 2, *a* shows the measured by the FASA collaboration and calculated fragment charge distributions for collisions of $p$ (8.1 GeV), $^4$He (4 and 14.6 GeV) and $^{12}$C (22.4 GeV) with Au target. Experiments have been done using the $4\pi$-setup FASA installed at Dubna Synchrophasotron [12].

The reaction mechanism for the light relativistic projectiles is usually divided into two stages. The first one is a fast energy-depositing stage, during which very energetic light particles are emitted and a nuclear remnant is excited. We use the intranuclear cascade model (INC) [37] for describing the first stage. The second stage is described by the SMM, which considers multibody decay of a hot and expanded nucleus. But such a two-stage approach fails to explain the observed IMF multiplicities. An expansion stage is inserted between the two parts of the calculation. The excitation energies and the residual masses are then fine tuned [12] to get agreement with the measured IMF multiplicities, i.e., the values for the residual (after INC) masses and their excitation energies are scaled on an event-by-event basis. The lines in Fig. 2, *a* give the charge distributions calculated in the framework of this combined model, INC + Expansion + SMM, assuming $T_c = 18$ MeV. The agreement between the data and the model prediction is very good.

Figure 2, *b* shows the power-law fit of the distributions with the $\tau$ parameter given in the insert as a function of the beam energy. The corresponding thermal excitation energy range is 3–6 MeV/nucleon. The power-law parameter exhibits the so-called critical behavior showing a minimum at the excitation energy corresponding to the temperature three times lower than

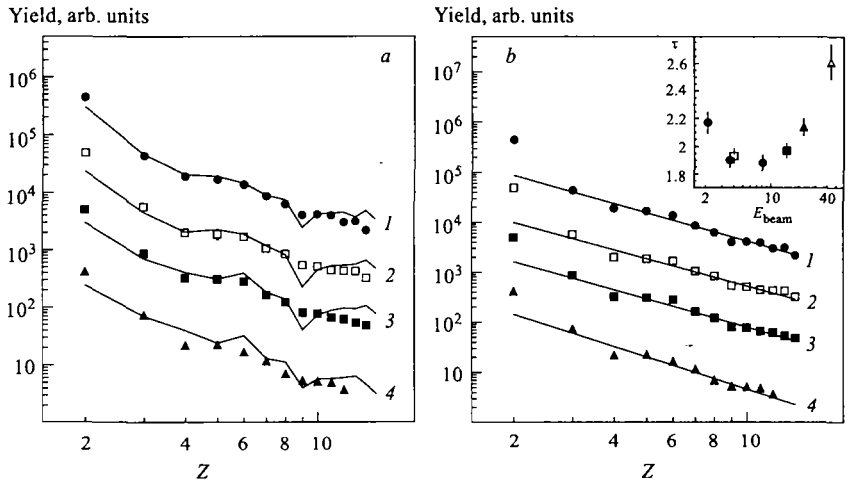


Fig. 2. Fragment charge distributions for $p$ + Au at 8.1 GeV (•, *1*), $^4$He + Au at 4 GeV (□, *2*), $^4$He + Au at 14.6 GeV (■, *3*) and $^{12}$C + Au at 22.4 GeV (▲, *4*): *a*) the lines are calculated by the INC + Exp. + SMM model (normalized at $Z = 3$); *b*) the power-law fits with $\tau$ parameters given in the insert as a function of beam energy (in GeV)

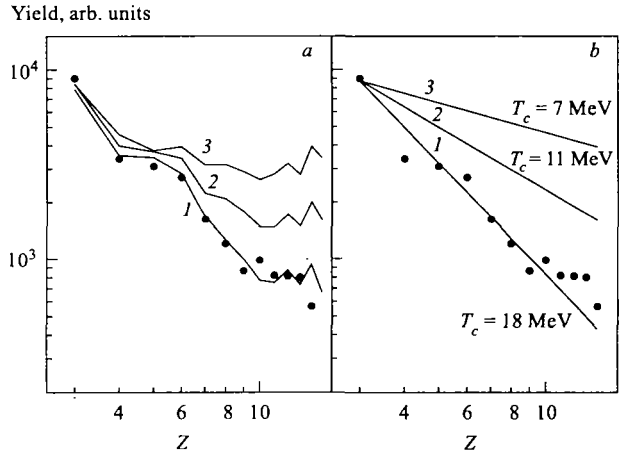


Fig. 3. Fragment charge distribution for $p$ + Au at 8.1 GeV (dots): *a*) the lines are calculated by the INC + Exp. + SMM model, assuming $T_c$ = 18 MeV (*1*), 11 MeV (*2*) and 7 MeV (*3*); *b*) the power-law fits

the assumed $T_c$. A conventional explanation of that is given in Ref. [12], so this minimum for $\tau$ has no relation to any criticality [28].

In the present paper the calculations are performed for $p$ (8.1 GeV) + Au collisions with $T_c$ as a free parameter. For all values of $T_c$ the calculations with the INC + Exp. + SMM model have been properly adjusted [12] to get the mean IMF multiplicity close to the measured

one. Figure 3, *a* shows the comparison of the measured fragment charge distribution and the model predictions for $T_c = 7$, 11 and 18 MeV. The statistical errors of the measurements do not exceed the size of the dots. The data are corrected for the counting rate loss caused by the cutoff ($\sim$ 1.2 MeV/nucleon) in the low-energy part of the IMF spectra. This correction is the largest ($\sim$ 15 %) for the heavier IMFs. The calculations are close to the data for $T_c = 18$ MeV. The estimated mean temperature of the fragmenting system is around 6 MeV, the mean charge and mass numbers are 67 and 158 respectively. The theoretical curves deviate from the data with decreasing $T_c$.

Figure 3, *b* gives the results of the power-law fits for the data and model calculations (in the range $Z = 3-11$). The Be yield was corrected in the fitting procedure for the loss of unstable $^8$Be. The final results are shown in Fig. 4. The measured power-law exponent is given as a band with a width determined by the statistical error. The size of the symbols for the calculated values of $\tau_{\rm app}$ is of the order of the error bar. From the best fit of the data and calculations one concludes that $T_c = (20 \pm 3)$ MeV at 90 % confidence level.

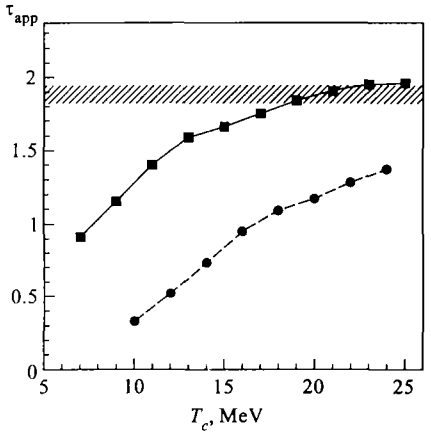


Fig. 4. The power-law exponent for $p$ (8.1 GeV) + Au collision. The band corresponds to the measured value and its error bar. The symbols are obtained by the power-law fits of IMF charge distributions calculated assuming different values of $T_c$ and different parametrization of the surface tension: squares are for Eq. (4), solid circles are for Eq. (5)

Figure 4 shows also the results of the calculations with $a_s(T)$ linearly dependent on $T/T_c$ [25,26]:

$$a_s(T) = a_s(0)\left(1 - \frac{T}{T_c}\right). \tag{5}$$

The calculated values of $\tau_{\rm app}$ in this case are remarkably lower than the measured one.

## CONCLUSION

Thermal multifragmentation of hot nuclei is interpreted as the liquid–fog phase transition. The critical temperature for the nuclear liquid–gas phase transition $T_c$ (at which surface tension vanishes) is estimated by using statistical multifragmentation model. For that purpose, the IMF charge distribution for $p$ + Au collisions at 8.1 GeV has been analyzed within the SMM with $T_c$ as a free parameter. The value $T_c = (20 \pm 3)$ MeV (90 % CL) obtained from the best fit to the data should be considered as some effective value of the critical temperature averaged over all the fragments produced in the collision. This value is significantly larger than those found in Refs. [25,26] by the analysis of the multifragmentation data in terms of Fisher's droplet formalism. Although our value for $T_c$ is model-dependent, as is any other estimate of the critical temperature, the analysis presented here provides strong support for a value of $T_c > 15$ MeV.

**Acknowledgments.** The authors are grateful to A. Hrynkiewicz, A. N. Sissakian, S. T. Belyaev, A. I. Malakhov, N. A. Russakovich for support and to A. V. Ignatyuk, I. N. Mishustin, V. D. Toneev, W. Reisdorf and ALADIN Workshop-2002 for illuminating discussions. The research was supported in part by Grant No. 00-02-16608 from the Russian Foundation for Basic Research, by the Grant of the Polish Plenipotentiary to JINR, by Grant NATO PST.CLG.976861, by Grant No. 1P03 12615 from the Polish State Committee for Scientific Research, by Contract No. 06DA453 with Bundesministerium für Forschung und Technologie, and by the US National Science Foundation.

REFERENCES

1. *Sauer G., Chandra H., Mosel U.* // Nucl. Phys. A. 1976. V. 264. P. 221.
2. *Jaqaman H., Mekjian A. Z., Zamick L.* // Phys. Rev. C. 1983. V. 27. P. 2782.
3. *Siemens P. J.* // Nature. 1983. V. 305. P. 410; Nucl. Phys. A. 1984. V. 428. P. 189c.
4. *Guarnera A. et al.* // XXXIII Winter Meeting on Nucl. Phys., Bormio, 1995; Preprint GANIL P95-05. Caen, 1995.
5. *Lee S. J., Mekjian A. Z.* // Phys. Rev. C. 1997. V. 56. P. 2621.
6. *Baran V. et al.* // Nucl. Phys. A. 1998. V. 632. P. 287.
7. *D'Agostino M. et al.* // Phys. Lett. B. 2000. V. 473. P. 219.
8. *Beaulieu L. et al.* // Phys. Rev. Lett. 2000. V. 84. P. 5971.
9. *Lopez O.* // Nucl. Phys. A. 2001. V. 685. P. 246c.
10. *Borderie B. et al.* // Phys. Rev. Lett. 2001. V. 86. P. 3252.
11. *Porile N. T. et al.* // Phys. Rev. C. 1989. V. 39. P. 1914.
12. *Avdeyev S. P. et al.* // Yad. Fiz. 2001. V. 64. P. 1628; Phys. At. Nucl. 2001. V. 64. P. 1549.
13. *Bonasera A. et al.* // La Rivista del Nuovo Cimento. 2000. V. 23. P. 1.
14. *Richert J., Wagner P.* // Phys. Rep. 2001. V. 350. P. 1.
15. *Bao-An Li et al.* // Phys. Lett. B. 1994. V. 335. P. 1.
16. *Avdeyev S. P. et al.* // Eur. Phys. J. A. 1998. V. 3. P. 75.
17. *Kwiatkowski K. et al.* // Phys. Rev. Lett. 1995. V. 74. P. 3756.
18. *Lips V. et al.* // Phys. Lett. B. 1994. V. 338. P. 141.
19. *Shmakov S. Yu. et al.* // Yad. Fiz. 1995. V. 58. P. 1735; Phys. At. Nucl. 1995. V. 58. P. 1635.
20. *Wang G. et al.* // Phys. Rev. C. 1996. V. 53. P. 1811;
    *Wang G. et al.* // Phys. Rev. C. 1998. V. 57. P. R2786.
21. *Bonche P. et al.* // Nucl. Phys. A. 1985. V. 436. P. 265.

22. *Feng-Shou Zhang* // Z. Phys. A. 1996. V.356. P.163.

23. *Hirsch A. S. et al.* // Phys. Rev. C. 1984. V.29. P.508.

24. *Panagiotou A. D., Curtin M. W., Scott D. K.* // Phys. Rev. C. 1985. V.31. P.55.

25. *Elliott J. B. et al.* // Phys. Rev. Lett. 2002. V.88. P.042701.

26. *Elliott J. B. et al.* nucl-ex /0205004v1. 2002.

27. *Karnaukhov V. A.* // Yad. Fiz. 1997. V.60. P.1780; Phys. At. Nucl. 1997. V.60. P.1625.

28. *Karnaukhov V. A. et al.* // Yad. Fiz. 1999. V.62. P.272; Phys. At. Nucl. 1999. V.62. P.237.

29. *Fisher M. E.* // Physics. 1967. V. 3. P. 255.

30. *Moretto L. G. et al.* // Phys. Lett. B. 1972. V.38. P.471.

31. *D'Agostino M. et al.* // Nucl. Phys. A. 1999. V.650. P.329.

32. *Kleine Berkenbusch M. et al.* // Phys. Rev. Lett. 2002. V.88. P.022701.

33. *Botvina A. S., Il'inov A. S., Mishustin I. N.* // Yad. Fiz. 1985. V.42. P.1127; Sov. J. Nucl. Phys. 1985. V.42. P.712;
*Bondorf J. et al.* // Nucl. Phys. A. 1985. V.444. P.460.

34. *Schmelzer J., Röpke G., Ludwig F.-P.* // Phys. Rev. C. 1997. V.55. P.1917.

35. *Reuter P. T., Bugaev K. A.* // Phys. Lett. B. 2001. V.517. P.233.

36. *Bondorf J. et al.* // Phys. Rep. 1995. V.257. P.133.

37. *Toneev V. D. et al.* // Nucl. Phys. A. 1990. V.519. P.463c;
*Amelin N. S. et al.* // Yad. Fiz. 1990. V.52. P.272.

38. *Ravenhall D. G., Pethick C. J., Lattimer J. M.* // Nucl. Phys. A. 1983. V.407. P.571.

Received on July 29, 2002.

Письма в ЭЧАЯ. 2002. №4[113] Particles and Nuclei, Letters. 2002. No.4[113]

УДК 530.145

# TOPOLOGICAL AND NONTOPOLOGICAL SOLUTIONS FOR THE CHIRAL BAG MODEL WITH CONSTITUENT QUARKS

*K. Sveshnikov* [a,b,1], *Il. Malakhov* [a], *M. Khalili* [a], *S. Fedorov* [a]

[a] Physics Department, Moscow State University, Moscow

[b] Institute of Theoretical Microphysics, Moscow State University, Moscow

The three-phase version of the hybrid chiral bag model, containing the phase of asymptotic freedom, the hadronization phase as well as the intermediate phase of constituent quarks, is proposed. For this model the self-consistent solutions of different topology are found in $(1+1)$D with due regard for fermion vacuum polarization effects. The renormalized total energy of the bag is studied as a function of its geometry and topological charge. It is shown that in the case of nonzero topological charge there exists a set of configurations being the local minima of the total energy of the bag and containing all the three phases, while in the nontopological case the minimum of the total energy of the bag corresponds to vanishing size of the phase of asymptotic freedom.

В данной работе предложен трехфазовый вариант гибридной киральной модели мешка, содержащий наряду с фазами асимптотической свободы и адронизации промежуточную фазу конституентных кварков. Для этой модели в $(1+1)$-мерном случае с учетом эффектов поляризации фермионного вакуума найдены самосогласованные решения с различной топологией. Изучена зависимость перенормированной полной энергии мешка от параметров, характеризующих его геометрию, и от его топологического заряда. Показано, что в случае ненулевого топологического заряда существует множество конфигураций, являющихся локальными минимумами полной энергии мешка и содержащих все три фазы, в то время как в нетопологическом случае минимум полной энергии мешка соответствует нулевому размеру фазы асимптотической свободы.

## INTRODUCTION

At present the models of quark bags [1–4] turn out to be one of the most perspective approaches to the study of the low-energy structure of baryons. The most promising results have been obtained within so-called hybrid chiral bag models (HCBM) [5–7], where asymptotically free massless quarks and gluons are confined in a chirally invariant way in a spatial volume, surrounded by the colorless purely mesonic phase, described by some nonlinear theory like the Skyrme model [8]. However, in such two-phase HCBM there is no place for massive constituent quarks, whose concept is one of the cornerstones in the hadronic spectroscopy [9]. From the last point of view the most attractive situation should be that in which first the initially free, almost massless current quarks transmute into «dressed», via interaction, massive constituent quarks carrying the same quantum numbers of color, flavor

[1] e-mail: costa@bog.msu.su

and spin, and only afterwards there emerges the purely mesonic colorless phase. The first step towards such a version of the bag is made in the three-phase chiral model, wherein the additional intermediate phase of interacting quarks and mesons with nonzero radial size is introduced [10, 11]. This model allows one to take self-consistently into account: i) the phase of asymptotic freedom with free massless quarks; ii) the phase of constituent quarks, which acquire an effective mass due to the chirally invariant interaction with the meson fields in the intermediate domain of finite size; iii) the hadronization phase, where the quark degrees of freedom are completely suppressed, while the nonlinear dynamics of meson fields leads to the appearance of the $c$-number boson condensate in the form of a classical soliton solution, which keeps up the topological nature of the model as well as the relevant quantum numbers.

It should be mentioned that the direct quark-meson interaction is also considered in a number of other approaches to the description of low-energy hadron structure, in particular, in the cloudy bag models [12–14], as well as in various versions of the chiral quark-soliton models [15–19]. However, the role of this interaction in each of these approaches is substantionally different. In the cloudy bag models such $\pi\bar{q}q$ coupling is treated only perturbatively, while in quark-soliton models it is considered as the main source for nonlinear dynamical generation of the quark bag structure in the whole space. In the case under consideration an intermediate variant takes place, where the contribution of the direct chiral quark-meson coupling to the properties of the system is nonperturbative, while the confinement of quarks is ensured by appropriate boundary conditions. Such an approach allows one to realize the nonlinear mechanism of dynamical mass generation in the intermediate domain, but, unlike the quark-soliton models, preserves the total confinement.

In the present paper a toy $(1 + 1)$D model of such kind is considered, in which in the intermediate domain the one-flavor fermion field is coupled in a chirally invariant way to the real scalar field, which possesses a nonlinear soliton solution in the exterior region. For this model the self-consistent solutions with different values of topological charge, namely 1, 2, and 0, are found with due regard for the fermion vacuum polarization effects. For these solutions the renormalized total energy of the bag is studied as a function of its geometry and topological charge. It is shown that for nonzero topological charge there exists a set of configurations being the local minima of the total energy of the bag and containing all the three phases, while in the nontopological case the minimum of the bag's energy corresponds to vanishing size of the phase of asymptotic freedom.

## 1. LAGRANGIAN AND EQUATIONS OF MOTION

The division of space into separate bag's phases is performed by means of a set of subsidiary fields $\theta(x)$, whose self-interaction is supposed to be strong enough to neglect the influence of the matter fields $\phi$ on the dynamics of $\theta$ to the leading order, and thereafter to use $\theta$ as background fields for the dynamics of $\phi$'s [10, 20]. One can obviously introduce as many fields $\theta(x)$ as needed with the appropriate self-interaction, which will determine an (almost) rectangular division of space into domains, corresponding to different phases. Note that in this approach the Lorentz covariance will be broken only spontaneously, on the level of solutions of equations of motion, so, in order to restore the broken Lorentz symmetry, one can freely use the framework of covariant group variables [21].

Within this framework, the model we consider is described by the following Lagrangian [10]:

$$\mathcal{L} = \bar{\psi} i\hat{\partial}\psi + \frac{1}{2}(\partial_\mu\varphi)^2 - \frac{1}{2}m_0^2\varphi^2\theta_{\mathrm{I}} - \frac{M}{2}\left[\bar{\psi}, \mathrm{e}^{ig\gamma_5\varphi}\psi\right]_- \theta_{\mathrm{II}} - \left(\frac{M_0}{2}\left[\bar{\psi}, \mathrm{e}^{ig\gamma_5\varphi}\psi\right]_- + V(\varphi)\right)\theta_{\mathrm{III}}, \tag{1.1}$$

with $\theta_{\mathrm{I}} = \theta(|x| < x_1)$, $\theta_{\mathrm{II}} = \theta(x_1 \leq |x| \leq x_2)$, $\theta_{\mathrm{III}} = \theta(|x| > x_2)$ being the step functions, which pick out the inner, intermediate and exterior bag's domains correspondingly, combined with the rule that upon the field variation all the surface terms, which should appear on the boundaries between domains, must be dropped. In (1.1) the vacuum pressure term $B$ is absent, although it is physically quite reasonable as taking account for the gluonic input to the bag structure. The reason is that in this model due to the existence of the intermediate phase the Dirac sea polarization behaves very specifically and itself produces the required «inward pressure», what is the main role of the $B$-term in the two-phase HCBM. Therefore we can drop it without serious loss of physical content, focusing attention mostly on fermion vacuum polarization effects.

To form the bag, we suppose $M_0$ to be very large, which leads to the dynamical suppression of fermions in the exterior domain III, and simultaneously take $m_0 \to \infty$, so the boson field vanishes in domain I. According to the general approach accepted in HCBM, the boson field is treated in the mean-field approximation, i.e., it is assumed to be a $c$-number field. Henceforth we shall consider the rest frame of the bag, where $\varphi(x)$ becomes a stationary classical background for fermions. In domain I we have $\varphi(x) = 0$, while in the bag's exterior $\varphi(x)$ decouples from fermions due to the infinite effective mass of the latters and is formed uniquely by the self-interaction $V(\varphi)$. We shall suppose that the self-interaction $V(\varphi)$ leads to soliton-like solutions of equations of motion and is an even function. Then the boson field could be either odd (the topological charge is nonzero) or even (the topological charge vanishes) function.

The equations of motion, following from (1.1), read:
in domain I

$$i\hat{\partial}\psi = 0, \tag{1.2a}$$

$$\varphi = 0, \tag{1.2b}$$

in domain II

$$\left(i\hat{\partial} - M\,\mathrm{e}^{ig\gamma_5\varphi}\right)\psi = 0, \tag{1.3a}$$

$$\varphi'' = ig\frac{M}{2}\langle\left[\bar{\psi}, \gamma_5\,\mathrm{e}^{ig\gamma_5\varphi}\psi\right]_-\rangle, \tag{1.3b}$$

and in domain III

$$\left(i\hat{\partial} - M_0\,\mathrm{e}^{ig\gamma_5\varphi}\right)\psi = 0, \tag{1.4a}$$

$$-\varphi'' + V'(\varphi) = 0, \tag{1.4b}$$

where $\langle\ \ \rangle$ in Eq. (1.3b) stands for the expectation value with respect to the fermionic state of the bag. To simplify calculations, we put further $g = 1$, because the dependence on it can be easily restored by means of the substitution $\varphi \to \varphi/g$. Then the spectral problem for fermionic wavefunctions $\psi_\omega$ with definite energy $\omega$ takes the form

$$\omega\psi_\omega = -i\alpha\psi'_\omega + \beta\,\mathrm{e}^{i\gamma_5\varphi}\left[M\theta_{\mathrm{II}} + M_0\theta_{\mathrm{III}}\right]\psi_\omega. \tag{1.5}$$

Upon taking $M_0 \to \infty$, we get that $\psi_\omega \to 0$ in domain III in such a way that the term $M_0\psi_\omega$ in Eq. (1.5) vanishes, and the chiral boundary conditions [3, 5–7, 22] at the points $\pm x_2$ appear instead:

$$\pm i\gamma^1\psi_\omega(\pm x_2) + \mathrm{e}^{i\gamma_5\varphi(\pm x_2)}\psi_\omega(\pm x_2) = 0. \tag{1.6}$$

In domain I, Eq. (1.5) is the equation for free massless fermions:

$$\omega\psi_{\mathrm{I}} = -i\alpha\psi'_{\mathrm{I}}, \tag{1.7}$$

while in the intermediate domain II one has

$$\omega\psi_{\mathrm{II}} = -i\alpha\psi'_{\mathrm{II}} + \beta M\,\mathrm{e}^{i\gamma_5\varphi}\psi_{\mathrm{II}}. \tag{1.8}$$

The wavefunction's continuity on the boundary between domains I and II gives

$$\psi_{\mathrm{I}}(\pm x_1) = \psi_{\mathrm{II}}(\pm x_1), \tag{1.9}$$

while $\psi_{\mathrm{II}}(\pm x_2)$ are subject of the boundary conditions (1.6). At the same time, the field $\varphi$ in Eq. (1.8) has to be determined self-consistently from Eq. (1.3b) with corresponding continuity conditions at points $|x| = x_{1,2}$.

## 2. SOLUTIONS WITH NONZERO TOPOLOGICAL CHARGE

The essential feature of this model is that the coupled equations (1.3) in the closed intermediate domain II of finite size $d = x_2 - x_1$ possess simple and physically meaningful solution, which would be unacceptable if these equations were considered in the infinite space. In order to obtain this solution in the most consistent way, we perform first in domain II the chiral Skyrme rotation

$$\psi_\omega = \exp(-i\gamma_5\varphi/2)\chi_\omega, \tag{2.1}$$

by virtue of which Eq. (1.8) and the boundary conditions (1.6) transform correspondingly into

$$\left(\omega - \frac{1}{2}\varphi'\right)\chi_\omega = -i\alpha\chi'_\omega + \beta M\chi_\omega, \tag{2.2}$$

$$\pm i\gamma^1\chi_\omega(\pm x_2) + \chi_\omega(\pm x_2) = 0. \tag{2.3}$$

It follows from Eq. (2.2) that, if we assume the linear behavior for the field $\varphi(x)$ in domain II, namely,

$$\varphi' = \mathrm{const} = 2\lambda, \tag{2.4}$$

then it becomes the equation for free massive fermions:

$$\nu\chi = -i\alpha\chi' + \beta M\chi, \tag{2.5}$$

with eigenvalues $\nu = \omega - \lambda$. So the fermions being massless in domain I acquire the mass $M$ in domain II due to the coupling to the field $\varphi$, whence the intermediate phase emerges describing massive quasifree «constituent quarks».

The most important feature of Eq. (2.5) is that it reveals the sign symmetry $\nu \to -\nu$, which corresponds to the unitary transformation of the fermionic wavefunction

$$\chi \to \tilde{\chi} = i\gamma_1\chi, \tag{2.6}$$

while the chiral currents

$$j_5 = i\bar{\psi}\gamma_5 \, \mathrm{e}^{i\gamma_5\phi}\psi = i\chi^+\gamma_1\chi \tag{2.7}$$

coincide for these sign-symmetric states:

$$j_5 = i\chi^+\gamma_1\chi = i\tilde{\chi}^+\gamma_1\tilde{\chi} = \tilde{j}_5. \tag{2.8}$$

However, the sign symmetry of Eq. (2.5) itself cannot ensure the corresponding one for the fermion spectrum, since it takes place in domain II only, while the latter has to be determined from the Dirac equation on the unification I $\cup$ II. Meanwhile in domain I one has Eq. (1.8), which possesses another symmetry, namely, $\omega \leftrightarrow -\omega$. That means that the sign symmetry $\nu \leftrightarrow -\nu$ of the fermionic spectrum could hold only for some discrete values of the derivative $\varphi'$ in domain II. These values are determined from the algebraic equation for fermionic energy levels, which is obtained from the straightforward solution of Eqs. (1.6)–(1.9) and reads

$$\exp(4i\omega x_1) = \frac{1 - \mathrm{e}^{-2ikd}\dfrac{M - i(\nu + k)}{M - i(\nu - k)}}{1 - \mathrm{e}^{-2ikd}\dfrac{M + i(\nu - k)}{M + i(\nu + k)}} \; \frac{1 - \mathrm{e}^{2ikd}\dfrac{M - i(\nu - k)}{M - i(\nu + k)}}{1 - \mathrm{e}^{2ikd}\dfrac{M + i(\nu + k)}{M + i(\nu - k)}}, \tag{2.9}$$

where $\nu^2 = k^2 + M^2$. It is easy to find from (2.9) that the fermionic spectrum reveals the symmetry $\nu \leftrightarrow -\nu$, if

$$4\lambda x_1 = \pi s, \tag{2.10}$$

where $s$ is integer, since for such values of $\varphi'(x)$ in domain II the left-hand side (l. h. s.) of Eq. (2.9) reduces to $(-1)^s \exp(4i\nu x_1)$.

When the condition (2.10) is fulfilled, the following consequence of arguments becomes reasonable. In the right-hand side (r. h. s.) of Eq. (1.3b), which determines $\varphi''(x)$ in domain II, we have the vacuum expectation value (v. e. v.) of the $C$-odd chiral current

$$J_5 = \frac{1}{2}\left[\bar{\psi}, i\gamma_5 \, \mathrm{e}^{i\gamma_5\phi}\psi\right]_- = \frac{1}{2}\left[\chi^+, i\gamma_1\chi\right]_-, \tag{2.11}$$

with $\chi$ being now the secondary quantized fermion field in the chiral representation (2.1)

$$\chi(x,t) = \sum_n b_n\chi_n(x)\,\mathrm{e}^{-i\omega_n t}, \tag{2.12}$$

where $\chi_n(x)$ are the normalized solutions of the corresponding Dirac equation, while $b_n, b_n^+$ are the fermionic creation-annihilation operators, which obey the canonical anticommutation relations

$$\{b_n, b_{n'}^+\}_+ = \delta_{nn'}, \quad \{b_n, b_{n'}\}_+ = 0. \tag{2.13}$$

The average over the given bag's state includes, by definition, the average over the filled sea of negative energy states $\omega_n < 0$ plus possible occupied valence fermion states with $\omega_n > 0$, which are dropped for a moment because their status is discussed specially below. Finally,

$$\langle J_5 \rangle = \langle J_5 \rangle_{\text{sea}} = \frac{1}{2} \left( \sum_{\omega_n < 0} - \sum_{\omega_n > 0} \right) \chi_n^+ i\gamma_1 \chi_n. \tag{2.14}$$

It should be emphasized that in Eq. (2.14) the division of fermions into sea and valence ones is made in correspondence with the sign of their eigenfrequencies $\omega_n$, which differ from sign-symmetric $\nu_n$ by the shift in $\lambda$:

$$\omega_n = \nu_n + \lambda, \tag{2.15}$$

and so do not possess the sign symmetry $\omega \leftrightarrow -\omega$. However, if we suppose additionally that $\nu_n$ and $\lambda$ are such that for all $n$ the signs of $\nu_n$ and $\omega_n$ coincide, i.e., after shifting by $\lambda$ none of $\nu_n$'s changes its sign, then the condition $\omega_n \gtrless 0$ in Eq. (2.14) will be equivalent to the condition $\nu_n \gtrless 0$. Thence

$$\langle J_5 \rangle_{\text{sea}} = \frac{1}{2} \left( \sum_{\nu_n < 0} - \sum_{\nu_n > 0} \right) \chi_n^+ i\gamma_1 \chi_n = 0 \tag{2.16}$$

by virtue of the relation (2.8). In turn, it means that Eq. (1.3b) in domain II reduces to $\varphi'' = 0$, which is in complete agreement with our initial assumption that $\varphi'(x) = \text{const}$ in domain II. In other words, we obtain the solution of the coupled Eqs. (1.3) in domain II in the form

$$\varphi(x) = \begin{cases} 2\lambda(x - x_1), & x_1 \le x \le x_2, \\ 2\lambda(x + x_1), & -x_2 \le x \le -x_1, \end{cases} \tag{2.17}$$

where $\lambda$ takes discrete values from (2.10), while the fermionic spectrum is determined from the relation (2.15) with $\nu_n$ being defined from Eq. (2.9) after replacing the l.h.s. to $(-1)^s \exp(4i\nu x_1)$.

There are the following keypoints that make this solution meaningful. The first is the finiteness of the intermediate domain size $d$, because for an infinite domain II the solution (2.17) would be unacceptable. In our case, however, the size of the intermediate domain is always finite by construction, while the boson field $\varphi(x)$ acquires the solitonic behavior in domain III due to self-interaction $V(\varphi)$. Here the following circumstance manifests itself again: in (1 + 1)D the chiral coupling $\bar{\psi} e^{i\gamma_5 \varphi} \psi$ itself cannot cause the solitonic behavior of the scalar field by virtue of the effects of fermion-vacuum polarization only, i.e., without some additional self-interaction of bosons [23]. The second point is the discreteness and the $\nu \leftrightarrow -\nu$ symmetry of the fermionic spectrum, which leads in turn to a reasonable method of calculation for the average of the chiral current $J_5$ over the filled Dirac sea (2.16), as well as for other $C$-odd observables like the total fermion number. After all, in the case we consider the boson field is continuous everywhere and so is topologically equivalent to the odd soliton that would take place in absence of fermions due to the self-interaction $V(\varphi)$ only. So the topological number of the boson field does not depend on the existence and sizes of the spatial domains containing fermions (I $\cup$ II). On the other hand, the baryon number of the hybrid bag is, by definition, the sum of the topological charge of the boson soliton and

the fermion number of the bag interior. In our case the latter is zero (for the ground state), hence the baryon number of the bag is determined by the topological charge of the boson field only and does not depend on the sizes of domains I and II containing fermions, which meets the general requirements for hybrid models. Some more details concerning the status of this solution of Eqs. (1.3) can be found in Ref. [10].

It should also be mentioned that, although the (topological) quantum numbers of such a bag are determined by its solitonic component, it does not mean that the filled fermion levels with positive energy could not exist at all. This would take place for small enough values of the parameter $\lambda$ only. If $\lambda$ increases, the negative levels $\omega_n = -|\nu_n| + \lambda$ should move into the positive part of the spectrum. The change of sign of each such level will decrease $\langle Q \rangle_{\text{sea}}$ by one unit of charge, but if we fill the emerging positive level with the valence fermion, then the sum $Q_{\text{val}} + Q_{\text{sea}}$ remains unchanged. Analogously, the total axial current will be equal to $J_{\text{val}} + J_{\text{sea}}$ and will not change either, which ensures the vanishing r. h. s. of Eq. (1.3b) and so preserves the status of linear function (2.17) as the self-consistent solution of the field equations. Therefore, the existence or absence of valence fermions in such construction of the ground state of the bag depends actually on the relation between $\lambda$ and $|\nu|_{\text{min}}$ and so appears to be a dynamical quantity like the other bag's parameters (the size and mass), which are determined from the total energy minimization procedure.

Another essential feature of this bag configuration is that (2.17) ensures the self-consistent solution of Eqs. (1.3) for even values $s = 2r$ in (2.10) only. The reason is that for odd values $s = 2r + 1$ the fermionic spectrum obtained from the solution of Eqs. (1.6)–(1.9) under the condition $\varphi' = 2\lambda$ will always contain the nondegenerate energy level $\chi_0(x)$ with zero frequency $\nu_0 = 0$, whereas for even values $s = 2r$ one has $\nu_n \neq 0$, $\forall n$. According to the general theory [24], such a zero mode causes fractionalization, which means that its contribution to all $C$-odd observables will be given by the operator $(1/2)(b_0^+ b_0 - b_0 b_0^+)$ with the eigenvalues $\pm 1/2$ and the numeric coefficient determined by $\chi_0(x)$. On the other hand, in Eq. (1.3b) the chiral current should be averaged over its eigenvector in order to keep up the vanishing dispersion of the r. h. s., otherwise the system of equations (1.3) would be ill-defined. So the operator part of the zero mode contribution to the r. h. s. of (1.3b) reduces to the factor $\pm 1/2$, while $\chi_0(x)$ appears to be such that the corresponding chiral current in domain II does not vanish (it is proportional to $\exp(-2M|x|)$). Hence for odd values $s = 2r + 1$ the r. h. s. of Eq. (1.3b) does not vanish, and the function (2.17) is no longer the self-consistent solution of Eqs. (1.3). However, it is easy to find the way of constructing analogous bags, where the odd values $s = 2r + 1$ are allowed instead of the even ones, utilizing the specific, for such $(1 + 1)$D bag models, possibility to choose in the model Lagrangian the signs of the chiral fermionic masses $M, M_0$, independently to the right and to the left of the central domain of asymptotic freedom. This question is worked out more explicitly in Ref. [25].

## 3. THE TOTAL ENERGY OF THE BAG FOR THE NONZERO TOPOLOGICAL CHARGE

As a result, for the bag with the topological charge 1 the boson field is zero in domain I, in domain II it is the linear function (2.17) with $\lambda = \pi r / 2x_1$, which after restoring the $g$-dependence is sewn together with the odd soliton solution of Eq. (1.4b) in the bag's exterior. The typical behavior of $\varphi(x)$ is presented in Fig. 1. For simplicity we shall suppose that in

domain III the asymptotic expansion of the soliton solution of Eq. (1.4b) for large $|x|$ can be used, namely,

$$\varphi_{\rm sol}(x) = \frac{\pi}{g}\left(1 - A\,{\rm e}^{-mx}\right), \quad x > x_2, \quad (3.1)$$

with $m$ being the meson mass in the bag's exterior (for $x < -x_2$, $\varphi_{\rm sol}(x)$ is determined via oddness).

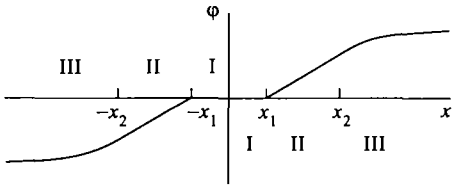


Fig. 1. The configuration of the boson field for a single bag with the topological charge 1

The factor $\pi/g$ means that we deal actually with the phase soliton with the total amplitude being multiple of $2\pi/g$, since it is the period of the initial chiral interaction $\bar{\psi}\exp(i\gamma_5 g\varphi)\psi$. The constant $A$ is determined from the continuity conditions for boson field at points $x = \pm x_2$, which gives

$$x_1 = \frac{r}{r+1}(x_2 + 1/m), \quad d = \frac{x_2 - r/m}{r+1}. \quad (3.2)$$

The condition $d \geq 0$ gives rise then to an additional restriction for the size of the confinement domain

$$mx_2 \geq r, \quad (3.3)$$

which shows that $r$ could be naturally interpreted as the index enumerating the excited states of the bag, whose sizes increase with $r$.

For the total energy of the boson field, one finds

$$E_\varphi = m\frac{\pi^2}{g^2}\frac{r+1}{mx_2+1}. \quad (3.4)$$

The total energy of the bag is the sum of $E_\varphi$ and the fermionic contribution $E_\psi$:

$$E_{\rm bag} = E_\varphi + E_\psi. \quad (3.5)$$

As it follows from (3.4), the boson field energy decreases smoothly for increasing $x_2$, so all the nontrivial dependence of the total bag energy $E_{\rm bag}$ on the model parameters originates from the fermionic contribution $E_\psi$, which is the sum of the filled Dirac sea of negative energy states and positive energy valence fermions:

$$E_\psi = E_{\rm val} + E_{\rm sea}. \quad (3.6)$$

Bearing in mind that the charge conjugation symmetry dictates the following definition of the Dirac sea energy [23, 26]:

$$E_{\rm sea} = \frac{1}{2}\sum_{\omega_n<0}\omega_n - \frac{1}{2}\sum_{\omega_n>0}\omega_n, \quad (3.7)$$

for the ground state of the bag described above, the sum (3.6) can be reduced to a single universal expression. If the transformation from $\omega_n$ to $\nu_n$ is sign-preserving for all $n$ and so there are no valence fermions in the ground state of the bag, one finds from (3.7)

$$E_\psi = E_{\rm sea} = \frac{1}{2}\sum_{\nu_n>0}(-\nu_n + \lambda) - \frac{1}{2}\sum_{\nu_n>0}(\nu_n + \lambda) = -\sum_{\nu_n>0}\nu_n. \quad (3.8)$$

If the parameter $\lambda$ appears to be large enough, the initially negative level $\omega_n = -|\nu_n| + \lambda$ changes its sign and turns into the occupied valence state. In this case it is convenient to calculate $E_\psi$ in two steps. At first, we consider the contribution from all states with $|\nu_n| > \lambda$ to $E_{\text{sea}}$, which in analogy to (3.8) reads

$$E'_{\text{sea}} = -\sum_{\nu_m > \lambda} \nu_m. \tag{3.9}$$

To this expression the energy of emerging valence fermion $E_{\text{val}} = -|\nu_n| + \lambda$ and the contribution of the positive levels with $\omega_n = \pm|\nu_n| + \lambda$ to the Dirac sea energy should be added, which gives

$$E_\psi = -|\nu_n| + \lambda - \frac{1}{2}[(-|\nu_n| + \lambda) + (|\nu_n| + \lambda)] + E'_{\text{sea}} = -\sum_{\nu_n > 0} \nu_n, \tag{3.10}$$

i.e., the same expression (3.8) as we have got for the energy of fermions without filled valence states.

For what follows it is convenient to introduce a set of new parameters, in terms of which the total energy of the bag takes the most appropriate form. First, we introduce the dimensionless quantities

$$\alpha = 2Mx_1, \quad \beta = 2Md, \quad \rho = 2Mx_2, \tag{3.11}$$

and consider in more detail Eq. (2.9), which determines the energy levels $\nu_n$. This equation has two branches of roots. The first one corresponds to real $k$ and in terms of $\alpha$ and $\beta$ can be transformed into the following form:

$$\tan\left(\alpha\sqrt{1+x^2}\right) = \frac{x}{\sqrt{x^2+1}} \frac{x\cos\beta x + \sin\beta x}{1 - \cos\beta x + x\sin\beta x}, \tag{3.12}$$

where the unknown quantity is the dimensionless $x$ defined through $k = Mx$, so that $\nu = M\sqrt{1+x^2}$. The real roots $x_n$ of (3.12) belong to the semiaxis $0 \le x_n < \infty$, since the fermionic wavefunctions are actually the standing waves in a finite spatial box with degeneracy in the sign of $k$, while the corresponding frequencies $\nu_n$ lie in the interval $M \le \nu_n < \infty$. The second branch corresponds to imaginary $k = iMx$, $\nu = M\sqrt{1-x^2}$, $0 \le x \le 1$ and can be derived from (3.12) through the analytical continuation:

$$\tan\left(\alpha\sqrt{1-x^2}\right) = \frac{x}{\sqrt{1-x^2}} \frac{x\cosh\beta x + \sinh\beta x}{\cosh\beta x + x\sinh\beta x - 1}. \tag{3.13}$$

For this branch one has $0 < \nu_n \le M$.

Thus, $\nu_n$ and so $E_\psi$ appear to be functions of two dimensionless parameters $\alpha$ and $\beta$, whose sum is the dimensionless total size of the confinement domain $\rho$:

$$\alpha + \beta = \rho. \tag{3.14}$$

Proceeding further, it is convenient to extract the mass of the «constituent quark» $M$ from the sea energy and fermionic frequencies as a dimensional factor:

$$\varepsilon_n = \nu_n/M = \sqrt{1+x_n^2}, \tag{3.15}$$

hence $E_\psi = -M\sum_n \varepsilon_n$. Upon introducing the dimensionless ratio of the two mass parameters of the model

$$\mu = m/2M, \tag{3.16}$$

the dimensionless energy of fermions $\mathcal{E}_\psi = E_\psi/M$ and analogously the dimensionless total energy $\mathcal{E}_{\rm bag} = E_{\rm bag}/M$, for the latter one finds

$$\mathcal{E}_{\rm bag} = \mathcal{E}_\psi(\alpha,\beta) + 2\mu\frac{\pi^2}{g^2}\frac{r+1}{\mu\rho+1}, \tag{3.17}$$

where the dimensionless parameters $\alpha$, $\beta$ are determined through $\mu$ and $\rho$ as

$$\alpha = \frac{r}{r+1}\,(\rho+1/\mu), \quad \beta = \frac{\rho - r/\mu}{r+1}. \tag{3.18}$$

So the total energy of the bag depends ultimately on two dimensionless parameters, $\mu$ and $\rho$, where the parameter $\mu$ is fixed by the ratio of the masses $m$ and $M$, while the optimal value of the bag's size should be found from the minimum of the total energy $\mathcal{E}_{\rm bag}(\rho)$ for given $\mu$.

To study the behavior of $\mathcal{E}_{\rm bag}(\rho)$, first of all we have to renormalize the fermion sea energy $\mathcal{E}_\psi$, which is obviously UV-divergent. Let us start with the asymptotics of roots of Eq. (3.12) for $x_n \gg 1$. Representing Eq. (3.12) as

$$\sin\left(\alpha\sqrt{1+x^2}\right) = \frac{1}{2}\left(\sqrt{1+x^2}+x\right)\sin\left(\alpha\sqrt{1+x^2}+\beta x+\delta\right) +$$

$$+\frac{1}{2}\left(\sqrt{1+x^2}-x\right)\sin\left(\alpha\sqrt{1+x^2}-\beta x-\delta\right), \tag{3.19}$$

where $\delta = \arctan x$, one finds

$$\varepsilon_n(\alpha,\beta) = \frac{\pi/2+\pi n}{\rho} + \frac{(-1)^{n-1}\sin\left[(\pi/2+\pi n)\alpha/\rho\right]+1+\beta/2}{\pi/2+\pi n} + O(1/n^2). \tag{3.20}$$

In the expression (3.20) the first term yields the quadratic and linear divergences in $\sum_n \varepsilon_n$, the second one produces the logarithmic one, while the term with the sine does not cause any divergence at all. To compensate the contribution of the first term, the energy of the sea of free fermions contained in the same «volume» $\rho$ should be subtracted, while the logarithmic divergence, proportional to $\beta/2$, is cancelled by the relevant one-loop counterterm of the boson self-energy [10]. The remaining logarithmic divergence, associated with the term $1/(\pi/2+\pi n)$, does not depend on the bag parameters and originates from the fermion confinement inside the bag, rather than from some local interaction. Actually, it is the divergent part of the energy of interaction between fermions and the confining potential (bag boundaries). The appearance of such diverging boundary energy in $\mathcal{E}_\psi$ is a specific feature of fermion vacuum polarization in all the bag models [6,7,27–32].

In the considered three-phase model this effect acquires some additional features. First, it takes place for nonzero size $d \neq 0$ of the intermediate phase only, while the corresponding boundary energy is negative and diverges as $(-\sum_n 1/(\pi/2+\pi n))$. More particularly, if $\alpha \to \rho$, then $(-1)^{n+1}\sin\left[(\pi/2+\pi n)\alpha/\rho\right] \to -1$, hence there remains only the logarithmic term $\beta/(\pi+2\pi n)$ in the asymptotics (3.20). Therefore in this limit $\mathcal{E}_\psi$ becomes finite just after

subtraction of the energy of perturbative vacuum and addition of the one-loop counterterm. On the other hand, the limit $\alpha \to \rho$ is equivalent to $\beta/\alpha \to 0$, and so the infinite energy of the interaction between fermions and bag boundaries takes place only for $d \neq 0$ and the finite size of the central domain (the phase of asymptotic freedom) of the bag.

So the considered three-phase bag model does not actually reveal the ability for the smooth transition into a two-phase configuration for $d \to 0$, although such an opportunity exists formally on the level of the initial Lagrangian (1.1). In fact, in the case of the two-phase bag ($d \equiv 0$) the exact fermion levels are $\varepsilon_n = (\pi/2 + \pi n)/\rho$, hence the single subtraction of the perturbative vacuum energy suffices for renormalization of $\mathcal{E}_\psi$. Therefore the transition between two- and three-phase bag configurations requires an infinite amount of energy, which is a specific feature of such many-phase systems. Note also that in the case of the two-phase bag ($d \equiv 0$) massless fermions are reflected directly from the bag boundaries. So in the three-phase model the infinite boundary energy of the bag is intimately bound up with the circumstance that for $d \neq 0$ the boundaries of the bag reflect massive fermions.

Within the three-phase models we have an opportunity to demonstrate this effect in an even more apparent way. For these purposes let us consider the $(1+1)$-dimensional analog of a «dibaryon», i. e., the configuration with the topological charge 2. Such an object consists of two identical topological bags of the type described above, which are placed so close to each other that their neighboring intermediate domains overlap. The corresponding Lagrangian takes the form

$$\mathcal{L} = \bar{\psi} i \hat{\partial} \psi + \frac{1}{2}(\partial_\mu \varphi)^2 - \frac{M}{2}\left[\bar{\psi}, \mathrm{e}^{ig\gamma_5\varphi}\psi\right]_- \theta_{\mathrm{I}} -$$

$$-\frac{1}{2} m_0^2 \left((\varphi - \pi/g)^2 \theta_{\mathrm{II}}^{(+)} + (\varphi + \pi/g)^2 \theta_{\mathrm{II}}^{(-)}\right) - \left(\frac{M_0}{2}\left[\bar{\psi}, \mathrm{e}^{ig\gamma_5\varphi}\psi\right]_- + V(\varphi)\right)\theta_{\mathrm{III}}, \quad (3.21)$$

where $\theta_{\mathrm{I}} = \theta((|x| \leq x_0) \cup (x_1 \leq |x| \leq x_2))$, $\theta_{\mathrm{II}}^{(\pm)} = \theta(x_0 < \pm x < x_1)$, $\theta_{\mathrm{III}} = \theta(|x| > x_2)$, with the same rule concerning field variations as for (1.1).

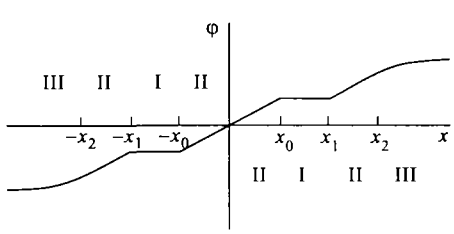


Fig. 2. The boson field profile for the «dibaryon»

The self-consistent solution of the model (3.21) corresponding to such a «dibaryon» configuration is again constructed assuming the linear behavior (2.4) for the boson field in the intermediate domains and taking account of the sign symmetry $\nu \leftrightarrow -\nu$ as well as of the conservation of the chiral current $j_5 = \tilde{j}_5$ for the transformations $\chi \to \tilde{\chi} = \sigma_2 \chi$. Omitting some straightforward, but lengthy calculations, let us present the main results.

The profile of the boson field, corresponding to the dibaryon configuration, is shown on Fig. 2. For the intermediate domains of this configuration, one obtains $\varphi' = \mathrm{const} = 2\lambda$, where $\lambda$ satisfies the condition

$$2\lambda a = \pi s, \quad a = x_1 - x_0. \quad (3.22)$$

The latter is quite analogous to Eq. (2.10) for a single isolated bag, since the parameter $2x_1$ in (2.10), as well as $a$ in (3.22), is the size of the domain of asymptotic freedom for a single bag. However, in the case of the dibaryon there are no zero modes in the fermionic spectrum for any values of $s$, hence no additional restrictions imposed on the integer $s$ in Eq. (3.22).

It is obvious that the $(1+1)$-dimensional model (3.21) cannot be considered as a realistic model of the dibaryon to any extent. However, being simple and nontrivial simultaneously, it turns out to be a very fruitful illustration for the study of the origin of additional logarithmically divergent terms $1/(\pi/2+\pi n)$ in the UV asymptotics of the fermionic spectrum in such three-phase bag models. The latter is again obtained from the corresponding transcendent equation for fermion levels, which in the trigonometric form reads

$$\sin\left(2\alpha\sqrt{1+x^2}\right)\left(x\sqrt{1+x^2}\cos\left((\beta+\gamma)x+\delta\right)-x\cos\gamma x\right)+$$

$$+\cos\left(2\alpha\sqrt{1+x^2}\right)\left(x^2\sin\left((\beta+\gamma)x+\delta\right)-\sqrt{1+x^2}\sin\gamma x+\sin\gamma x\sin\left(\beta x+\gamma\right)\right)+$$

$$+\left(\sqrt{1+x^2}-\cos\left(\beta x+\gamma\right)\right)\sin\gamma x=0, \tag{3.23}$$

where $\alpha = Ma$, $\beta = 2Md$, $d = x_2 - x_1$, $\gamma = 2Mx_0$, $\delta = \arctan x$. The parameter $d = x_2 - x_1$ is the size of the outward intermediate domains for each of the single bags forming the dibaryon, while $2x_0$ is the size of their common internal intermediate domain, i.e., the domain of their mutual interaction. The UV asymptotics of $\varepsilon_n$'s in this case has the following form:

$$\varepsilon_n(\alpha,\beta,\gamma)=\frac{\pi/2+\pi n}{\rho}+$$

$$+\frac{(-1)^{n+1}\left(\sin\left[(\pi/2+\pi n)(2\alpha+\gamma)/\rho\right]-\sin\left[(\pi/2+\pi n)\gamma/\rho\right]\right)+1+(\beta+\gamma)/2}{\pi/2+\pi n}+O(1/n^2), \tag{3.24}$$

where

$$\rho = 2\alpha+\beta+\gamma = M(2a+2d+2x_0) = 2Mx_2 \tag{3.25}$$

is the total dimensionless bag's size. As in the case of a single isolated bag, the main divergent term in the asymptotics (3.24) corresponds to the sea energy of free fermions in the «volume» $\rho$, while the logarithmic term, proportional to $(\beta+\gamma)/2$, is exactly compensated by one-loop self-energy counterterm. The change of the coefficient in this term compared to (3.20) is caused by the fact that in the considered case the interaction between fermions and boson field takes place in the domain of the size $2d+2x_0$. Besides this, there remains again a logarithmically divergent term $1/(\pi/2+\pi n)$, which corresponds to the (infinite) energy of the interaction between fermions and the confining potential (bag boundaries). It follows from Eq. (3.24) that on the level of divergent terms the boundary energy of the dibaryon coincides exactly with that of a single isolated bag. So we are led to an unambiguous conclusion that it is indeed the effect of fermion confinement in a simply connected domain, which gives rise to the term $1/(\pi/2+\pi n)$ in Eqs. (3.20) and (3.24), since in the dibaryon configuration the number of boundary points is just the same as in the case of one isolated bag. Note also that the direct consequence of this circumstance is that in $(1+1)$D the dibaryon configuration cannot be obtained as a result of continuous fusion of two isolated bags, since when they are separated enough from each other, the sum of their boundary energies is twice larger than that of the dibaryon. In other words, in $(1+1)$D the reconstruction of the bag's boundary in the fusion-fission processes requires an infinite amount of energy.

After all, it follows from (3.24) that for $\beta \to 0$, i.e., for vanishing outward intermediate domains of the dibaryon, one gets $(-1)^{n+1} \sin[(\pi/2 + \pi n)(2\alpha + \gamma)/\rho] \to -1$, which compensates the term $1/(\pi/2 + \pi n)$, and the infinite interaction energy between fermions and bag boundaries disappears. This circumstance provides with one more argument the assertion, made for a single bag by analysis of the asymptotics (3.20), that the infinite boundary energy appears only when fermions pass through the intermediate phase just before reflection from the bag boundaries.

As a result, for a three-phase bag with $d \neq 0$ the extraction of the finite part from $\mathcal{E}_\psi$ consists actually of two separate procedures. The first one is the standard renormalization onto perturbative vacuum with account of the one-loop counterterm, caused by virtual fermion pairs [10]. The second one is the compensation of the boundary energy by means of an appropriate subtraction, and both procedures suffer from an ambiguity in the choice of subtraction point. In the «classical» renormalization scheme, this uncertainty is resolved by fixing the physical values for a corresponding number of parameters. For obvious reasons, we avoid doing that in our «toy» $(1+1)$D model, but consider instead the most straightforward approach to the compensation of divergences in the sum (3.8), which keeps up the continuous dependence of the result of substraction on the model parameters. The essence of this approach is that we subtract from $\sum_n \varepsilon_n$ another sum with the same summation index $n$, whose common term coincides exactly with the divergent part of asymptotics (3.20). The result is the finite quantity

$$\tilde{\mathcal{E}}_\psi = -\sum_n \left[\varepsilon_n - \left(\frac{\pi/2 + \pi n}{\rho} + \frac{1 + \beta/2}{\pi/2 + \pi n}\right)\right]. \tag{3.26}$$

This method requires no additional counterterms, because all the divergences are already cancelled by the subtracted sum. Of course, to some extent the physical meaning of such a procedure is lost. It should be emphasized, however, that it is only the $(1+1)$D case when the theory with coupling $\mathcal{L}_{\mathrm{I}} = G\bar{\psi}(\sigma + i\gamma_5\pi)\psi$ is (super)renormalizable and any counterterm has explicit physical meaning. For higher space dimensions this is already not true and so the procedure of compensation of divergences in the energy based on (3.26) should not be considered as having no motivation. For more detailed discussion on the extraction of the finite part from the divergent Dirac sea energy in $(3+1)$D HCBM see Refs. [30–32].

Now — having dealt with the renormalization of $\mathcal{E}_\psi$ in this way — let us turn to the study of the total bag energy

$$\mathcal{E}_{\mathrm{bag}} = \tilde{\mathcal{E}}_\psi(\alpha, \beta) + 2\mu \frac{\pi^2}{g^2} \frac{r+1}{\mu\rho + 1} \tag{3.27}$$

as a function of the parameters $\mu$ and $\rho$. The convergent logarithmic sine-term in the asymptotic expression (3.20) gives rise to the first feature of $\mathcal{E}_{\mathrm{bag}}$. For these purposes we transform this term to the form

$$\left(\tilde{\mathcal{E}}_\psi\right)_{\log}(\alpha, \beta) = \frac{1}{\pi} \sum_{n \gg 1} (-1)^n \frac{\sin[(\pi\alpha/\rho)(n + 1/2)]}{n + 1/2} \tag{3.28}$$

and then use the well-known relation

$$\sum_{n=0}^{\infty} (-1)^n \frac{\sin[z(n + 1/2)]}{n + 1/2} = \ln \tan(\pi/4 + z/4), \quad |z| < \pi. \tag{3.29}$$

The sums (3.28) and (3.29) possess the similar common term, while the sum (3.28) diverges as $(-\ln(\pi - z))$ when $z \to \pi$. So for $\pi\alpha/\rho \to \pi$ , which implies $\beta \to 0$, the sum (3.29) will show the similar behavior, namely,

$$\left(\tilde{\mathcal{E}}_{\psi}\right)_{\log}(\alpha, \beta) \to -(1/\pi)\ln\beta, \quad \beta \to 0. \tag{3.30}$$

Therefore, both the renormalized fermion energy (3.26) and the total bag's energy (3.27) reveal the logarithmic singularity for $\beta \to 0$, i.e., for $\rho \to r/\mu$, which confirms the qualitative analysis of the vacuum polarization effects in the three-phase bag, performed above. More precisely, after the subtraction (3.26) the renormalized $\tilde{\mathcal{E}}_{\psi}$ includes $\sum_n 1/(\pi/2 + \pi n)$ as a counterterm for the divergent part of the boundary energy, but the latter disappears for $\beta \to 0$.

$\mathcal{E}_{\text{bag}}$ will also grow for $\rho \to \infty$. In this case $\alpha/\rho \to r/(r+1)$, so the logarithmic term (3.28) remains finite, which means that we have to deal now with the whole sum (3.26). However, the leading order behavior of $\tilde{\mathcal{E}}_{\psi}$ can be evaluated from (3.26) quite effectively by virtue of the fact that for $\rho \to \infty$ the fermionic spectrum becomes quasicontinuous, which allows one to transform the sum over $x_n$ into integral over $dx$. The analysis of distribution of the roots of Eq. (3.12) shows that in this limit $\sum_n \varepsilon_n$ can be estimated by the following (divergent) integral:

$$\sum_n \varepsilon_n \to \frac{1}{\pi}\int dx\,\sqrt{1+x^2}\left[\beta + \frac{1}{1+x^2} + \alpha\frac{x^2}{x^2+\sin^2\left(\alpha\sqrt{1+x^2}\right)} - \right.$$
$$\left. - \frac{\sin\left(\alpha\sqrt{1+x^2}\right)\cos\left(\alpha\sqrt{1+x^2}\right)}{\sqrt{1+x^2}\left(x^2+\sin^2\left(\alpha\sqrt{1+x^2}\right)\right)}\right]. \tag{3.31}$$

For the subtracted sum in (3.26) one finds

$$\sum_n \left(\frac{\pi/2+\pi n}{\rho} + \frac{1+\beta/2}{\pi/2+\pi n}\right) \to \frac{\rho}{\pi}\int dx\,\left(x + \frac{1+\beta/2}{\rho x}\right). \tag{3.32}$$

The integrals (3.31) and (3.32) have obviously the same divergent part $(1/\pi)\int dx(\rho x + 1/x + \beta/2x)$, and so their difference yields a converging integral, in agreement with the subtraction procedure. The leading term of the integrand in this difference, taken with the (correct) inverse sign, is $\beta/8\pi x^3$. Since $\beta \to \rho/(r+1)$ for $\rho \to \infty$, this finally leads to the emergence of the positive, proportional to $\rho$, contribution to $\tilde{\mathcal{E}}_{\psi}$ and correspondingly to $\mathcal{E}_{\text{bag}}$.

The numerical calculations confirm completely such qualitative predictions for the behavior of $\mathcal{E}_{\psi}(\rho)$ and $\mathcal{E}_{\text{bag}}(\rho)$. The values of free parameters $\mu$ and $g$ are chosen as $\mu = 0.25$, which corresponds approximately to the ratio $m_{\pi}/2M_Q$, and $g = 1$, because the energy of the boson soliton does not have any significant influence on the main properties of $\mathcal{E}_{\text{bag}}(\rho)$. The results of $\mathcal{E}_{\text{bag}}(\rho)$ calculation for $r = 1, 2, 3, 4, 5$ are depicted on Fig. 3 and show that the size and energy of the solution, determined from the minimum of $\mathcal{E}_{\text{bag}}(\rho)$, grow continuously for increasing $r$, whereas the curvature of $\mathcal{E}_{\text{bag}}(\rho)$ in the minimum decreases, which supports the interpretation of configurations with $r > 1$ as excited states of the bag.

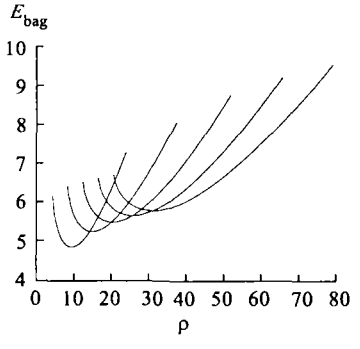


Fig. 3. The dependence of the topological bag's energy on its size

## 4. BAGS WITH ZERO TOPOLOGICAL CHARGE

For bags with vanishing topological charge the relevant configuration of the boson field should be an even one $\varphi(x) = \varphi(-x)$. The principal difference between this case and the previous one is that for even $\varphi(x)$ the sign symmetry $\omega \leftrightarrow -\omega$ is a characteristic feature of the spectral problem for fermions (1.6)–(1.9), which can be easily justified by means of the following transformation of fermionic wavefunctions:

$$\psi_\omega(x) \to \psi_{-\omega}(x) = \pm\gamma_5\psi_\omega(-x). \tag{4.1}$$

However, the corresponding chiral currents are related now in the following way:

$$j^5_{-\omega}(x) = -j^5_\omega(-x), \tag{4.2}$$

so there is no automatic compensation between positive- and negative-frequency terms in the v.e.v. of $J_5(x)$. From (4.2) one can derive only the relation

$$\langle J_5(x)\rangle_{\text{sea}} = \langle J_5(-x)\rangle_{\text{sea}}, \tag{4.3}$$

which guarantees the consistence of Eq. (1.3b) with respect to parity. The direct consequence of such fermion properties is that the even configuration of the boson field, similar to (2.17),

$$\varphi(x) = \begin{cases} +2\lambda(x - x_1), & x_1 \le x \le x_2, \\ -2\lambda(x + x_1), & -x_2 \le x \le -x_1, \end{cases} \tag{4.4}$$

is not an exact solution of Eqs. (1.3), since in this case $\langle J_5(x)\rangle_{\text{sea}} \not\equiv 0$ in domain II.

Nevertheless, the configuration (4.4) plays an important role in the study of the nontopological case. First of all, for $g \ll 1$ it turns out to be a rather good approximation to the precise solution. To argue this statement, let us note firstly that the replacement $\varphi = \tilde{\varphi}/g$ removes $g$ from Eq. (1.3a), while Eq. (1.3b) will contain $g$ only as a coefficient in the r.h.s., namely,

$$\tilde{\varphi}'' = ig^2\frac{M}{2}\langle\left[\bar{\psi}, \gamma_5\, \mathrm{e}^{i\gamma_5\tilde{\varphi}}\psi\right]_-\rangle. \tag{4.5}$$

Assuming further that the potential $V(\varphi)$ depends on $g$ as

$$V(\varphi) = W(g\varphi)/g^2, \tag{4.6}$$

where $W(f)$ should be an even polynom to maintain the (anti)symmetry of soliton solutions, for small $g$ there appears a quite natural expansion in powers of $g^2$ in the problem. Within this expansion, the zero-order approximation for the rescaled boson field $\tilde{\varphi}(x)$ is the configuration (4.4) in domain II, $\tilde{\varphi}(x) \equiv 0$ in domain I, while in domain III it is given by the even soliton solution of Eq. (1.4b). As in the topological case, to simplify calculations we retain only the asymptotics of this solution, which means

$$\tilde{\varphi}_{\text{sol}}(x) = \pi\left(1 - A\,\mathrm{e}^{-m|x|}\right), \quad |x| > x_2. \tag{4.7}$$

Merging (4.4) and (4.7) via continuity of $\varphi$ and $\varphi'$ gives rise to the following relation:

$$2\lambda = \frac{\pi m}{md + 1}, \tag{4.8}$$

whence for the energy of the boson field one finds

$$E_{\tilde{\varphi}} = \frac{\pi^2 m}{md+1}. \tag{4.9}$$

(By returning to the initial $\varphi$ the dependence on $g$ in $E_\varphi$ is restored by adding the coefficient $1/g^2$.)

Now let us show that the first-order $O(g^2)$ correction to the energy of the boson field (4.9) vanishes exactly for any current in the r.h.s. of Eq. (4.5), provided the asymptotics (4.7) for the boson field in domain III remains valid beyond the perturbation expansion in $g^2$, which implies that the corrections caused by the r.h.s. of (4.5) could disturb solely the value of the parameter $A$. Further, we shall consider only the positive semiaxis. The contribution of the negative one is exactly the same.

From the relation (4.7) we derive

$$m\tilde{\varphi}(x_2) + \tilde{\varphi}'(x_2) = \pi m, \tag{4.10}$$

while in domain III

$$\tilde{\varphi}'_{\mathrm{III}}(x) = \tilde{\varphi}'(x_2)\, \mathrm{e}^{-m(x-x_2)}, \tag{4.11}$$

which is valid beyond the $g^2$-expansion as well. Using the virial theorem, which is also relevant beyond this expansion, we obtain the following general expression for the contribution of domain III to $E_{\tilde{\varphi}}$:

$$E_{\tilde{\varphi}\,\mathrm{III}} = \int\limits_{\mathrm{III}} dx\ \tilde{\varphi}'^2 = \frac{\left(\tilde{\varphi}'(x_2)\right)^2}{2m}. \tag{4.12}$$

Proceeding further, on account of the first-order correction from the nonvanishing $\langle J_5(x)\rangle$ one obtains for the boson field in domain II

$$\tilde{\varphi}(x) = 2\lambda(x - x_1) + g^2\tilde{\varphi}_1(x). \tag{4.13}$$

At the same time, it follows from the condition $\tilde{\varphi}_{\mathrm{I}}(x) \equiv 0$ and the boundary conditions (4.10) that

$$\tilde{\varphi}_1(x_1) = 0, \quad m\tilde{\varphi}_1(x_2) + \tilde{\varphi}'_1(x_2) = 0. \tag{4.14}$$

Then for the boson field energy in domain II with the first $O(g^2)$ correction, one finds

$$E_{\tilde{\varphi}\,\mathrm{II}} = \frac{1}{2}\int\limits_{\mathrm{II}} dx\ \tilde{\varphi}'^2 = 2\lambda\left(\lambda d + g^2\tilde{\varphi}_1(x_2)\right). \tag{4.15}$$

On the other hand, it follows in the same approximation from (4.12) and (4.13) that

$$E_{\tilde{\varphi}\,\mathrm{III}} = \frac{2\lambda}{m}\left(\lambda + g^2\tilde{\varphi}'_1(x_2)\right). \tag{4.16}$$

Returning to Eq. (4.14), one finds that in the sum $E_{\tilde{\varphi}\,\mathrm{II}} + E_{\tilde{\varphi}\,\mathrm{III}}$ the contribution of $\tilde{\varphi}_1$ vanishes. In other words, within the $g^2$-expansion the corrections to the leading approximation (4.9) in $E_{\tilde{\varphi}}$, caused by the nonvanishing $\langle J_5(x)\rangle$, start from the second-order $O(g^4)$ only.

At the same time, for fermions the leading order of $g^2$-expansion is $O(g^0)$. In this approximation the spectral problem (1.6)–(1.9) leads to the following equation for the fermionic spectrum:

$$\exp(4i\omega x_1) = \left[\frac{\nu_- + k_-}{\nu_+ + k_+}\right] \frac{1 - \mathrm{e}^{-2ik_+ d}\dfrac{M - i(\nu_+ + k_+)}{M - i(\nu_+ - k_+)}}{1 - \mathrm{e}^{-2ik_+ d}\dfrac{M + i(\nu_+ - k_+)}{M + i(\nu_+ + k_+)}} \frac{1 - \mathrm{e}^{2ik_- d}\dfrac{M - i(\nu_- - k_-)}{M - i(\nu_- + k_-)}}{1 - \mathrm{e}^{2ik_- d}\dfrac{M + i(\nu_- + k_-)}{M + i(\nu_- - k_-)}}, \tag{4.17}$$

where $\nu_\pm = \omega \pm \lambda$, $\nu_\pm^2 = k_\pm^2 + M^2$. The total energy of the bag is still given by the sum (3.5), where the fermion energy has the form

$$E_\psi = -\sum_{\omega_n < 0} \omega_n. \tag{4.18}$$

Like in (3.8), in (4.18) the inequality $\omega_n < 0$ is strict, because for the configuration (4.4) there are no levels with $\omega_n = 0$ for any values of $x_1, x_2$.

Finally, after restoring the dependence on $g^2$ in $E_\varphi$ we obtain the following expression for the total energy of the bag:

$$E_{\mathrm{bag}} = \frac{\pi^2}{g^2}\,\frac{m}{md+1} + E_\psi + O(g^2), \tag{4.19}$$

where the two first leading terms in $E_{\mathrm{bag}}$ — the bosonic $O(1/g^2)$ and fermionic $O(g^0)$ — are determined by the zero-order approximation for the boson field (4.4), (4.7) only, while the corrections start with $O(g^2)$ terms, at once in the bosonic and fermionic parts of the total energy. Moreover, the considerable simplicity of Eq. (4.17) makes it possible to analyze the fermionic spectrum in a semianalytical way, which in turn allows one to use the configuration (4.4), (4.7) as a trial one for a qualitative study of the nontopological bag properties for even larger values $g \simeq 1$.

Thus, in further analysis of the main properties of the nontopological bag we shall use the first two terms in the total energy (4.19), which can be found directly from the configuration (4.4), (4.7). Recalculating $E_\varphi$ to dimensionless variables, introduced in (3.11), (3.14)–(3.16), one obtains

$$\mathcal{E}_{\mathrm{bag}}(\alpha, \beta) = \mathcal{E}_\psi(\alpha, \beta) + \frac{\pi^2}{g^2}\frac{2\mu}{\mu\beta + 1}, \tag{4.20}$$

where $\alpha$, $\beta$ are now independent parameters. So the study of the bag's energy as a function of its geometry becomes a qualitatively different problem of finding the two-dimensional surface $\mathcal{E}_{\mathrm{bag}}(\alpha, \beta)$.

The extraction of the finite part from $\mathcal{E}_\psi(\alpha, \beta)$ undergoes the same main stages as in the topological case, but reveals some peculiar features, caused by the independence of $\alpha$, $\beta$. After some algebra the UV asymptotics of the energy levels can be presented in the form

$$\varepsilon_n(\alpha, \beta) = \frac{\pi/2 + \pi n}{\rho} + \frac{(-1)^{n+1}\cos(2\lambda d)\sin[(\pi/2 + \pi n)\alpha/\rho] + 1 + \beta/2}{\pi/2 + \pi n} + O(1/n^2). \tag{4.21}$$

From the structure of the logarithmic term in (4.21) we immediately deduce that, as for the topological case, the renormalized via asymptotics $\tilde{\mathcal{E}}_\psi$, and so $\mathcal{E}_{\rm bag}$, acquire the logarithmic divergence $(-\ln\beta/\pi)$ for $\beta \to 0$. Besides this, $\tilde{\mathcal{E}}_\psi$ and $\mathcal{E}_{\rm bag}$ increase for $\beta \to \infty$ and finite $\alpha$. Since $\rho$ grows together with $\beta$, this effect turns out to be quite similar to the increase of $\tilde{\mathcal{E}}_\psi$ and $\mathcal{E}_{\rm bag}$ for $\rho \to \infty$ in the topological case: in the UV domain the difference between $\nu_+$ and $\nu_-$ vanishes and Eq. (4.17) turns into (2.9). Thereon to analyze the renormalized $\tilde{\mathcal{E}}_\psi$ one may use the integral approximation (3.31), (3.32), in which for $\beta \to \infty$ the main term in the integrand of $\tilde{\mathcal{E}}_\psi$ is positive and proportional to $\beta$.

The behavior of $\mathcal{E}_\psi$ and $\mathcal{E}_{\rm bag}$ for $\alpha \to \infty$ and finite $\beta$ requires special consideration, since in this case the logarithmic sine-term in asymptotics (4.21) becomes significant again, but, unlike the case of $\beta \to 0$, there appears now an additional factor $\cos(2\lambda d)$. Since $2\lambda d = \pi\mu\beta/(\mu\beta+1)$, the sign of this multiplier can be either positive or negative depending on the current value of $\beta$. However, in this limit another effect comes into play, namely, the proportional to $\alpha$ increase of the number of levels on the branches of the fermionic spectrum that correspond to the imaginary values of $k_\pm$ in (4.17), where $0 < \nu_\pm \le M$. Directly for Eq. (4.17) this effect shows up in an intricate enough way due to the presence of separate branches for imaginary $k_+$ and $k_-$ and therefore can be analyzed in detail only numerically, but its essence could be understood quite simply, if we neglect for a while the difference between $k_+$ and $k_-$. Then we are left with only one branch with $0 < \nu_n \le M$ determined from Eq. (3.13). For $\alpha \to \infty$ the spectrum of energy levels belonging to this branch becomes quasicontinuous with the interval between the levels of order $\pi/\alpha$, hence $\sum_n \varepsilon_n$ over this branch can be approximated by the integral

$$\sum_{0<\nu_n\le M} \varepsilon_n \to -\frac{1}{\pi}\int_0^1 dx\,\sqrt{1-x^2}\left[-\frac{\alpha x}{\sqrt{1-x^2}}+\right.$$

$$\left.+\frac{x\left(\beta+1/(1-x^2)\right)-\sinh\left(\beta x+\gamma\right)/\sqrt{1-x^2}}{\cosh\left(\beta x+\gamma\right)-\sqrt{1-x^2}}\right]. \tag{4.22}$$

From (4.22) one can easily see that for $\alpha \to \infty$ the contribution of these levels to $\sum_n \varepsilon_n$ takes the form $\alpha/2\pi$ + finite terms depending on $\beta$ only. Transforming further the relevant terms in the subtracted sum to the integral, one obtains

$$\int_{\pi/2}^{\alpha} dx\,\left(\frac{x}{\rho}+\frac{1+\beta/2}{x}\right), \tag{4.23}$$

whence it follows that for $\alpha \to \infty$ the main terms in the subtracted sum should be

$$\frac{\alpha^2}{2\pi\rho}+\frac{1+\beta/2}{\pi}\ln\alpha. \tag{4.24}$$

The leading terms in Eqs. (4.22), (4.24) cancel each other, so in this limit after subtraction the contribution of the branch with $0 < \nu_n \le M$ to the renormalized $\tilde{\mathcal{E}}_\psi$ becomes $(1/\pi)(1+\beta/2)\ln\alpha$ + finite terms. For the case of separate branches for $k_+$ and $k_-$ the general features of their asymptotic behavior for $\alpha \to \infty$ remain the same. As a result, after combining

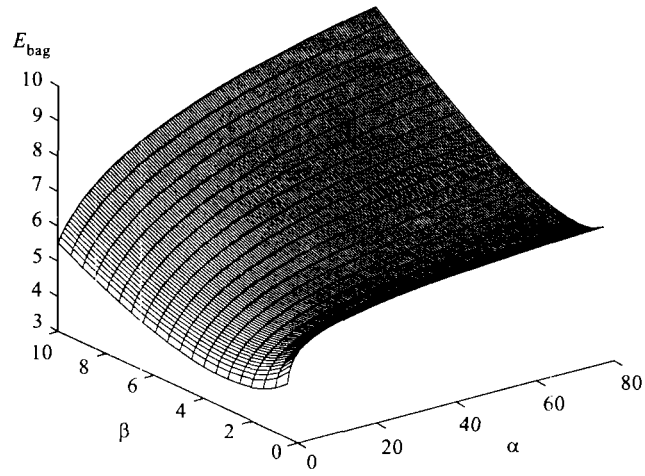


Fig. 4. The profile of the surface $\mathcal{E}_{\text{bag}}(\alpha, \beta)$

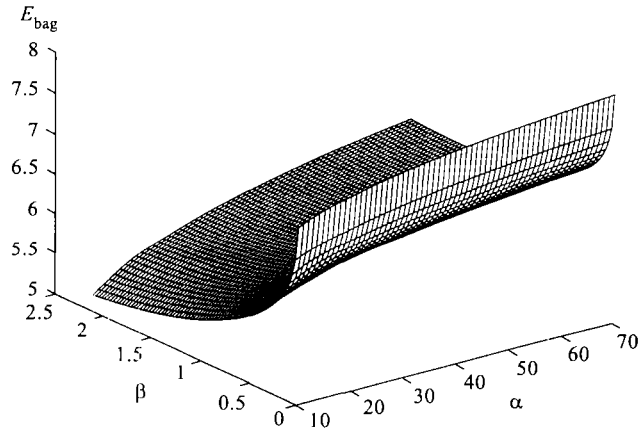


Fig. 5. The profile of the surface $\mathcal{E}_{\text{bag}}(\alpha, \beta)$, rescaled to observe the behavior for small $\beta$

this asymptotics with the corresponding input of the logarithmic term in the UV asymptotics (4.21), for the leading term in $\mathcal{E}_\psi$ for $\alpha \to \infty$ one finds

$$\frac{1}{\pi}(1 + \beta/2 + \cos 2\lambda d)\ \ln\alpha, \quad \alpha \to \infty, \tag{4.25}$$

which is definitely positive for all $\beta$. So in this limit the bag's energy also grows, but now proportionally to $\ln\alpha$.

The numerical calculation, performed for the same values $\mu = 0.25$ and $g = 1$ as for the topological bags, confirms such behavior of $\tilde{\mathcal{E}}_\psi$ and $\mathcal{E}_{\text{bag}}$. Moreover, the calculation shows that there is not any nontrivial minimum in the total energy for the nontopological case at all,

while the minimal value of energy is achieved for the configuration with vanishing size of the phase of asymptotic freedom and for finite nonzero $\beta$, which is clearly seen from Figs. 4, 5, where the profiles of the 2D surfaces $\mathcal{E}_{\text{bag}}(\alpha, \beta)$ are presented in different scales. So for the bags with zero topological charge the considered three-phase model predicts that the main role should be played by the intermediate phase of constituent quarks, which is quite consistent with semiphenomenological quark models of mesons [9, 33].

## CONCLUSION

This work is aimed at the construction of a three-phase version of a hybrid chiral bag, wherein first the initially free, almost massless current quarks transmute into «dressed», due to interaction, massive constituent quarks with the same quantum numbers, and only afterwards there emerges a purely mesonic colorless phase. Our results show that such a model can be formulated in a quite consistent fashion and leads to reasonable behavior of the total bag's energy as a function of its size, which takes the form of an infinitely deep potential well with a distinct minimum in the topological case, whereas in the nontopological case the minimal energy of the bag corresponds to the configuration in which the phase of asymptotic freedom disappears.

The specific feature of this model is a substantially enhanced influence of the fermion vacuum polarization on the bag properties. In particular, in this case the Dirac sea polarization itself produces the infinite increase of energy at large distances. Another essential trait is the appearance of infinite interaction energy between fermions and bag boundaries (i.e., confining potential) for $d \neq 0$, which means that the size of the intermediate domain does not actually vanish, although on the level of the initial Lagrangian the formal limit $d \to 0$ exists and describes a two-phase HCBM. In other words, such a three-phase model cannot be continuously transformed into a two-phase one, which is the ultimate reason of its remarkably different features.

It is worthwhile to mention once more the question of the choice of method for calculation of the Dirac sea averages for fermion bags. The method we used is based on the discreteness of the fermionic energy spectrum, which by means of quite obvious considerations leads to very simple solution of coupled equations of the bag in the intermediate domain. Let us remark, however, that, despite arguments in favor of such a method of calculation of sea averages, we cannot completely reject alternative methods like the thermal regularization. The question of which one is more adequate to the physics of the problem should be answered only through detailed study of realistic models.

It should also be emphasized that by constructing such a three-phase model we have substantially leant on the requirement of Lorentz covariance. The initial formulation of the model, where $\theta$ fields are restored, is a local field theory [10], and, regardless of the diversity of classical solutions one needs to deal with, the covariance is broken only spontaneously and so can be freely restored by means of methods of Refs. [21] based on the covariant center-of-mass variables for a localized quantum-field system. However, such an explicitly covariant framework requires some essential changes in the calculation techniques, since the invariant dynamics of fields acquires a specific finite-difference form [21], and so will be considered separately.

This work was supported in part by RFBR under Grant 00-15-96577 and by Saint-Petersburg Concurrency Centre of Fundamental Sciences, Grant 00-0-6.3-24.

## REFERENCES

1. *Bogoliubov P. N.* // Ann. Inst. H. Poincare. 1967. V. 8. P. 163;
   *Bogoliubov P. N., Dorokhov A. E.* // Sov. J. Part. Nucl. 1987. V. 18. P. 391.

2. *Chodos A. et al.* // Phys. Rev. D. 1974. V. 9. P. 3471;
   *Chodos A. et al.* // Ibid. V. 10. P. 2559;
   *DeGrand T. et al.* // Phys. Rev. D. 1975. V. 12. P. 2060.

3. *Chodos A., Thorn C. B.* // Phys. Rev. D. 1975. V. 11. P. 2733;
   *Inoue T., Maskawa T.* // Progr. Theor. Phys. 1975. V. 54. P. 1853.

4. *Bardeen W. A. et al.* // Phys. Rev. D. V. 11. 1975. P. 1094.

5. *Brown G. E., Rho M.* // Phys. Lett. B. 1979. V. 82. P. 177;
   *Vento V. et al.* // Nucl. Phys. A. 1980. V. 345. P. 413.

6. *Rho M.* // Phys. Rep. 1994. V. 240. P. 1.

7. *Hosaka H., Toki O.* // Phys. Rep. 1996. V. 277. P. 65.

8. *Zahed I., Brown G. E.* // Phys. Rep. 1986. V. 142. P. 1;
   *Holzwarth G., Schwesinger B.* // Rep. Progr. Phys. 1986. V. 49. P. 825.

9. *Gasiorowicz S., Rosner J. L.* // Am. J. Phys. 1981. V. 49. P. 1954;
   *Montanet L. et al.* // Phys. Rev. D. 1994. V. 50. P. 1173;
   *Povh B. et al.* Particles and Nuclei. Berlin: Springer, 1995.

10. *Sveshnikov K., Silaev P.* // Theor. Meth. Phys. 1998. V. 117. P. 263.

11. *Cherednikov I. et al.* // Nucl. Phys. A. 2000. V. 676. P. 339.

12. *Théberge S., Thomas A. W., Miller G. A.* // Phys. Rev. D. 1980. V. 22. P. 2838; 1981. V. 24. P. 216.

13. *Thomas A. W.* // Adv. Nucl. Phys. 1984. V. 13. P. 1.

14. *Miller G. A.* // Int. Rev. Nucl. Phys. 1984. V. 2. P. 190.

15. *Kahana S., Ripka G., Soni V.* // Nucl. Phys. A. 1984. V. 415. P. 351.

16. *Banerjee M. K., Broniowski W., Cohen T. D.* Chiral Solitons / Ed. by K. F. Liu. Singapore: World Scientific, 1987.

17. *Diakonov D. I., Petrov V. Yu., Povilitsa P. V.* // Nucl. Phys. B. 1988. V. 306. P. 809.

18. *Birse M. C.* // Progr. Part. Nucl. Phys. 1991. V. 25. P. 1.

19. *Alkofer R., Reinhardt H., Weigel H.* // Phys. Rep. 1996. V. 265. V. 139.

20. *Creutz M.* // Phys. Rev. D. 1974. V. 10. P. 1749;
   *Creutz M., Soh K.* // Phys. Rev. D. 1975. V. 12. P. 443.

21. *Sveshnikov K.* // Phys. Lett. A. 1989. V. 136. P. 1; Teor. Mat. Fiz. 1990. V. 82. P. 55.

22. *Perry R., Rho M.* // Phys. Rev. D. 1986. V. 34. P. 1169.

23. *Campbell D. K., Liao Y.-T.* // Phys. Rev. D. 1976. V. 14. P. 2093.

24. *Niemi A. J., Semenoff G. W.* // Phys. Rep. 1986. V. 135. P. 99.

25. *Malakhov I., Sveshnikov K.* To be published in «Theor. Math. Phys.».

26. *Daschen R., Hasslacher B., Neveu A.* // Phys. Rev. D. 1975. V. 12. P. 2443.

27. *Jackson A. D., Rho M.* // Phys. Lett. B. 1986. V. 173. P. 217; 220;
*Jackson A. D., Vepstas L.* // Phys. Rep. 1990. V. 187. P. 109.

28. *Mulders P. J.* // Phys. Rev. D. 1984. V. 30. P. 1073.

29. *Plumien G., Muller B., Greiner W.* // Phys. Rep. 1986. V. 134. P. 87.

30. *Elizalde E., Bordag M., Kirsten K.* // J. Math. Phys. 1996. V. 37. P. 895;
*Elizalde E. et al.* // J. Phys. A. 1998. V. 31. P. 1743.

31. *Falomir H., DeFrancia M., Santangelo E. M.* // Phys. Lett. B. 1996. V. 371. P. 285.

32. *Bordag M., Mohideen U., Mostepanenko V.* // Phys. Rep. 2001. V. 353. P. 1.

33. *Lavelle M., McMillan D.* // Phys. Rep. 1997. V. 279. P. 1.

Received on September 11, 2002.

Письма в ЭЧАЯ. 2002. №4[113] Particles and Nuclei, Letters. 2002. No.4[113]

УДК 539.1.07: 528.41

# COMPARISON OF ATLAS TILECAL MODULE No. 8 HIGH-PRECISION METROLOGY MEASUREMENT RESULTS OBTAINED BY LASER (JINR) AND PHOTOGRAMMETRIC (CERN) METHODS

*V. Batusov* [a], *J. Budagov* [a], *J. C. Gayde* [b], *J. Khubua* [a], *C. Lasseur* [b], *M. Lyablin* [a], *L. Miralles Verge* [c], *M. Nessi* [b], *N. Rusakovich* [a], *A. Sissakian* [a], *N. Topiline* [a]

[a] Joint Institute for Nuclear Research, Dubna

[b] CERN, Geneva

[c] IFAE, Barcelona

The high-precision assembly of large experimental set-ups is of a principal necessity for the successful execution of the forthcoming LHC research programme in the TeV-beams. The creation of an adequate survey and control metrology method is an essential part of the detector construction scenario. This work contains the dimension measurement data for ATLAS hadron calorimeter MODULE No. 8 (6 m, 22 tons) which were obtained by laser and by photogrammetry methods. The comparative data analysis demonstrates the measurements agreement within $\pm 70$ $\mu$m. It means, these two clearly independent methods can be combined and lead to the rise of a new-generation engineering culture: high-precision metrology when precision assembling of large scale massive objects.

Для успешного выполнения предстоящей исследовательской программы LHC на ТэВ-ном пучке необходима высокоточная сборка крупногабаритных экспериментальных установок. Создание адекватного метрологического метода обзора и контроля — важная часть подготовки сценария создания детекторов. Работа содержит данные обмера модуля №8 (6 м, 22 т) адронного тайл-калориметра установки ATLAS, полученные лазерным и фотограмметрическим методами. Сравнительный анализ данных показывает, что точность совпадения выполненных измерений составляет $\pm 70$ мкм. Это означает, что рассматриваемые два независимых метода могут быть объединены для создания инженерной метрологии нового поколения — прецизионной сборки крупногабаритных, массивных объектов.

## INTRODUCTION

The ATLAS hadron tile-calorimeter is composed [1] of one central barrel and two extended barrels (Fig. 1). Radially the tile-calorimeter extends from an inner 2.8 m to an outer 4.25 m radius. Azimuthally, the barrel and extended barrels are divided into 64 MODULES. Dubna began mass production of barrel modules in April 1999. To guarantee very high MODULES assembly precision, we proposed, developed and practically applied a new unique laser control system [2, 3]. The laser control system instrumentation and a brief description of the method see in Appendices 1 and 2.

In January 2000, the JINR and CERN groups measured the ATLAS tile-calorimeter MODULE No. 8 dimensions by the laser and photogrammetric methods at CERN.

The photogrammetric instrumentation and method are documented in Appendix 3.

During these measurements the MODULE was kept at the same position which allowed one to obtain the data for comparison of both methods. Clearly, these measurement methods are fully independent.

It must be also noted that the MODULE No. 8 was measured by standard surveying method using theodolites for industrial 3D metrology before the application of the photogrammetric method; the standard deviation ($1\sigma$) according to the DIN 18723 norm is given to 0.15 mgon (0.5°) for measurements of both horizontal and vertical angles. See the results on http://edms.cern.ch/document/309991/1

A small reference network was arranged around the MODULE in such a way that the theodolites sights were nearly parallel to the faces: therefore, the accuracy for the coordinate perpendicular to the face was given by the high-precision angle measurements.

The survey results for both the geometric methods and the comparisons have been documented in the reports noted in Appendix 4.

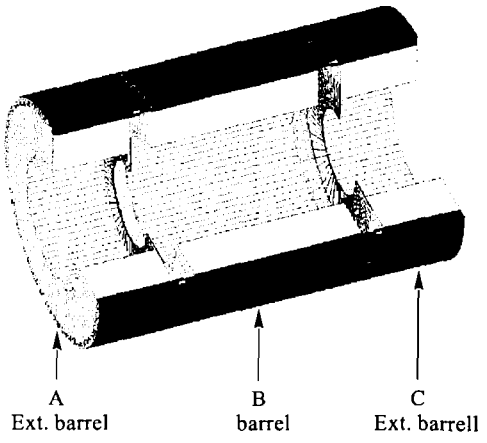


Fig. 1. The tile-calorimeter barrel and two extended barrels

In two sets of measurements (photo and laser) we had the following four measurement lines (common for both methods) on the MODULE surface [3] (see Fig. 2):

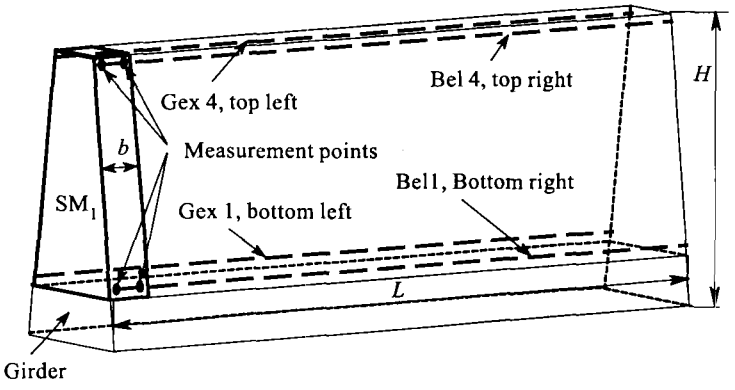


Fig. 2. Measurement lines on the MODULE surface

— Bottom-left line[1] of the laser method coincides with the bottom-left line Gex 1[2] of the photogrammetric method;

— Top-left line coincides with Gex 4;

— Bottom-right line[1] coincides with Bel 1[3];

— Top-right line coincides with Bel 4.

Comparison was made only along these lines.

In the photogrammetric method the measurement points were located (Fig. 2) on the submodule (SM) surface at a distance of $1/4 \times b$ from the submodule edge ($b$ is the submodule width). The MODULE height $H = 1940$ mm and its length $L = 5600$ mm.

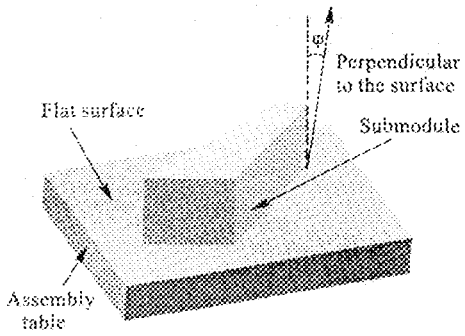


Fig. 3. Definition of submodule maximal twist angle $\varphi$

In the laser method the measurement points were located on the submodule edges. This location of the measurement points was motivated by the presence of the submodule twist angle $\varphi$ (Fig. 3) and, consequently, only at such a positioning one can detect (observe) the parts, going farthest beyond the limits of the MODULE. We note that the top-lines data will expectedly demonstrate the largest discrepancies in comparison with the bottom-lines data as it is in the narrow part of the submodule where one observes the maximal twist angles $\varphi$ reaching the value of $10^{-4}$ rad.

## 1. COORDINATE SYSTEMS (CS)

**Requirements to the CS.** When choosing CS, it seems natural to fix it to some element of the MODULE. It should be taken into account that the dimensions and shape (form) of such element (surface, edge) may differ from its shop-drawing dimensions (nonflat, not straight-lined, twisted, etc.).

As a result, systematic errors may arise and deteriorate final measurement precision.

In this sense it seems essential that the systematic error should be at worse comparable with the measurement precision. Otherwise the choice of the CS can give a distorted idea of the MODULES measured.

**CS of JINR Laser Method.** The choice of the CS is determined by the Dubna technology of the MODULE assembly [1]. The centre «$0_L$» of the CS is chosen in the middle of the bottom edge of the girder base surface from the side of submodule 1 (see Fig. 4).

• The $Y_L$ axis goes along the line, which connects the point $0_L$, and point «$N$», which is the middle (centre) of the bottom base of the girder at the side of submodule 19.

---

[1] The left (right) side of the MODULE is the side on the left (right) of the observer looking from the $SM_1$ along the MODULE.

[2] Direction to the town Gex.

[3] Direction to the town Bellegarde.

• The $Z_L$ axis goes along the line connecting the point $0_L$ and point «$M$» in the middle of the edge of the narrow part of the special submodule from the side of the endplate.

• The $X_L$ axis is perpendicular to the $Z_L$ and $Y_L$ axes.

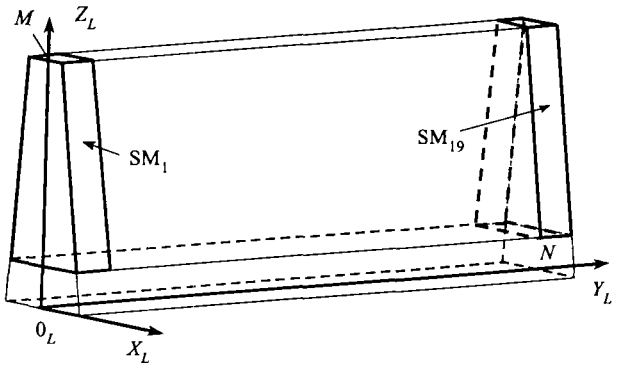


Fig. 4. Coordinate system of the laser method

**CS of the CERN Photogrammetric Method and Measured Points.** The four extreme corners of the girder were measured and set in the same horizontal plane within a max.–min. of 0.1 mm with using a precise optical level (precision of a direct measurement is 30 $\mu$, then precision of a vertical difference between 2 corners is 42 $\mu$).

The distances between the corners were measured within an accuracy of 0.1 mm using a precise electro-optical distancemeter associated with a metrological class theodolite as mentioned above. Then the coordinate system for the photogrammetry is referred to the plane of the girder, set horizontal, and to the four corners of the girder, altogether within 0.1 mm; so that margin value is referred to the procedure of setting the four extreme corners of the girder horizontal by using a precise optical level.

The coordinate centre «$0_P$» is the centroid of the four bottom corners of the girder (Fig. 5).

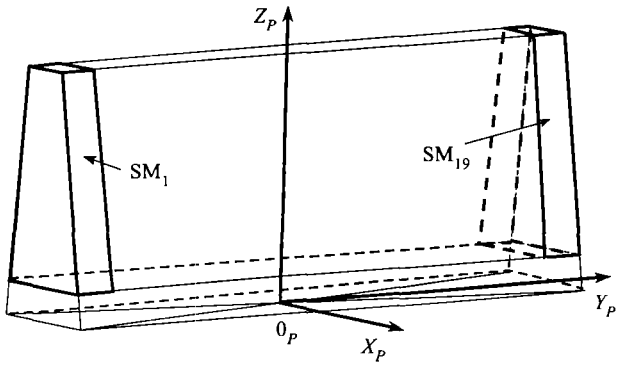


Fig. 5. Coordinate system of the photogrammetric method

• The $Y_P$ axis is in the mean plane of the four corners and parallel to the girder longitudinal axis.

• The $Z_P$ axis is perpendicular to the mean plane of the four corners.

• The $X_P$ axis is in the mean plane of the four corners at the origin and perpendicular to the $Y_P$ axis.

The plane $X_P 0_P Y_P$ is horizontal within 0.1 mm, i.e., 0.02 mrad as a longitudinal tilt angle and 0.2 mrad as a transversal tilt angle; the $Z_P$ axis is vertical within the same accuracy along the two angular components.

Despite the accuracy of the photogrammetric process, within 50 $\mu$ spatially at $1\sigma$, and in order to include the uncertainty on the definition of the CS, all the results documented in the reports were given within 100 $\mu$ accuracy.

In fact the four corners, measured by standard precise level and metrological class theodolite, were also measured by photogrammetry so that the coordinates given by that method were directly expressed in the CS as described above.

Each submodule was equipped with 16 coded retroreflective targets ($3 \times 3$ cm), 8 on each side and arranged by two at four levels quoted respectively at 0.35, 0.88, 1.44, and 1.77 m from the reference mean plane of the four corners measured and set horizontal as described above. That regular arrangement permitted one to calculate the thickness of the module at each level, to give the median plane at each level, i.e., the misalignment with respect to the reference axis of the girder and then the spatial banana shape of the entire MODULE. Finally there were 152 points measured on each side for the definition of the MODULE envelope and its geometrical parameters, all referred to the girder as defined above.

In addition to these parameters, the best fit plane was calculated for each side as well as the differences for each point to the mean plane so that the max. and min. values were identified easily. The wedge angle was calculated for the entire MODULE and could be extracted for each submodule.

*Comments on the CS of the CERN photogrammetric method.* 1. The girder may have the following (compared with the drawing) distortions measured at JINR by the Dubna survey group:

• The girder may have the «twist» angle $\varphi_G$ (Fig. 6); we measured this angle by the minilevel: $\varphi_G = 10^{-4}$ rad.

• The girder may have a banana shape (Fig. 7).

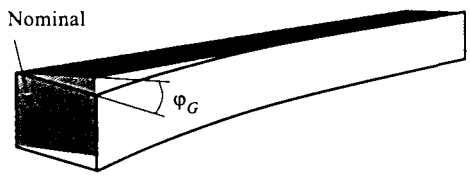


Fig. 6. «Twist» of the girder


Fig. 7. Sagging («banana») of the girder

Sagging may reach a value of $\delta = 0.6$ mm. As the girder bottom surface is not flat, the possible final effect is that the CS can be not orthogonal. It seems to us that this is practically

impossible to take this effect into account as one cannot determine the shape of the bottom girder base (down plane) for the already assembled MODULE.

2. The lines of the long side edges of the bottom girder base are not straight-lined and sagging may reach $\delta_{\max} = 0.6$ mm (Fig. 8).

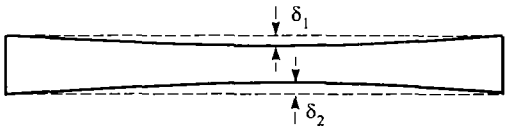


Fig. 8. Sagging of side edges of the girder bottom base

The difference $\delta_1 \neq \delta_2$ may lead to the asymmetric location of the coordinate centre $0_P$.

3. As was already said, the girder arrived from Romania with some residual «twist» along the longitudinal axis and this twist may reach $\varphi_G = \pm 2 \cdot 10^{-4}$ rad (our data for girder 12). One can measure the twist before the MODULE is assembled, or before submodules are positioned. After the MODULE is fully assembled, the twist amplitude will change in an uncontrolled manner. If, however, one assumes that this change is insignificant, one can conclude that the vertical axis of the girder is oriented to the angle $\varphi_K = \pm 2 \cdot 10^{-4}$ rad relative to the vertical axis of the submodule (see Fig. 9). This effect (twisting of the girder) will finally influence the photogrammetric data: the measured «distance» (distance from the ideal MODULE surface to the nearest points of the real MODULE) will be larger on the one side of the MODULE and smaller on the other. In other words, the pseudo-worsening of the photogrammetric measurement data will take place.

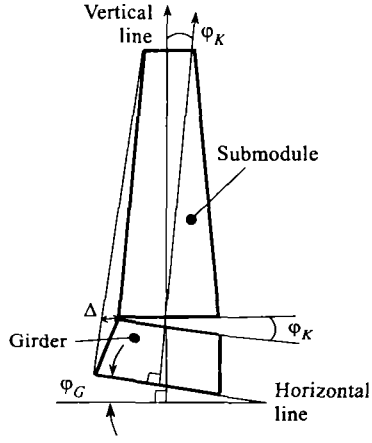


Fig. 9. Relative position of the submodule and of the «twisted» girder

It must be noted at that stage that one advantage of the photogrammetric method is to give a full complete geometrical envelope of the MODULE referred to a proper reference attached to the object itself, namely, the girder which is the real backbone of the assembly of the MODULES. See the section on the measured points.

*Comments on the CS of the JINR laser method.* According to «item 3» (see above) the systematic error will appear in determination of the coordinates of the bottom-line along the $X$ axis. The magnitude of this error (for maximal observed $\theta = \pm 2 \cdot 10^{-4}$ rad of the girder twist) will be $\Delta = 60$ $\mu$m, which is compatible with the measurement precision. Note that following the MODULE assembling technology, the girder is to be positioned on the base unit in such a way that its «twist» must be symmetric about horizontal line (Fig. 9).

## 2. DATA PRESENTATION

The results of both methods are presented in the form of the table (see Appendix 5) of deviation of the measured points from the surface of the nominal MODULE (Fig. 10).

— Top size «$A$» is the size that coincides with the width of the narrow part of the master plates in the indicated place.

— The «1–2–3–4» contour coincides with the contour of the master plates.

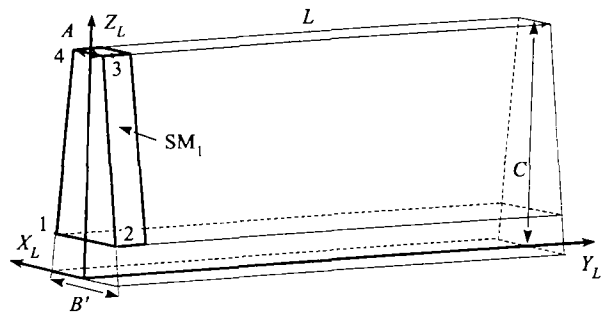


Fig. 10. Position of the nominal MODULE in the laser method coordinate system

For the laser method the dimensions of the nominal MODULE are:

$A = 223.31$ mm, top (narrow) base;

$B = 408.80$ mm, bottom (wide) base;

$C = 1942$ mm, height;

$L = 5600$ mm, length;

$B' = 414.16$ mm, theoretical dimension derivable as a result of master plates imaginary extension on the 1942 mm height.

The nominal MODULE must be positioned in such a way that positive maximal deviations of both sides of MODULE became equal (sort of «symmetrization» of the positive deviations).

## 3. RESULTS OF COMPARISON

**Transformation of the Laser Data to the Photogrammetric Data.** Figure 11 presents nontransformed (primary) data for both methods (see item 1 of the comments on the CS of the photogrammetric method). Recall that the twist angle $\varphi = \pm 2 \cdot 10^{-4}$ was determined for the girder of MODULE No. 10.

We find it rather logical to assume that the MODULE No. 8 twist is also $\varphi \approx \pm 10^{-4}$.

If so, one may expect that (attention!) MODULE No. 8 in the laser measurements will be turned as a whole by an angle of $\approx 10^{-4}$ rad as compared with the photogrammetric method.

This assumption is confirmed by the measurement data disposition (Fig. 11). Indeed, if one turns the laser set of measurements by an angle $\theta_0 = 0.8 \cdot 10^{-4}$ along the $Y$ axis, the laser data set practically coincides with the photogrammetric series.

One more disagreement between the data of both methods is clearly visible (see Appendix 5). The envelope top overall size chosen in the photogrammetric method (the $A$ value in Fig. 10) is 0.3 mm narrower than in the laser method (see Appendix 5).

Direct caliper measurements of the outer dimensions of the master plates on the narrow part (these are the dimensions which determine the envelope top overall dimension) indicate that the master plates were manufactured about 0.3–0.4 mm smaller than the nominal size. It is in favor of the overall dimension chosen in the laser method (see item 3).

To reach the most complete data coincidence we turned the laser data by an angle $\theta_0 = 0.8 \cdot 10^{-4}$ rad with respect to $Z$ axis and also made the overall dimension noncontradicting in

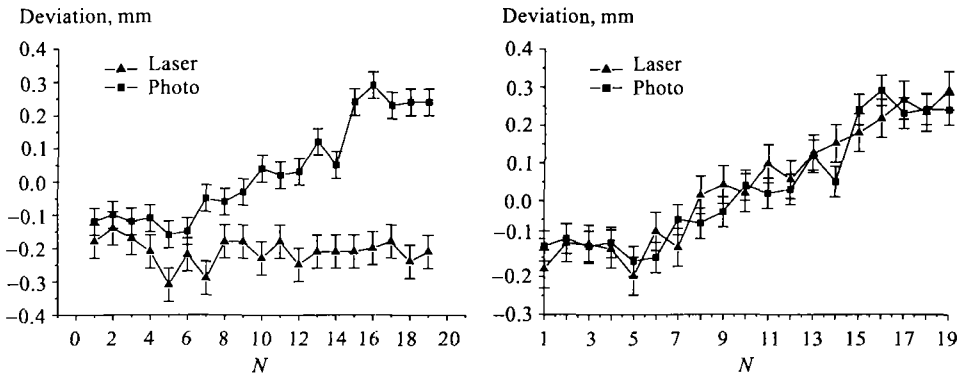


Fig. 11. Line Bel 1 measurement data by the photogrammetric and laser bottom-right methods with no correction applied for MODULE No. 8

Fig. 12. The same as in Fig. 11 but after correction (turn by $0.8 \cdot 10^{-4}$ rad)

both methods (Fig. 12). The value obtained for $\theta_0$ agrees with the above estimate correction angle $\approx 10^{-4}$ rad.

In Figs. 11, 12 the data analysis shows good agreement for the shapes of the curves, too. Appendix 6 represents a very full data set and shows that after «turning» correction (see above) laser and photogrammetric results are in agreement with the precision quoted on the hystogram. The $\sigma$ value of the distribution of $D_L - D_P$ differences (or «distances»), measured by the laser and photogrammetric methods is: $\sigma_b = 65$ $\mu$m for bottom lines; $\sigma_t = 90$ $\mu$m for top lines.

As was mentioned in the introduction, the $\sigma_t$ value for the top lines always turns out to be larger than $\sigma_b$.

All the above results confirm the quoted measurement precision. The coincidence of the shapes of the distributions of the results obtained by both methods is enough to state that both methods are close in precisions.

## CONCLUSION

Measurements performed by both methods indicate that MODULE No. 8 is within tolerance (0.6 mm from the nominal size).

Impressive coincidence of both laser and photo fully independent methods has been achieved by applying two corrections:

— turning of the laser method data by an angle $\theta_0 = 0.8 \cdot 10^{-4}$ rad with respect to the $Z$ axis;

— correction of the nominal MODULE width in the nominal MODULE top part (see item 3, size «$A$») chosen in the photo method; this correction is based on direct measurements of size «$A$».

So the results of measuring the «MODULE geometry» by both methods coincide with an accuracy of about $(\sigma_b + \sigma_t)/2 \approx 80$ $\mu$m.

All the above-said allows one to conclude that, as we understand:

It seems very important to use both methods (they are independent) for fulfilling such a complex technical task as the precision assembly of the barrel hadron calorimeter and a much more difficult task like final assembly of all ATLAS systems in the near future.

The joining of the JINR and CERN groups' efforts might lead to the rise of engineering culture of a new generation: high-precision metrology when precision assembling of large-scale massive objects.

**Acknowledgements.** The CERN team would like to express their gratitude to the JINR team for having initiated that study and incorporated the photogrammetry concepts and results.

Some other persons from the CERN team participated in the regular measurements of the tile MODULES: Katia Nummiaro, Dirk Mergelkuhl, Jean-Frédéric Fuchs, for the photogrammetric parts — measurements, analysis and report; Jean Noel Joux and André Froton, for the geometrical preparatory works.

The JINR team thanks INTAS for the financial support of the JINR team work with grant INTAS–CERN No. 288.

The JINR team thanks Yu. Lomakin for his great contribution at all stages of the MODULE assembly at JINR. We are grateful to V. Romanov, M. Nazarenko, S. Tokar and A. Shchelchkov for their help at various stages on assembly technology development, accumulated data pasportization, high precision measurements tooling delivery, solving of a numerous custom and transport problems.

REFERENCES

1. *Airapetian A. et al.* CERN/LHCC/96-42. 1996.

2. *Alikov B. A. et al.* Metrological Inspection of MODULES of Hardon Calorimeter for ATLAS Detector. Tile Cal. Inter. Nat. Note No. 79. 1997.

3. *Batusov V. et al.* // Part. Nucl., Lett. 2001. No. 2[105]. P. 33.

Received on May 17, 2002.

## Appendix 1
## LASER MEASUREMENT SYSTEM (LMS)

Parts of the measurement equipment we use, are precision instruments industrially produced: CALIPERS ($\pm 20$ $\mu$m precision) and MINILEVEL ($\pm 10^{-5}$ rad/m precision).

The special laser measurement system (Fig. 13), we have designed and constructed, has a potential of precision of $\pm 50$ $\mu$m when operated over a distance of typically 6 m in length. The gaining factor has been in the combination of this precision to an operation and manipulation simplicity for this device.

The LMS has been designed and constructed for the control of the surface geometry. The LMS (Fig. 14) consists of a laser and photo-detector (PhD) built up by four independent parts; both the laser and the PhD are fixed on special and high-precision adjustment units.

The LMS measurement principle was proposed by the authors for an earlier [2] application. Its principle is based on the measurements of the distance $H(i)$ between the surface under control ($LL'$) and the axis of the laser beam directed in a quasi-parallel way to that surface (Fig. 14). By positioning the PhD detector at different positions $A(i)$, the associated values of $H(i)$ are determined by adjusting (using a system of a microscrews) the centre of the photo-detector relative to the laser beam. The full surface geometry is determined by a series of such measurements (Fig. 15).

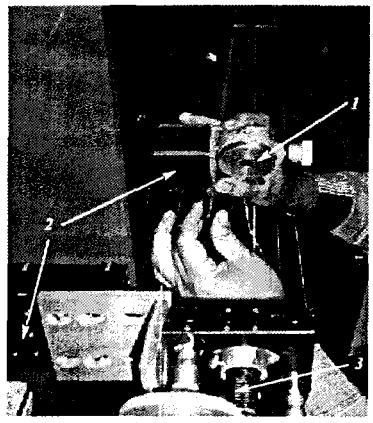


Fig. 13. Measurement system: *1* — quadrant photodiod; *2* — magnetic bases; *3* — laser

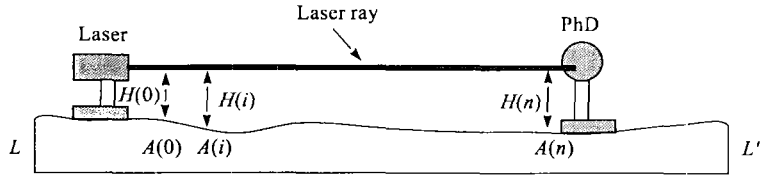


Fig. 14. LMS measuring principle

The measurement precision is limited by the precision of the adjustment system and by the air convective fluxes, which can be noticeably improved by positioning the laser beam inside a special telescopic dielectric tube.

Multiple measurements done with our LMS have shown that the standard deviation value for individual $H(n)$ measurements on a 6 m long calibrated base is 30 $\mu$m. By adding to this the intrinsic precision, the precision of the positioning of the LMS system on the surface to be measured (specific submodules surface), the resulting measurement precision for the entire area (1.9 × 5.6 m) of the MODULE side surface is within $\pm 50$ $\mu$m.

Fig. 15. LMS during assembly and quality control

## Appendix 2
## DUBNA LASER MEASUREMENT SYSTEM MAIN COMPONENTS

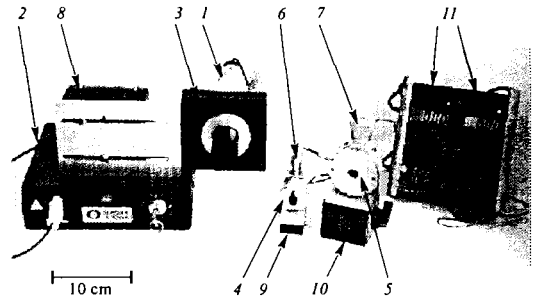


Fig. 16. Dubna Laser Measurement System main components: *1* — laser; *2* — power module; *3* — adjustment module; *4, 5* — quadrant photodiode devices (*4* — type I; *5* — type II); *6, 7* — positioning module (*6* — type I; *7* — type II); *8, 9, 10* — magnetic base (*8* — type I; *9* — type II; *10* — type III); *11* — multimeters

## Appendix 3
## GEOMETRICAL AND PHOTOGRAMMETRIC OPERATIONS FOR THE MODULE No. 8

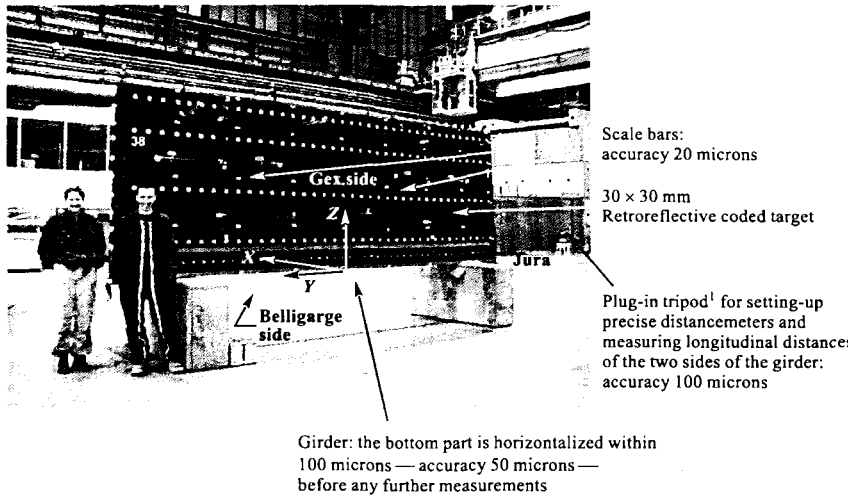


Fig. 17

The MODULE No. 8 was measured at CERN in January 2000, first by theodolite (see the results on http://edms.cern.ch/document/309991/1) then by photogrammetry (see the results and the comparisons on http://edms.cern.ch/document/309987/1).

[1]This tripod was also used for the first measurement by theodolite: specific targets were hold in the gap between two successive plates so that the target was referred to the average external surface of four successive plates apart the gap.

## CERN MAIN PHOTOGRAMMETRIC EQUIPMENT

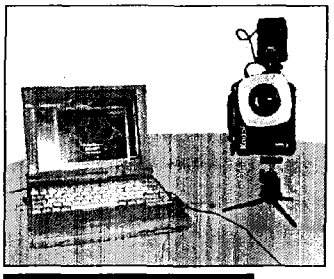

— DCS 460 — sensor CCD ⇒ 6 millions pixels/pixels = 9 m
— 18, 20, 24 mm lenses
— Rollei DPA/CDW software package

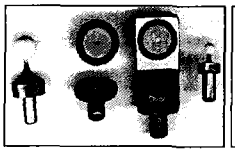

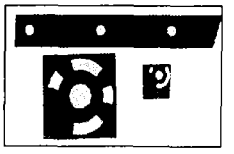

*Usual retro-reflective targes* *Strips and coded labels*

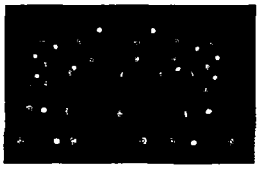

f/16, f/22 ⇒ under-exposed photos
⇒ necessity of reflective targets and annular flash
⇒ good contrast
⇒ image processing precision = 1/30 pixel = 0.3–0.4 m

Fig. 18

## Appendix 4
## WHAT IS DIGITAL PHOTOGRAMMETRY?
## ...3-D COORDINATE MEASURING TECHNIQUE

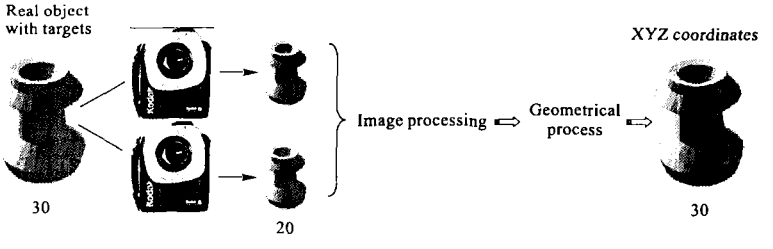


*At least two images from two different locations. One cannot measure the object itself... but its image.*

Geomentical process:

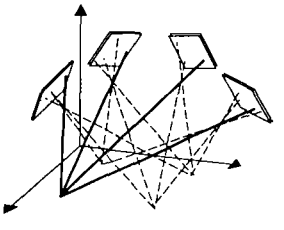

**1. Multi-image orientation**

**Resection** = process that enables one to know the camera position and aiming angles
**Triangulation** = intersecting lines in space, computes the location of a point in all three dimensios

⇒ Approximate positions and approximate coordinates = 3 translations + 3 rotations

Fig. 19

**2. Perspective rays adjustment:**

interior (image system — self calibration → systematic error camera)
and exterior orientations (object system) of the camera adjusted together

Scaling photogrammetry:

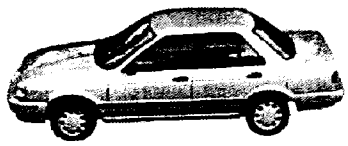

Need to use calibrated scale bars and/or known distances on the object

Forms! Dimensions?

Forms! Dimensions!

Least squares ⇒ 3D object coordinates ⇒ statistical analysis ⇒ error budget...
geometrical modeling... as built/reverse engineering...

Fig. 20

## Appendix 5
## DEVIATION OF THE MEASURED POINTS FROM THE SURFACE OF THE NOMINAL MODULE

The results of the LASER (Bot R, Top R, Top L, Bot L) and photogrammetry (Bel 1, Bel 4, Gex 4, Gex 1) methods are presented in the form of the table of deviation of

*Table* 1

| No. of submodule | Right side | | | | Left side | | | |
|---|---|---|---|---|---|---|---|---|
| | Distance for bottom line | | Distance for top line | | Distance for top line | | Distance for bottom line | |
| | Bel 1 | Bot R | Bel 4 | Top R | Gex 4 | Top L | Gex 1 | Bot L |
| 1 | −0.12 | −0.18 | 0.04 | −0.28 | 0.22 | −0.23 | 0.30 | −0.18 |
| 2 | −0.10 | −0.14 | 0.11 | −0.14 | 0.13 | −0.35 | 0.23 | −0.21 |
| 3 | −0.12 | −0.17 | 0.17 | 0.06 | −0.10 | −0.44 | 0.28 | −0.22 |
| 4 | −0.11 | −0.21 | 0.14 | −0.13 | −0.02 | −0.33 | 0.19 | −0.17 |
| 5 | −0.16 | −0.31 | 0.08 | −0.34 | 0.00 | −0.22 | 0.18 | −0.12 |
| 6 | −0.15 | −0.22 | 0.19 | −0.22 | −0.11 | −0.24 | 0.10 | −0.19 |
| 7 | −0.05 | −0.29 | 0.21 | −0.08 | 0.21 | −0.44 | 0.06 | −0.28 |
| 8 | −0.06 | −0.18 | 0.14 | −0.11 | −0.10 | −0.12 | −0.07 | −0.25 |
| 9 | −0.03 | −0.18 | 0.22 | −0.16 | 0.12 | −0.22 | 0.04 | −0.19 |
| 10 | 0.04 | −0.23 | 0.29 | −0.06 | −0.27 | −0.26 | −0.04 | −0.18 |
| 11 | 0.02 | −0.18 | 0.07 | −0.32 | −0.16 | −0.28 | −0.14 | −0.29 |
| 12 | 0.03 | −0.25 | 0.12 | −0.41 | 0.06 | −0.05 | −0.04 | −0.21 |
| 13 | 0.12 | −0.21 | 0.08 | −0.40 | 0.00 | −0.01 | −0.11 | −0.25 |
| 14 | 0.05 | −0.21 | −0.06 | −0.54 | 0.06 | 0.18 | −0.04 | −0.19 |
| 15 | 0.24 | −0.21 | −0.05 | −0.49 | 0.18 | 0.14 | −0.03 | −0.20 |
| 16 | 0.29 | −0.20 | −0.16 | −0.70 | 0.33 | 0.26 | −0.06 | −0.24 |
| 17 | 0.23 | −0.18 | −0.09 | −0.58 | 0.38 | 0.52 | −0.06 | −0.17 |
| 18 | 0.24 | −0.24 | −0.25 | −0.86 | 0.33 | 0.35 | −0.14 | −0.22 |
| 19 | 0.24 | −0.21 | −0.29 | −0.96 | 0.38 | 0.48 | −0.16 | −0.21 |

the measured points from the surface of the nominal MODULE for each submodule. The left (right) side of the MODULE is the side on the left (right) of the observer looking from the SM1 along the MODULE

## Appendix 6
## RESULTS OF COMPARISON

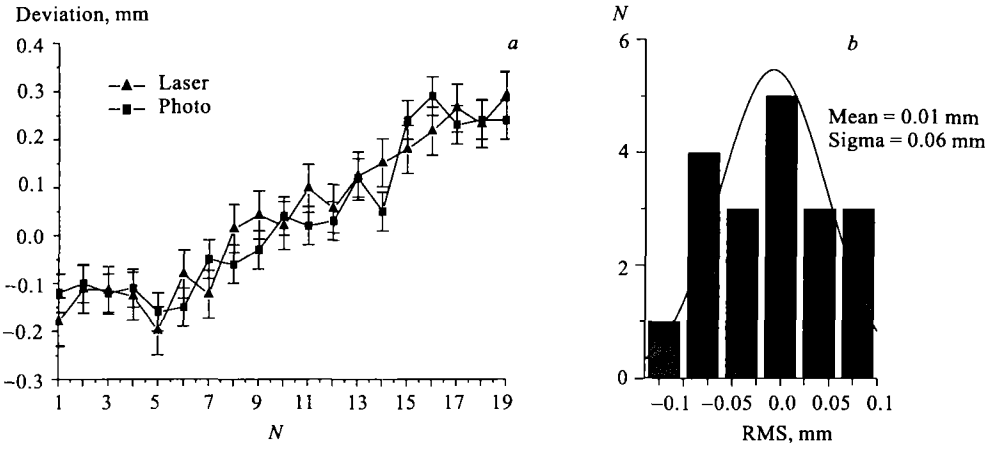


Fig. 21. Line Bel 1 measurements data by the photogrammetric and laser bottom-right methods after correction (turn by $0.8 \cdot 10^{-4}$ rad)

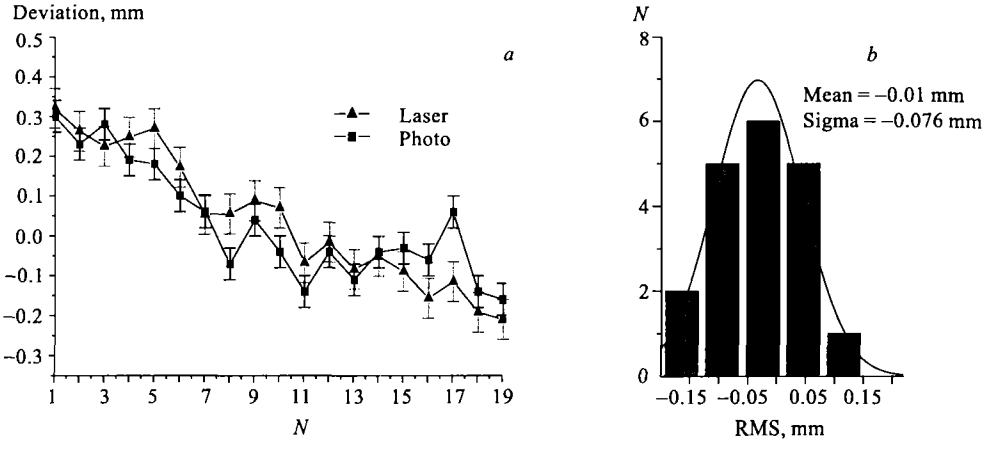


Fig. 22. Line Gex 1 measurements data by the photogrammetric and laser bottom-left methods after correction (turn by $0.8 \cdot 10^{-4}$ rad)

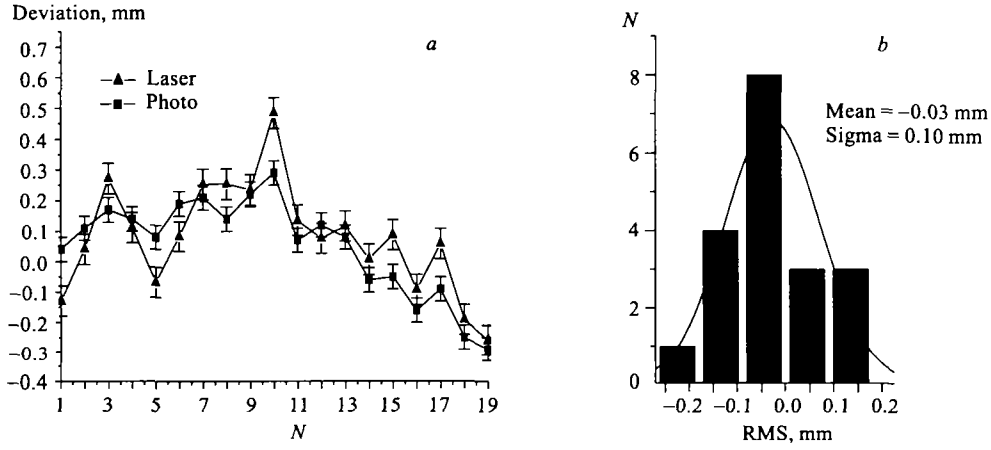


Fig. 23. Line Bel 4 measurements data by the photogrammetric and laser top-right methods after correction (turn by $0.8 \cdot 10^{-4}$ rad)

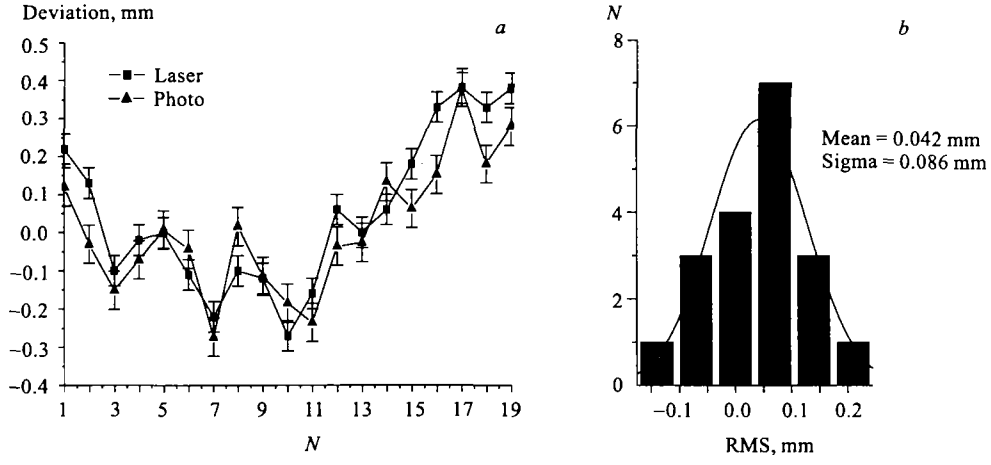


Fig. 24. Line Gex 4 measurements data by the photogrammetric and laser top-left methods after correction (turn by $0.8 \cdot 10^{-4}$ rad)

Письма в ЭЧАЯ. 2002. №4[113] Particles and Nuclei, Letters. 2002. No.4[113]

УДК 539.1.07

# КАЛИБРОВКА ПУЧКОВОГО ПОЛЯРИМЕТРА НА СИНХРОФАЗОТРОНЕ ОИЯИ

*Л. С. Ажгирей* [а], *А. А. Жданов* [б], *В. Н. Жмыров* [а], *В. П. Ладыгин* [а], *Ф. Легар* [в], *А. Н. Прокофьев* [б], *Г. Д. Столетов* [а]

[а] Объединенный институт ядерных исследований, Дубна

[б] Петербургский институт ядерной физики РАН, Гатчина, Россия

[в] DAPNIA, CEA/Saclay, Gif-sur-Yvette Cedex, France

Описаны результаты калибровки поляриметра, предназначенного для измерения векторной компоненты поляризации пучка дейтронов на синхрофазотроне ОИЯИ. Приводятся данные об анализирующей способности упругого *pp*-рассеяния на угол 14° в л.с. в области импульсов протонов от 1,18 до 3,46 ГэВ/*c* и эффективной анализирующей способности рассеяния протонов на полиэтиленовой мишени на тот же угол при импульсах протонов между 1,4 и 2,8 ГэВ/*c*. Полученные результаты использовались для измерения поляризации пучка дейтронов в опытах по измерению разности полных сечений *np*-рассеяния продольно-поляризованных нейтрона и протона с различными ориентациями спинов.

The results of calibration of the polarimeter for the measurement of the vector component of the polarization of the deuteron beam at the JINR Synchrophasotron are presented. The data on the analyzing power of the elastic *pp* scattering at an angle of 14° (lab. syst.) in the range of proton momenta from 1.18 to 3.46 GeV/*c* and on the effective analyzing power of the proton scattering on polyethylene target at proton momenta between 1.48 and 2.79 GeV/*c* are given. The data obtained were used to measure the deuteron beam polarization during experiment on the measurement of the total cross section difference $\Delta\sigma_L$ in *np* transmission.

## ВВЕДЕНИЕ

Исследование поляризационных явлений в ядерных реакциях на синхрофазотроне ОИЯИ [1–6] потребовало создания поляриметра для мониторирования векторной компоненты поляризации пучка дейтронов, поставляемых ионным источником [7]. С этой целью на канале медленного вывода синхрофазотрона был сооружен поляриметр, измеряющий асимметрию рассеяния протонов на полиэтиленовой мишени [8].

Поляриметр состоит из мишени и направленных на нее четырех телескопов, каждый из которых содержит по два сцинтилляционных счетчика. Обе пары телескопов устанавливаются в горизонтальной плоскости (вектор спина дейтронов ориентирован вертикально) под углами относительно падающего пучка, соответствующими кинематике упругого *pp*-рассеяния для рассеянной частицы и частицы отдачи. Таким образом, четырехкратные совпадения сигналов со сцинтилляционных счетчиков позволяют выделять события, соответствующие упругому (и квазиупругому) *pp*-рассеяниям, и одновременно регистрировать случаи рассеяния направо и налево, определяющие асимметрию рассеяния. Более детальное описание поляриметра приводится в [8].

Основанием для создания этого поляриметра послужило то, что, с одной стороны, поляризация протонов (и нейтронов), вылетающих вперед в результате развала дейтронов на мишени, равна поляризации дейтронного пучка; с другой стороны, известно, что анализирующие способности упругого и квазиупругого $pp$-рассеяний в широкой области энергий одинаковы [9].

Помимо относительного мониторирования поляризации пучка, поляриметр может использоваться и для измерения абсолютной величины поляризации; для этого, однако, он должен быть прокалиброван. Проблеме калибровки пучкового поляриметра и посвящено настоящее сообщение.

## КАЛИБРОВКА ПОЛЯРИМЕТРА

Предварительная калибровка пучкового поляриметра (т.е. определение величины $A(CH_2)$ — анализирующей способности для рассеяния на полиэтиленовой мишени) была выполнена [10] по результатам измерения векторной поляризации пучка дейтронов в экспериментах по определению разности полных сечений $\Delta\sigma_L$ $np$-рассеяния в сеансах 1995 г. [1] и 1997 г. [4]. Абсолютная величина векторной поляризации пучка была получена в сеансе 1997 г. по результатам измерения асимметрии для разности $CH_2-C$ и известной анализирующей способности $pp$-рассеяния протонов с импульсом 1,48 ГэВ/$c$ на угол 14°. Отсюда была определена эффективная анализирующая способность для рассеяния на $CH_2$. Далее, привязываясь к этой величине, на основании измерений асимметрии на $CH_2$ в сеансах 1995 и 1997 гг. нашли импульсную зависимость $A(CH_2)$ для рассеяния протонов на угол 14° в интервале от 1,48 до 3,0 ГэВ/$c$. Таким образом, абсолютные значения $A(CH_2)$ были получены, по существу, по измерениям при одном импульсе дейтронов, 2,96 ГэВ/$c$.

В 2001 г., в сеансе измерений разности $\Delta\sigma_L$ представилась возможность провести более детальную калибровку пучкового поляриметра для рассеяния на $CH_2$ на угол 14°. Измерения асимметрии $pp$-рассеяния по разности $CH_2-C$ были выполнены при кинетических энергиях протонов 1,4, 1,7, 1,9 и 2,0 ГэВ. Анализирующая способность упругого $pp$-рассеяния в интересующей нас области энергий протонов была определена по мировым данным о поляризации, возникающей при рассеянии неполяризованного пучка на неполяризованной мишени, и по данным об анализирующей способности упругого $pp$-рассеяния, полученным на поляризованной мишени. С этой целью использовались результаты измерений угловых зависимостей поляризации в упругом $pp$-рассеянии в интервале углов рассеяния $\Theta^*$ в с.ц.м., включающих угол 14° в л.с., из работ [11–33], приведенные в базе данных [34]; данные об анализирующей способности $A_{00n0}(pp)$ в окрестности 2,2 ГэВ/$c$ [35]; результаты недавних измерений функции возбуждения анализирующей способности $p$p-рассеяния на ускорителе COSY [36].

Угловые зависимости аппроксимировались выражением

$$P(\Theta^*) = \sum_{i=1}^{n} a_i (\Theta^*)^i, \tag{1}$$

где $a_i$ — подгоняемые параметры; угловые зависимости из базы данных [34], измеренные при импульсах $\leq 1{,}7$ ГэВ/$c$, фитировались до значения $n = 2$, остальные данные — до

значения $n = 4$. Из угловых зависимостей $A_{00n0}(pp)$, приведенных в [36], интересующие нас значения под углом 14° в л. с. при импульсах выше 1,910 ГэВ/$c$ были найдены путем интерполяции, а ниже этого значения — путем экстраполяции. Что касается работ [31] и [35], в которых измерения проводились под углом 13,9° в л. с., предполагалось, что эти данные можно отнести к углу 14°, допустив лишь незначительную ошибку. Параметры, вычисленные в результате аппроксимации всех упомянутых данных выражением (1), позволили найти значения поляризации $P_{pp}(14°)$.

Найденные значения, численно равные анализирующей способности $A_{00n0}$ упругого $pp$-рассеяния на угол 14°, оказалось возможным аппроксимировать плавной зависимостью от импульса протонов в интервале от 1,185 до 3,464 ГэВ/$c$:

$$A(p) = (0{,}6658 \pm 0{,}0066) - (0{,}1236 \pm 0{,}0055)p + (0{,}0077 \pm 0{,}0012)p^2 \qquad (2)$$

при отношении $\chi^2/ndf = 270{,}7/142$ для 145 значений поляризации. Линейная аппроксимация дает результат

$$A(p) = (0{,}7056 \pm 0{,}0041) - (0{,}1605 \pm 0{,}0015)p \qquad (3)$$

при отношении $\chi^2/ndf = 278{,}7/143$. Экспериментальные данные и результат аппроксимации показаны на рис. 1, *а*. На рис. 1, *б* показаны данные и аппроксимирующая зависимость в интервале импульсов от 2,7 до 3,5 ГэВ/$c$; эта область дает наибольший вклад в величину $\chi^2$.

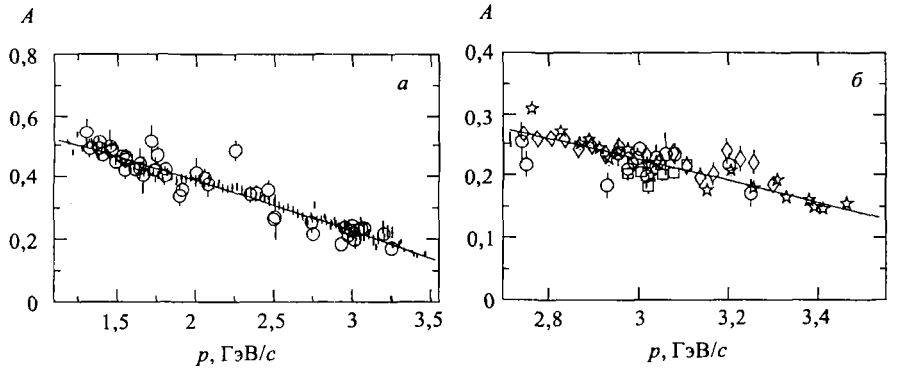


Рис. 1. Зависимость анализирующей способности упругого $pp$-рассеяния на угол 14° в л. с. от импульса протонов. Экспериментальные данные: *а*) светлые кружки — [34]; темные точки — [31, 35, 36]; *б*) светлые кружки — [34]; звездочки — [31]; квадраты — [35]; ромбы — [36]

Найденная зависимость $A(p)$ для $pp$-рассеяния и результаты измерения асимметрии для разности $CH_2 - C$ позволили определить эффективную анализирующую способность для рассеяния на мишени $CH_2$ при кинетических энергиях протонов 1,4, 1,7, 1,9 и 2,0 ГэВ.

Кроме этого, были заново проанализированы результаты измерения асимметрии для разности $CH_2 - C$ в сеансе 1997 г. при рассеянии протонов с импульсом 1,48 ГэВ/$c$ на угол 14°. Уточненные значения составили: асимметрия в $pp$-рассеянии $\epsilon(pp) = 0{,}273 \pm 0{,}008$;

*Таблица* 1. **Эффективные анализирующие способности $A(CH_2)$ для рассеяния протонов на угол 14°, измеренные пучковым поляриметром**

| $p_d$, ГэВ/$c$ | $T_p$, ГэВ | $\epsilon(CH_2)$ | $A(CH_2)$ | Работа |
|---|---|---|---|---|
| 2,96 | 0,81 | 0,231 ± 0,005 | 0,395 ± 0,008 | Перенорм. [10] |
| 4,28 | 1,40 | 0,156 ± 0,005 | 0,301 ± 0,012 | Настоящая работа |
| 4,28 | 1,40 | 0,151 ± 0,008 | 0,275 ± 0,015 | Настоящая работа |
| 4,72 | 1,60 | 0,168 ± 0,003 | 0,286 ± 0,009 | Перенорм. [10] |
| 4,93 | 1,70 | 0,121 ± 0,004 | 0,225 ± 0,009 | Настоящая работа |
| 5,14 | 1,80 | 0,144 ± 0,004 | 0,246 ± 0,009 | Перенорм. [10] |
| 5,36 | 1,90 | 0,113 ± 0,004 | 0,206 ± 0,013 | Настоящая работа |
| 5,57 | 2,00 | 0,103 ± 0,002 | 0,187 ± 0,005 | Настоящая работа |
| 6,00 | 2,20 | 0,086 ± 0,003 | 0,147 ± 0,007 | Перенорм. [10] |

определенная из соотношения (2) анализирующая способность $pp$-рассеяния 0,466; поляризация пучка $P = 0{,}586 \pm 0{,}017$ (что согласуется с результатами работы [10]); асимметрия в рассеянии на $CH_2$ $\epsilon(CH_2) = 0{,}2314 \pm 0{,}0054$; эффективная анализирующая способность при 1,48 ГэВ/$c$ $A(CH_2) = 0{,}395 \pm 0{,}008$.

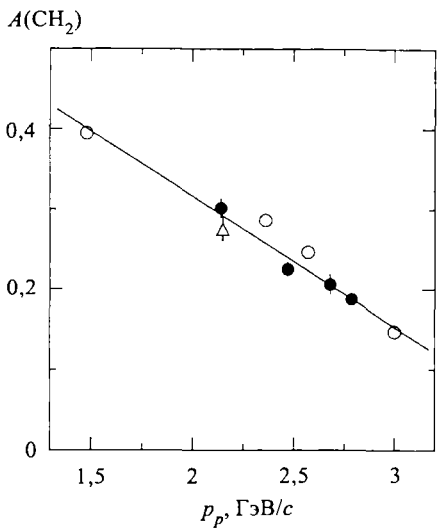


Рис. 2. Зависимость эффективной анализирующей способности $A(CH_2)$ для рассеяния на угол 14° в л.с. от импульса протонов. Светлыми кружками показаны перенормированные данные работы [10], темными кружками и светлым треугольником — данные настоящей работы

Перенормировка значений $A(CH_2)$ для $T_p$, равных 1,6, 1,8 и 2,2 ГэВ, требует отдельного пояснения. Дело в том, что в процессе обработки данных сеанса 1997 г. было замечено уменьшение величины поляризации пучка в ходе измерения параметра $\Delta\sigma_L$, и это доказывает необходимость непрерывного мониторирования поляризации. Полученные в процессе мониторирования значения асимметрии в рассеянии на $CH_2$ затем были экстраполированы к «нулевому» моменту времени в предположении, что поляризация в ходе всего сеанса уменьшалась линейно; именно эти экстраполированные значения и приведены в табл. 1 и на рис. 1 работы [10]. Сейчас, однако, ясно, что предположение о линейном дрейфе величины поляризации в течение всего сеанса достаточно произвольно, этот дрейф характерен только для периода мониторирования, поэтому вместо экстраполированных значений следует использовать измеренные значения асимметрии, указав возможные систематические ошибки. Все данные по эффективной анализирующей способности для рассеяния на $CH_2$, включая перенормированные данные работы [10] и данные, полученные в сеансе 2001 г., приведены в табл. 1 и показаны на рис. 2 в зависимости от импульса протонов.

Данные об эффективной анализирующей способности для рассеяния на $CH_2$ можно аппроксимировать зависимостью

$$A_{CH_2}(p_p) = (0{,}642 \pm 0{,}016) - (0{,}163 \pm 0{,}006)p_p. \quad (4)$$

Отметим, что в табл. 1 и на рис. 2 указаны чисто статистические ошибки. Разброс значений на рис. 2 относительно аппроксимирующей прямой позволяет оценить возможную систематическую ошибку этих данных, которая составляет около 8 %, как это и указывалось в работе [10]. Следует также отметить, что телесный угол поляриметра в сеансах 2001 г. был несколько меньше, чем в сеансах 1995 и 1997 гг., что не сказалось на полученных результатах.

Другой способ калибровки пучкового поляриметра (или же определения поляризации пучка по известной анализирующей способности) основан на измерении зависимости числа совпадений сигналов от счетчиков, регистрирующих рассеянную частицу и частицу отдачи, от угла, под которым расположен сопряженный телескоп.

Такие измерения были проведены в июне 2001 г. на пучке векторно-поляризованных дейтронов с импульсом 4,28 ГэВ/*c*. Угол рассеяния был выбран равным 14°, при этом частица отдачи в упругом *pp*-рассеянии вылетает под углом 66,5°. Более подробные измерения, к сожалению, не могли быть выполнены в ходе этого эксперимента, однако полученные результаты, показанные на рис. 3, в достаточной мере иллюстрируют описываемый способ калибровки.

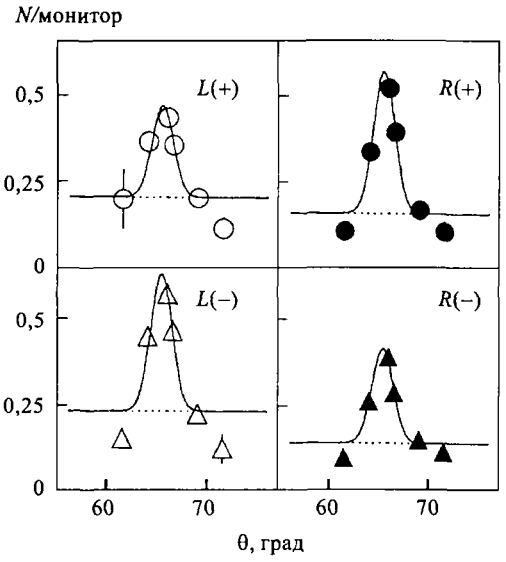


Рис. 3. Зависимости отношений числа четырехкратных совпадений к числу отсчетов монитора от углов, под которыми расположены сопряженные телескопы поляриметра, для разных ориентаций спина дейтронов относительно горизонтальной плоскости. Светлые и темные кружки (треугольники) соответствуют рассеянию налево и направо частиц со спином, направленным вверх (вниз)

Измеренные угловые зависимости аппроксимировались выражением

$$N/\text{монитор} = N_0 \exp\left(-((\Theta - \Theta_0)/\sigma_0)^2/2\right) + A(1 + B\Theta). \quad (5)$$

Здесь первый и второй члены представляют, соответственно, вклады от рассеяния на ядрах водорода и нуклонах углерода, составляющих мишень $CH_2$. По 24 значениям отношений $N$/монитор были определены 11 параметров (параметры $\Theta_0$, $\sigma_0$ и $B$ для всех четырех распределений были одинаковы). Поскольку площади под пиками на рис. 3 пропорциональны произведению $N_0\sigma_0$, асимметрия рассеяния на водороде представляется в виде

$$\epsilon_{pp} = \frac{L^+R^- - L^-R^+}{(L^+ + L^-)(R^+ + R^-)}, \quad (6)$$

где $L^+, L^-, R^+$ и $R^-$ суть значения параметров $N_0$, причем $L$ и $R$ соответствуют рассеяниям налево и направо, а индексы «+» и «–» — знакам поляризации.

Полученное в этих измерениях значение $\epsilon_{pp} = 0{,}2011 \pm 0{,}0082$ приводит к поляризации пучка, равной $0{,}550 \pm 0{,}022$. Асимметрия рассеяния на $CH_2$ оказалась равной $0{,}1512 \pm 0{,}0085$, откуда анализирующая способность $A(CH_2) = 0{,}275 \pm 0{,}015$. Это значение приведено в табл. 1 и в виде светлого треугольника показано на рис. 2. Видно, что оно согласуется со значением, полученным при этом же импульсе протонов другим способом. Точность результатов можно было бы и повысить, если бы удалось выполнить измерения на крыльях угловых зависимостей.

## ЗАКЛЮЧЕНИЕ

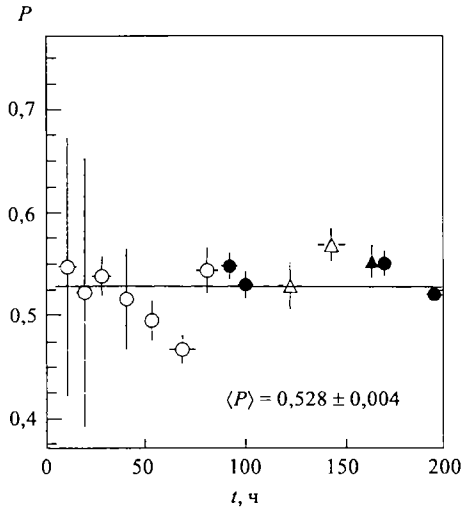


Рис. 4. Результаты измерения векторной поляризации пучка дейтронов в сеансе 2001 г. при разных импульсах дейтронов: светлые кружки — 4,28 ГэВ/*c*; темные кружки — 4,93 ГэВ/*c*; светлые треугольники — 5,36 ГэВ/*c*; темные треугольники — 5,57 ГэВ/*c*

В заключение приведем результаты измерения поляризации векторно-поляризованного пучка дейтронов в сеансе 2001 г., во время измерений разности полных сечений $np$-рассеяния $\Delta\sigma_L$ на продольно-поляризованных пучке и мишени, полученные с помощью пучкового поляриметра. Измерения проводились для начальных импульсов дейтронов 4,18; 4,93; 5,36 и 5,57 ГэВ/*c*. Угол рассеяния в поляриметре был выбран равным 14°, измерения проводились по разности от мишеней $CH_2$ и C, использовались значения анализирующей способности $pp$-рассеяния в соответствии с соотношением (1). Результаты измерений, соответствующие разным значениям импульса протонов, в хронологическом порядке показаны на рис. 4.

Поскольку в течение большей части сеанса использовался пучок с двумя модами поляризации, на рис. 4 приведены усредненные по модам поляризации значения. Среднее значение поляризации в течение указанного времени измерений составило $\langle P \rangle = 0{,}528 \pm 0{,}004$.

Измерения с тремя модами поляризации пучка дают возможность определить значения поляризации, отвечающие различным ориентациям спина дейтронов относительно горизонтальной плоскости; такие измерения также проводились несколько раз в ходе сеанса. Условия измерений и полученные результаты приведены в табл. 2.

Отметим, что приведенные в табл. 2 данные, полученные 11 и 13.10.2001, в результате усреднения приводят к значениям, показанным в виде первой и пятой точек на рис. 4. Измерения 19.10.2001 г. проводились с помощью поляриметра, расположенного в фокусе F3 канала медленного вывода ВП-1.

*Таблица* 2. **Поляризация пучка дейтронов с противоположными ориентациями спина**

| Время измерений | $p_d$, ГэВ/$c$ | Угол рассеяния | Мишень | $A$ | $P(+)$ | $P(-)$ |
|---|---|---|---|---|---|---|
| 06.10.2001 | 7,6 | 8° | $CH_2$ | 0,212 | $0{,}533 \pm 0{,}073$ | $-0{,}628 \pm 0{,}072$ |
| 11.10.2001 | 4,28 | 14° | $CH_2-C$ | 0,366 | $0{,}568 \pm 0{,}037$ | $-0{,}612 \pm 0{,}037$ |
| | | | | | $0{,}544 \pm 0{,}032$ | $-0{,}601 \pm 0{,}041$ |
| 13.10.2001 | 4,28 | 14° | $CH_2-C$ | 0,366 | $0{,}433 \pm 0{,}051$ | $-0{,}544 \pm 0{,}050$ |
| | | | | | $0{,}448 \pm 0{,}035$ | $-0{,}518 \pm 0{,}032$ |
| 19.10.2001 | 3,5 | 14° | $CH_2$ | 0,357 | $0{,}314 \pm 0{,}020$ | $-0{,}441 \pm 0{,}020$ |
| | | | | | $0{,}305 \pm 0{,}014$ | $-0{,}490 \pm 0{,}014$ |
| | | | | | $0{,}322 \pm 0{,}048$ | $-0{,}495 \pm 0{,}041$ |

Исследования были частично поддержаны Российским фондом фундаментальных исследований (грант №01-02-17299).

## СПИСОК ЛИТЕРАТУРЫ

1. *Adiasevich B. P. et al.* // Z. Phys. C. 1996. V. 71. P. 65.
2. *Afanasiev S. V. et al.* // Phys. Lett. B. 1998. V. 434. P. 21.
3. *Ажгирей Л. С. и др.* // ЯФ. 1999. Т. 62. С. 1796.
4. *Sharov V. I. et al.* // Eur. Phys. J. C. 2000. V. 13. P. 255.
5. *Ladygin V. P. et al.* // Eur. Phys. J. A. 2000. V. 8. P. 409.
6. *Ажгирей Л. С. и др.* // ЯФ. 2001. Т. 64. С. 2046.
7. *Anishchenko N. G. et al.* // Proc. of the 5th Intern. Symp. on High Energy Spin Physics, Brookhaven, 1982. AIP Conf. Proc. 1983. V. 95. P. 445.
8. *Ажгирей Л. С. и др.* // ПТЭ. 1997. Т. 1. С. 51; transl.: Instr. and Exp. Tech. 1997. V. 40. P. 43.
9. *Ball J. et al.* // Eur. Phys. J. C. 1999. V. 11. P. 51; references therein.
10. *Ажгирей Л. С. и др.* // Крат. сообщ. ОИЯИ. 1999. №3[95]. С. 20.
11. *Azhgirey L. S. et al.* // Sov. J. Nucl. Phys. 1966. V. 2. P. 636.
12. *Albrow M. G. et al.* // Nucl. Phys. B. 1970. V. 23. P. 445.
13. *Betz F. W. et al.* // Phys. Rev. 1966. V. 148. P. 1289.
14. *McNaughton M. W. et al.* // Phys. Rev. C. 1982. V. 23. P. 1128.
15. *Barlett M. L. et al.* // Phys. Rev. C. 1983. V. 27. P. 682.
16. *Cozzika G. et al.* // Phys. Rev. 1967. V. 164. P. 1672.

17. *Lehar F. et al.* // Nucl. Phys. B. 1987. V. 294. P. 1013.

18. *Perrot F. et al.* // Ibid. P. 1001.

19. *Borisov N. S. et al.* // JETP Lett. 1981. V. 34. P. 130.

20. *Homer R. J. et al.* // Nuovo Cim. 1962. V. 23. P. 690.

21. *Vovchenko V. G. et al.* // JETP Lett. 1979. V. 29. P. 87.

22. *Garçon M. et al.* // Phys. Lett. B. 1987. V. 183. P. 273.

23. *Marshak M. L. et al.* // Phys. Rev. C. 1987. V. 18. P. 331.

24. *Bell D. A. et al.* // Phys. Lett. B. 1980. V. 94. P. 310.

25. *Miller D. et al.* // Phys. Rev. D. 1977. V. 16. P. 2016.

26. *Diebold R. et al.* // Phys. Rev. Lett. 1975. V. 35. P. 632.

27. *Makdisi Y. et al.* // Phys. Rev. Lett. 1980. V. 45. P. 1529.

28. *Neal H. A. et al.* // Phys. Rev. 1967. V. 161. P. 1374.

29. *Grannis P. et al.* // Phys. Rev. 1966. V. 148. P. 1297.

30. *Parry J. H. et al.* // Phys. Rev. D. 1973. V. 8. P. 45.

31. *Allgower C. E. et al.* // Nucl. Phys. A. 1998. V. 637. P. 231.

32. *Bareyre P. et al.* // Nuovo Cim. 1961. V. 20. P. 1049.

33. *Arvieux J. et al.* // Z. für Physik C. 1997. V. 76. P. 465.

34. Access via http://nn-online.sci.kun.nl

35. *Ball J. et al.* // Eur. Phys. J. C. 1999. V. 10. P. 409.

36. *Altmeier M. et al.* // Phys. Rev. Lett. 2000. V. 85. P. 1819.

Получено 11 июня 2002 г.

Письма в ЭЧАЯ. 2002. №4[113] Particles and Nuclei, Letters. 2002. No.4[113]

УДК 539.126.4

# АНОМАЛЬНОЕ ПОВЕДЕНИЕ $A$-, $t$-ЗАВИСИМОСТЕЙ И ФАЗЫ ПАРЦИАЛЬНОЙ ВОЛНЫ КОГЕРЕНТНОГО ОБРАЗОВАНИЯ РАДИАЛЬНОГО РЕЗОНАНСА $\pi(1300)$[1]

*О. А. Займидорога*

Объединенный институт ядерных исследований, Дубна

Сравнение свойств когерентного образования резонанса a1(1260) и радиального состояния $\pi(1300)$, рождаемых в одном процессе, свидетельствует об аномальном поведении $A$-, $t$-*зависимостей и фазы парциальной волны радиального резонанса* $\pi(1300)$.

The coherent production of resonance state a1(1260) confronts with the coherent production of radial excited state $\pi(1300)$. Anomalous $A$-, $t$-dependence of production cross-section and behaviour of phase of partial wave of radial state $\pi(1300)$ have been observed.

Взаимодействие адронов высокой энергии с ядрами с определенной вероятностью ведет к образованию тяжелых резонансов в процессе когерентного взаимодействия падающей частицы, в то время как ядро остается целым и в основном состоянии. Если после взаимодействия ядро остается в основном состоянии, то процесс является когерентным, а амплитуда процесса есть сумма индивидуальных нуклонных амплитуд. Если состояние ядра не изменяется, то между адроном и ядром может происходить обменный процесс с квантовыми числами вакуума. Когерентный дифракционный процесс сохраняет дискретные квантовые числа: заряд, барионное число, странность, $C$-, $G$-четность. Сечение процесса имеет пик в переднем направлении. Это означает, что рожденная резонансная система имеет ту же самую спиральность, что и падающая частица. И так как средний спин ядра равен нулю, то это не вносит вклада в азимутальный угловой момент. Когерентное взаимодействие адронов усиливает рождение резонансов, образованных дифракционно, в соответствии с определенными правилами отбора. Так, сечение когерентного дифракционного образования резонансных состояний растет с атомным номером ядра, имея максимум сечения под углом, равным нулю градусов. Примером такого состояния является рождение на ядерных мишенях резонанса a1(1260).

В настоящей работе представлены экспериментальные данные образования резонансов в когерентном процессе и сделано сравнение свойств рождения радиального состояния $\pi(1300)$ и резонанса a1(1260), которые рождаются в одном процессе взаимодействия $\pi$-мезона с ядром. Когерентное образование многомезонных систем $\pi$-мезонами с энергией 40 ГэВ на спектрометре ОИЯИ, на ускорителе с энергией 70 ГэВ в Серпухове исследовалось в сотрудничестве с институтами физики Милана, Болоньи и Европейским

[1]Работа была доложена на Еврофизической конференции по физике высоких энергий, Тампере, Финляндия, 1999 г.

центром ядерных исследований [1]. Мишени из Be, C, Si, Ti, Cu, Ag, Ta и Pb были использованы для изучения процесса

$$\pi + A \to \pi^+, \pi^-, \pi^- + A.$$

Полное число событий, удовлетворяющих критериям когерентного отбора, составило 153359 событий для всех масс. Выполненный парциально-волновой анализ этих событий позволил определить интенсивность и относительную фазу каждого состояния по спиночетности $3\pi$-системы [3]. Данный анализ был проведен для следующих критериев отбора:

а) для когерентного набора, содержащего события с $t' < t'^*$, где $t'^*$ — 4-мерный момент передачи импульса — соответствовал первому дифракционному минимуму $t' = t - t_{\min}$;

б) для каждого ядра отдельно с целью получения сведений об $A$-зависимости парциальных волн;

в) для различных областей по 4-мерной передаче для групп ядер в массовом интервале $3\pi$-системы 0,9–1,2 и 1,2–1,5 ГэВ/$c^2$.

Вклад некогерентных процессов под когерентным пиком составляет менее 8 %, а амплитуд с переворотом спина — менее 1 % [2], поэтому относительная фаза когерентных волн может быть измерена надежно.

Исследование резонансных свойств $1^+S$-состояния a1(1260) и $0^-S$-состояния $\pi(1300)$ было основано на данных парциально-волнового анализа когерентного набора, а также $A$- и $t$-зависимостей. $t'$-зависимости $1^+$- и $0^-$-состояний для областей масс 0,9–1,2 и 1,2–1,5 ГэВ показаны на рис. 1, *а, б*. Резонанс a1(1260) (волна $1^+$) демонстрирует максимальное сечение рождения при $t' = 0$ и $t'$-зависимость $\exp(-at')$, в то время как когерентно-рожденное радиальное состояние $\pi(1300)$ (волна $0^-$) имеет другое поведение

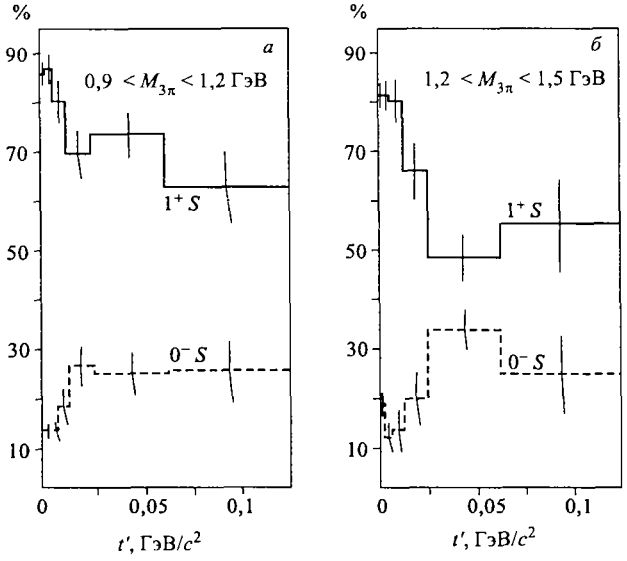


Рис. 1

и сечение образования этого состояния можно аппроксимировать функцией $t' \exp(-at')$. На рис. 2 представлена $A$-зависимость обеих волн: $1^+S$ — a1(1260) и $0^-S$ — $\pi(1300)$. Выход $1^+S$-состояния растет с атомным номером, в то время как выход $0^-S$-состояния не растет с атомным номером и стремится к уменьшению. Поведение относительной фазы $\delta$ $(1^+S - 0^-P)$ в зависимости от атомного номера приведено на рис. 3, *а* и свидетельствует об усилении дифракционного образования резонанса. На рис. 3, *б* $A$-зависимость $0^-S$-состояния демонстрирует тот факт, что разность фаз волн $0^-S$ и $0^-P$ не меняется с атомным номером. В противоположность поведению волны $1^+S$ это состояние не проявляет какой-либо $A$-зависимости относительной фазы волн $(0^-S - 0^-P)$.

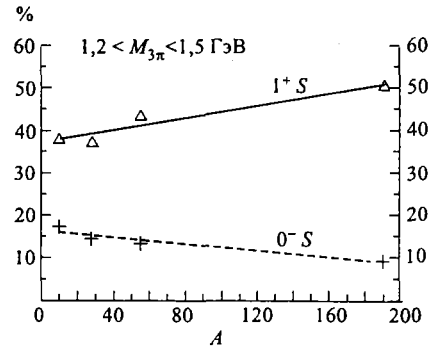


Рис. 2

Таким образом, увеличение выхода a1(1260) с ростом атомного номера ядра, рост фазы a1-резонанса наряду с уменьшением выхода состояния $\pi(1300)$ в зависимости от атомного номера ядра мишени и его специфическая $t'$-зависимость, по-видимому, указывают на то, что в процесс дифракционного рождения a1-резонанса на ядрах включается дополнительный механизм. Этот механизм может быть двухэтапным, так как в дифракционном рассеянии рожденная система, прежде чем достигнуть конечного состояния в течение переходного времени, может существовать в другом состоянии, например $\pi^- \rightarrow \pi(1300)^- \rightarrow$a1(1260). Пространственно-временная картина этого процесса обсуждалась в работе [4] и, по-видимому, адекватна наблюдаемому поведению $A$- и $t'$-зависимостей состояний a1(1260) и $\pi(1300)$.

Автор выражает благодарность членам коллаборации за возможность использования результатов исследований.

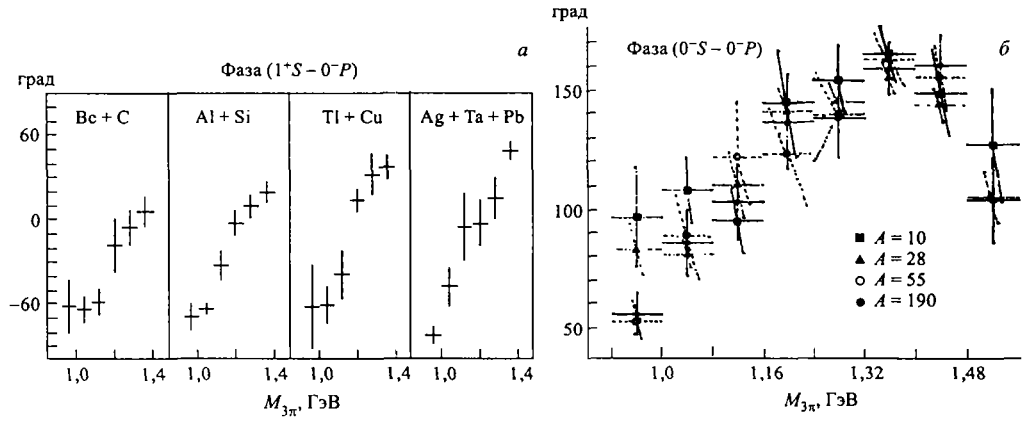


Рис. 3

## СПИСОК ЛИТЕРАТУРЫ

1. *Анджеяк Р. и др.* Препринт ОИЯИ 13-3588. Дубна, 1967.

2. *Bellini G., di Corato M., Frabetty P. L. et al.* Evidence of New $0^-S$ Resonances in $\pi^+\pi^-\pi^-$ System // Phys. Rev. Lett. 1982. V. 48. P. 1697.

3. *Займидорога О. А.* Радиальные возбуждения систем из легких кварков // ЭЧАЯ. 1999. Т. 30, вып. 1. С. 5.

4. *Fäldt G., Osland P.* Helicity-flip in Particle Production on Nuclei // Nucl. Phys. B. 1977. V. 126. P. 221.

Получено 25 сентября 2000 г.

Письма в ЭЧАЯ. 2002. №4[113] Particles and Nuclei, Letters. 2002. No.4[113]

УДК 539.12

# О НЕКОТОРЫХ ОБРАТНЫХ ЗАДАЧАХ ЯДЕРНОЙ ФИЗИКИ

*Б. З. Белашев* [а], *М. К. Сулейманов* [б]

[а]Институт геологии Карельского научного центра РАН, Петрозаводск

[б]Объединенный институт ядерных исследований, Дубна

Рассмотрены некоторые обратные задачи физики высоких энергий и ЯМР-спектроскопии. Для их решения применены методы интегрального преобразования Фурье и максимума энтропии. Интегральные образы экспериментальных распределений информативны при определении пространственно-временных характеристик области генерации частиц и анализе размытых спектров. Работоспособность методов проверена путем сравнения их результатов с данными, полученными независимым образом.

Some inverse problems of high energy physics and NMR spectroscopy are observed. The methods of the Fourier transformation and the maximum entropy technique have been applied for their solutions. The integral images of the experimental distributions are informative for determination of the space-time characteristics of the particles generation domain and for the analysis of blurring spectra. These methods have been tested in comparision with the results which have been obtained independently.

Обратная задача возникает там, где искомая информация не может быть получена при помощи прямых измерений. Большинство обратных задач ядерной физики связано с интерпретацией данных экспериментов по рассеянию частиц высоких энергий на мишенях. По картине рассеяния определяют структуру сталкивающихся частиц, потенциал взаимодействия, динамику происходящих при столкновении процессов. В некоторых случаях ядро или частицу рассматривают как зонд с известными магнитным моментом, длиной волны, системой энергетических уровней, а по его взаимодействию с веществом и полем судят о концентрации вещества, особенностях среды или конфигурации поля. Такие обратные задачи типичны для ЯМР- и ЯГР (мессбауэровской)-спектроскопии, нейтронной дифрактометрии, активационного анализа, эмиссионной томографии и других приложений ядерной физики.

В статье рассмотрены некоторые обратные проблемы экспериментов физики высоких энергий [1–7]. Для их решения использованы фильтрационные методы, позволяющие путем фурье-преобразования экспериментальных данных получить результат без сколь-нибудь существенного использования априорных ограничений [3–9]. Это свойство оказывается особенно важным при выборе моделей процессов в случаях, когда экспериментальные распределения совместимы с несколькими моделями, а применение аппроксимационных методов оказывается неэффективным.

При решении обратной задачи возникает вопрос о достоверности полученных результатов. Ответ на этот вопрос может быть дан путем сравнения результатов, полученных независимыми способами. Такое сравнение проведено на примере размытых спектров,

разрешение которых повышено применением аппаратурных средств и апостериорно при помощи метода максимума энтропии (ММЭ) [8, 9].

Цель работы состоит в том, чтобы продемонстрировать применимость однотипных математических и алгоритмических подходов на основе интегральных преобразований к решению некоторых обратных задач ядерной физики.

## ПРОСТРАНСТВЕННО-ВРЕМЕННЫЕ ХАРАКТЕРИСТИКИ ПРОЦЕССА МНОЖЕСТВЕННОГО РОЖДЕНИЯ ЧАСТИЦ

В подходе Подгорецкого–Копылова пространственно-временные характеристики процесса множественного рождения частиц можно получить, изучая корреляции тождественных частиц с близкими 4-импульсами [1]. Вероятность $W(q_0, \mathbf{q})$ обнаружения двух тождественных частиц с 4-импульсами $P_1 = \{\epsilon_1, \mathbf{p}_1\}$ и $P_2 = \{\epsilon_2, \mathbf{p}_2\}$, испущенных двумя неподвижными точечными источниками с координатами $\{t_1, \mathbf{r}_1\}$ и $\{t_2, \mathbf{r}_2\}$, выражают формулой

$$W(q_0, \mathbf{q}) = 1 + \frac{\cos\left[\mathbf{q}(\mathbf{r}_1 - \mathbf{r}_2) - q_0(t_1 - t_2)\right]}{1 + (q_0\tau)^2}, \tag{1}$$

где $\mathbf{q} = \mathbf{p}_1 - \mathbf{p}_2$, $q_0 = \epsilon_1 - \epsilon_2$, $\tau$ — время жизни источников. Для тождественных частиц одинаковой энергии $q_0 = 0$ зависимость определена пространственной переменной $\mathbf{R} = \mathbf{r}_1 - \mathbf{r}_2$:

$$W(\mathbf{q}) = 1 + \cos(\mathbf{qR}). \tag{2}$$

Пусть $f(\mathbf{R})$ — нормированное пространственное распределение источников частиц по переменной $\mathbf{R}$. Тогда формула (2) для вероятности $W(\mathbf{q})$ имеет вид

$$W(\mathbf{q}) = 1 + \int f(\mathbf{R}) \cos(\mathbf{qR})\, d\mathbf{R}. \tag{3}$$

При этом в силу нумерации тождественных частиц двумя равноправными способами $f(\mathbf{R}) = f(-\mathbf{R})$ функция $W(\mathbf{q})$ не зависит от знака $\mathbf{R}$, а интегральное слагаемое в (3) является фурье-образом $F(\mathbf{q})$ функции $f(\mathbf{R})$

$$W(\mathbf{q}) = 1 + F(\mathbf{q}). \tag{4}$$

По экспериментальной зависимости $W(\mathbf{q})$ находим фурье-образ

$$F(\mathbf{q}) = W(\mathbf{q}) - 1, \tag{5}$$

а по нему путем обратного преобразования Фурье определяем функцию распределения $f(\mathbf{R})$.

В столкновениях тождественных частиц при условии независимости источников частиц из экспериментальных данных можно получить информацию непосредственно о плотности распределения источников в области генерации $\rho(\mathbf{r})$ [3]. Фурье-образ $G(\mathbf{q})$ функции $\rho(\mathbf{r})$ вычисляют по формуле

$$G(\mathbf{q}) = \sqrt{W(\mathbf{q}) - 1}. \tag{6}$$

Полученную обратным преобразованием Фурье трехмерную функцию $\rho(\mathbf{r})$ удобно представить в виде сечений области генерации системой параллельных плоскостей или проекцией области генерации на плоскость, перпендикулярную заданному направлению. Условие $\rho(\mathbf{r}) \geqslant 0$ ограничивает экспериментальные распределения определенным классом функций. Это ограничение автоматически снимается, если реконструкцию распределения источников вести по его фурье-образу с применением ММЭ [8].

Отбор тождественных частиц с $\mathbf{q} = 0$ для определения функции распределения источников по переменной $t = t_1 - t_2$ невозможен, так как приводит к значению $q_0 = 0$, что следует из условия, связывающего массы, энергии и импульсы тождественных частиц.

При рассмотрении общего случая мы не будем накладывать ограничений на величину $q_0$. Введем нормированную функцию распределения $f_1(\mathbf{R}, t, \tau)$ и преобразуем формулу (1) с учетом известного тригонометрического тождества косинуса разности

$$W(q_0, \mathbf{q}) = 1 + \int f_1(\mathbf{R}, t, \tau) \frac{\cos(\mathbf{qR}) \cos(q_0 t) d\mathbf{R} dt d\tau}{1 + (q_0\tau)^2} + \\ + \int f_1(\mathbf{R}, t, \tau) \frac{\sin(\mathbf{qR}) \sin(q_0 t) d\mathbf{R} dt d\tau}{1 + (q_0\tau)^2}. \quad (7)$$

Последнее интегральное слагаемое в формуле (7) равно нулю вследствие равноправности нумерации частицы в паре, четности функции $f_1(\mathbf{R}, t, \tau)$ и нечетности синуса по переменным $\mathbf{R}$ и $t$.

В предположении о независимости пространственного, временного и релаксационного распределений, описываемых соответственно нормированными функциями $f(\mathbf{R})$, $\chi(t)$ и $\varphi(\tau)$, выраженной условием $f_1(\mathbf{R}, t, \tau) = f(\mathbf{R})\chi(t)\varphi(\tau)$, формулу (7) перепишем в виде

$$W(q_0, \mathbf{q}) = 1 + \int f(\mathbf{R}) \cos(\mathbf{qR}) d\mathbf{R} \int \chi(t) \cos(q_0 t) dt \int \frac{\varphi(\tau)\, d\tau}{1 + (q_0\tau)^2}. \quad (8)$$

Первые два интегральных сомножителя выражения (8) представляют фурье-образы $F(\mathbf{q})$, $X(q_0)$ пространственного и временного распределений, а третий — фурье-образ $C(q_0)$ функции, размывающей временное распределение источников

$$W(q_0, \mathbf{q}) = 1 + F(\mathbf{q}) X(q_0) C(q_0). \quad (9)$$

Произведение $C(q_0)X(q_0)$ находим по наблюдаемым зависимостям $W(q_0, \mathbf{q})$, $W(0, \mathbf{q})$

$$C(q_0)X(q_0) = \frac{W(q_0, \mathbf{q}) - 1}{F(\mathbf{q})} = \frac{W(q_0, \mathbf{q}) - 1}{W(0, \mathbf{q}) - 1}. \quad (10)$$

Функция $C(q_0)$ в эксперименте неизвестна. Выделить фурье-образ $X(q_0)$ из произведения $C(q_0)X(q_0)$ и найти функцию $\chi(t)$ его обратным преобразованием Фурье можно, вводя априорную информацию о распределении источников частиц по времени жизни. Например, равномерное распределение источников $\varphi(\tau) = 1/a$ по времени жизни в интервале $[0; a]$ приводит к функции

$$C(q_0) = \frac{1}{a} \int_0^a \frac{d\tau}{1 + (q_0\tau)^2} = \frac{\operatorname{arctg}(q_0 a)}{(q_0 a)} \quad (11)$$

и позволяет восстановить распределение $\chi(t)$. Результат зависит от вида функции $\varphi(\tau)$.

Структуру распределения $\chi(t)$ также можно получить с помощью метода удвоения и контролируемого смещения пиков или путем фурье-гильберт-фильтрации, позволяющих разделить пики без использования априорных сведений о функции $\varphi(\tau)$ [9]. При этом профили разделенных пиков распределения $\chi(t)$ содержат информацию о функции $\varphi(\tau)$.

Интегральные образы пространственно-временного распределения источников частиц могут быть непосредственно выявлены при специальном представлении данных. В ряде случаев полезными оказываются искусственный переход от экспериментальных распределений к их интегральным образам и нелинейные операции с ними. Существует целый класс таких операций, позволяющих при обратном переходе получить более информативные оценки данных по сравнению с исходными распределениями [9].

## ПОИСК БАРИОННЫХ РЕЗОНАНСОВ В СПЕКТРАХ ЭФФЕКТИВНЫХ МАСС

Предметом исследования являются двухчастичные корреляции продуктов реакции множественного рождения при высоких энергиях, проявляющиеся в распределениях пар вторичных частиц по эффективной массе $M_{\text{эф}}$ и несущие информацию об образующихся в процессе генерации частиц компаунд-системах или резонансах.

Для исследования динамики процесса столкновения интерес представляют $\Delta$-изобары — барионные резонансы, образующие связанную короткоживущую систему из нуклона и $\pi$-мезона. Интерес обусловлен тем, что рождение таких резонансов на ядрах в столкновении адронов с ядрами при низких энергиях может являться основным каналом упругого рассеяния. Изобары могут нести информацию о взаимодействии с другими фрагментами ядра и предоставляют возможность экспериментально изучать цветные степени свободы.

Целью исследования спектров эффективных масс $(\pi^{\pm}p)$ пар в $\pi^-p$- и $\pi^{-12}$C-взаимодействиях при $P_{\pi^-} = 40$ ГэВ/$c$ было определение структуры спектров и установление связи между рождением барионных резонансов и частным случаем множественной генерации адронов — кумулятивным рождением частиц в $\pi^{-12}$C-взаимодействиях [5].

Спектры эффективных масс $(\pi^{\pm}p)$ пар были построены на основе неупругих 11688 $\pi^-p$- и 8642 $\pi^{-12}$C-взаимодействий, полученных при анализе стереофотоснимков с двухметровой пропановой камеры ЛВЭ ОИЯИ, облученной пучком $\pi^-$-мезонов серпуховского ускорителя [2]. Эффективную массу $(\pi^{\pm}p)$ пар рассчитывали по формуле

$$M_{\text{эф}} = \sqrt{m_p^2 + m_\pi^2 + 2(E_pE_\pi - p_pp_\pi \cos\theta)} \qquad (12)$$

с использованием масс протона и $\pi$-мезона — $m_p$ и $m_\pi$, их полных энергий — $E_p$ и $E_\pi$, абсолютных значений импульсов — $p_p$ и $p_\pi$ и угла между импульсами — $\theta$ в л.с. Импульс отобранных протонов составлял от 140 до 700 МэВ/с.

Для установления связи между процессами рождения $\Delta$-изобар и кумулятивного испускания $\pi$-мезонов в $\pi^{-12}$C-взаимодействиях были использованы две схемы отбора вторичных $\pi$-мезонов в событии. В первой схеме учитывали все $\pi$-мезоны события, во второй схеме исключали $\pi$-мезон с максимальным значением порядка кумулятивности $n_c$ в со-

бытии. Порядок кумулятивности определяли в соответствии с формулой $n_c = \dfrac{E - p_{\|}}{m_N}$ через полную энергию $E$, продольный импульс $p_{\|}$ $\pi$-мезона и массу нуклона $m_N$.

Анализ структуры спектров эффективных масс $(\pi^{\pm}p)$ вели с помощью двух методов обработки на основе преобразования Фурье. В первом методе выявляли периодичности в зависимости модуля фурье-образа симметризованного спектра от угловой частоты, по которым определяли положения компонент, сопоставляемые массам резонансов [4]. Результаты применения метода показаны на рис. 1. Положения выделенных особенностей спектров указаны стрелками, ошибки положений — отрезками над стрелками, значение массы близкого к заданному положению пион-нуклонного резонанса — числом.

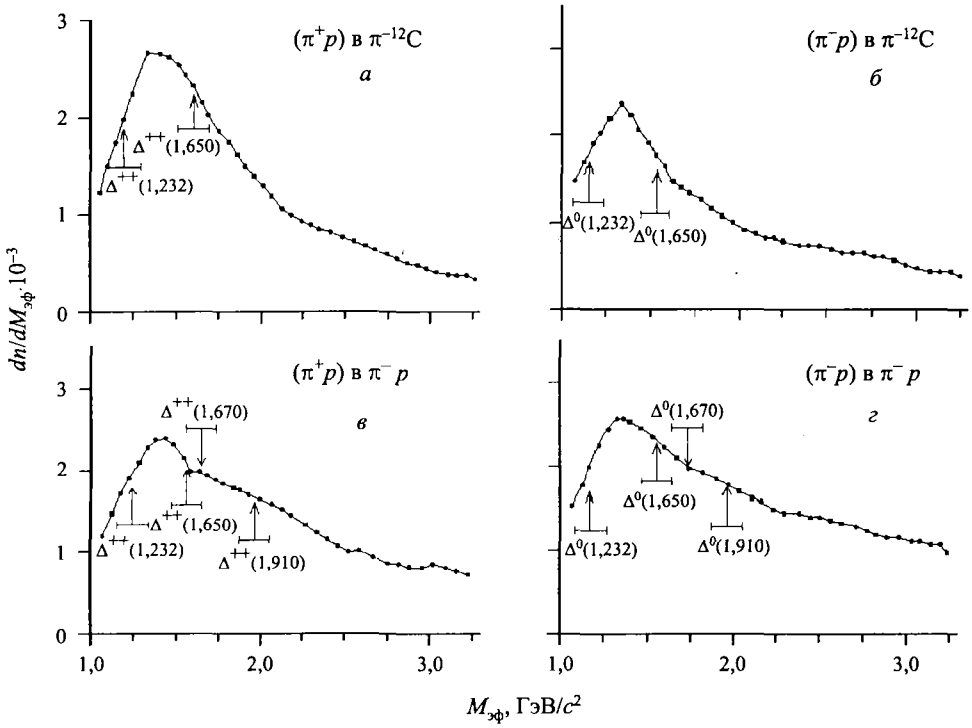


Рис. 1. Результаты применения модифицированного фурье-алгоритма к спектрам эффективных масс $(\pi^{\pm}p)$ пар в $\pi^-p$- (*в*, *г*) и в $\pi^{-12}$C-взаимодействиях (*а*, *б*) при $P_{\pi^-} = 40$ ГэВ/*c*

Во втором методе была использована идея контролируемого регулирования ширин компонент спектра эффективных масс [6, 9]. Уменьшения ширин компонент в оценке спектра достигали умножением фурье-образа спектра на экспоненциальную функцию. При обратном преобразовании Фурье такого образа полученная оценка имела более высокую контрастность по сравнению с первоначальным спектром и содержала особенности, которые по величине эффективной массы могли быть сопоставлены барионным резонансам [5].

Результаты этого метода представлены на рис. 2, на котором приведены экспериментальные распределения $\frac{dN(M_{эф})}{dM_{эф}}$ и полученные оценки $f(M_{эф})$, соответствующие $\pi^{\pm}p$-парам первой схемы отбора $\pi$-мезонов события (*а*, *б*) и $\pi^{\pm}p$-парам второй схемы отбора (*в*, *г*). Главный пик выявленных мультиплетных структур соответствует массе 1,232 ГэВ/$c^2$, дополнительный пик — массе 1,650 ГэВ/$c^2$. Исключение кумулятивных $\pi$-мезонов приводило к равномерному понижению оценки спектра эффективных масс примерно на 30 % без изменения формы.

Полученные особенности в спектрах эффективных масс $\pi^{\pm}p$-пар сопоставлены $\Delta^{++}(1{,}232)$-, $\Delta^{++}(1{,}650)$-, $\Delta^{++}(1{,}670)$-, $\Delta^{++}(1{,}910)$-изобарам в $\pi^{-}p$- и $\Delta^{++}(1{,}232)$, $\Delta^{++}(1{,}650)$ в $\pi^{-12}$C-взаимодействиях. Анализ средней множественности $\pi^{+}$- и $\pi^{-}$-мезонов в $\pi^{-12}$C-взаимодействиях при $P_{\pi^-} = 40$ ГэВ/$c$ с учетом фона показал, что исключение любого $\pi$-мезона в событии приводит к уменьшению $\frac{dN(M_{эф})}{dM_{эф}}$ примерно на 30 %. Этот результат проинтерпретирован, как указание на независимость процессов появления кумулятивных $\pi$-мезонов и рождения барионных резонансов.

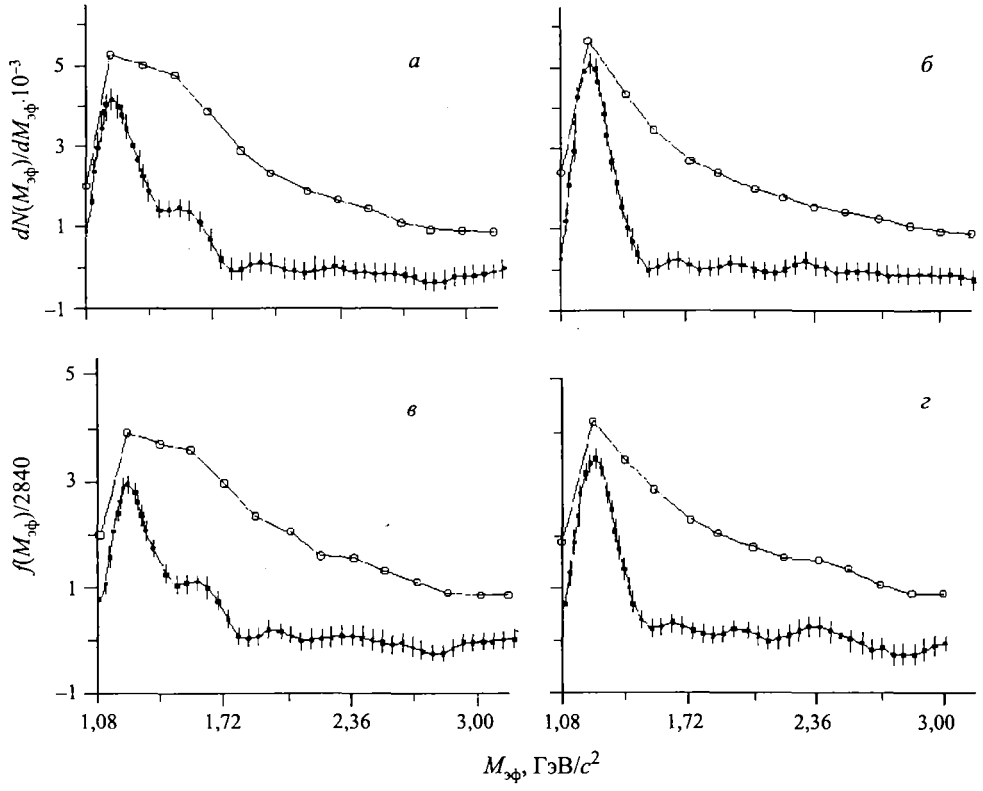


Рис. 2. Спектры эффективных масс $(\pi^{+}p)$ (*а*) и $(\pi^{-}p)$ пар (*б*) $\frac{dN(M_{эф})}{dM_{эф}}$ (○), их оценки $\hat{f}(M_{эф})$ (●) для двух схем отбора $\pi$-мезонов

## СТРУКТУРА РАСПРЕДЕЛЕНИЙ ЧАСТИЦ ПО БЫСТРОТЕ

Согласно современным представлениям о взаимодействии адронов высоких энергий с нуклонами и ядрами основная доля вторичных частиц возникает в процессе адронизации быстрого кварк-партона в струю частиц [10]. Проявляющуюся в близкодействующих корреляциях продуктов взаимодействия струйную адронизацию удобно изучать в распределениях продуктов реакции по быстроте $y = \frac{1}{2} \ln \left( \frac{E + p_{\|}}{E - p_{\|}} \right)$ ($E$ и $p_{\|}$ — соответственно энергия и продольный импульс вторичной частицы), наблюдая группировку частиц относительно нескольких характерных быстрот.

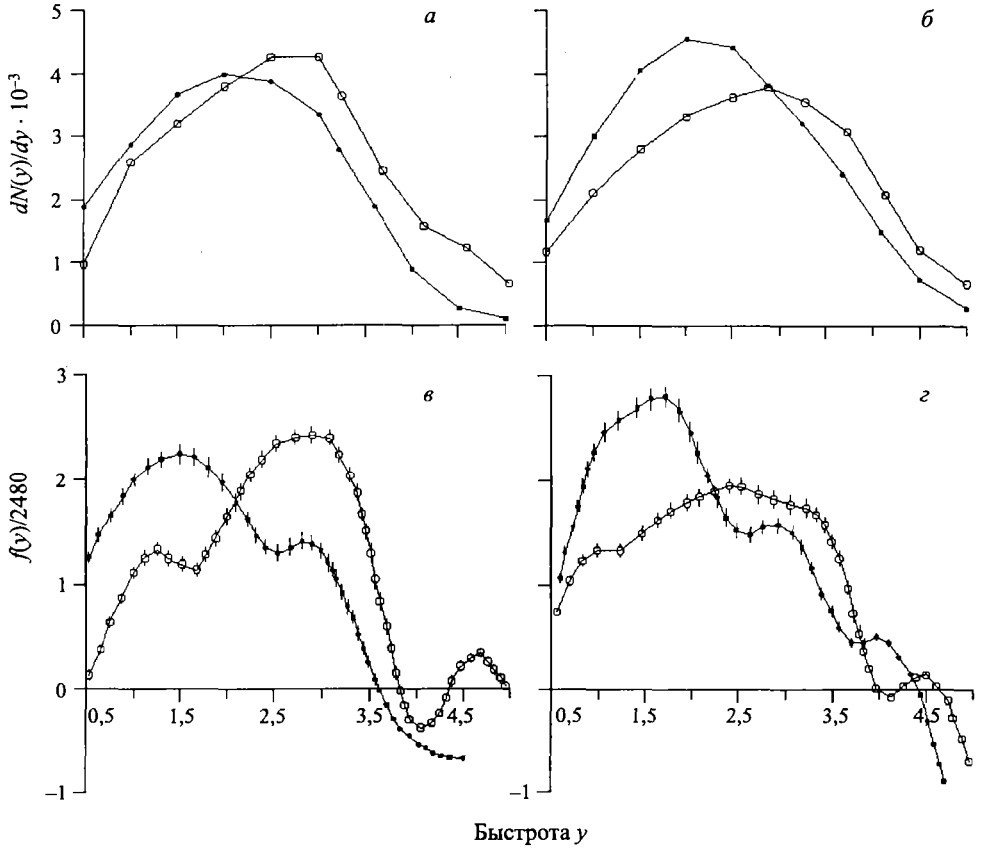


Рис. 3. Распределение $\pi$-мезонов ($\pi^+$ (•), $\pi^-$ (○)) по быстроте в $\pi^- p$- (*а*) и в $\pi^{-12}$C-взаимодействиях (*б*) и их оценки соответственно (*в*) и (*г*), полученные при помощи фурье-алгоритма регулирования ширины спектральных линий

Типичным является случай, когда распределения по быстроте представляют гладкие кривые без видимых характерных особенностей, что затрудняет выделение струй. Для

выявления характерных быстрот процесса множественного рождения $\pi^{\pm}$-мезонов в реакциях $\pi^- p$ и $\pi^{-12}$C при $P_{\pi^-} = 40$ ГэВ/$c$ [7] был применен ранее использованный метод уменьшения ширин компонент распределений [6, 9].

Исходные данные и результаты применения метода приведены на рис. 3. Распределения по быстроте $\pi^{\pm}$-мезонов в этих реакциях (*а, б*) сильно размыты, а их контрастные оценки (*в, г*) демонстрируют сложную структуру. В $\pi^- p$-взаимодействии оценка распределения по быстроте $\pi^+$-мезонов является дублетом с модами $\approx$ 1,4 и 2,8, для $\pi^-$-мезонов — триплетом с модами $\approx$ 1,2; 2,8; 4,7. В $\pi^{-12}$C-взаимодействиях оценка распределения по быстроте для $\pi^+$-мезонов содержит три пика с быстротами $\approx$ 1,4; 2,8; 3,3, а для $\pi^-$-мезонов — три пика с быстротами $\approx$ 0,9; 2,5; 4,4, причем второй пик оказывается сильно размытым в интервале быстрот 1,8–3,2.

Полученные результаты позволяют сопоставить характерные быстроты вторичных $\pi$-мезонов в диапазонах 1,0–1,6; 1,8–3,2; 4,0–4,4 областям фрагментации мишени, налетающей частицы и сохранению налетающего $\pi$-мезона. Число и значения характерных быстрот процесса зависят от массы мишени и зарядов вторичных $\pi$-мезонов.

## ЯМР-СПЕКТРЫ ТВЕРДЫХ ТЕЛ

Явление магнитного резонанса характерно для ядер со спином, отличным от нуля, помещенных в магнитное поле, и проявляется в прецессии магнитных моментов. Несущие химическую, биофизическую и медицинскую информацию, ЯМР-спектры регистрируют при взаимодействии магнитных моментов ядер с электромагнитным излучением, содержащим частотные компоненты вблизи частоты Лармора, или в результате быстрых изменений ориентации внешнего магнитного поля под действием специальных последовательностей радиочастотных импульсов, инициирующих переходные процессы в системе ядерных спинов [11]. Применение таких последовательностей позволило эффективно усреднить спин-спиновое взаимодействие ядер в твердых телах и получить их ЯМР-спектры, не уступающие по разрешению ЯМР-спектрам жидкостей.

Возможность зарегистрировать ЯМР-спектр поликристаллического образца с различным разрешением позволяет, применяя к спектру низкого разрешения ММЭ-способ введения пробных функций размытия [9], сравнить полученную оценку со спектром высокого разрешения. В данной задаче работоспособность ММЭ-способа проверена на примере размытого ЯМР-спектра органического соединения адамантана, имеющего постоянный уровень фона.

На рис. 4 показан ЯМР-спектр $^{13}$C адамантана (*а*), зарегистрированный методом вынужденной прецессии (кривая *1*) и с помощью последовательности импульсов (кривая *2*) [11], а также ММЭ-оценка (кривая *3*) и ее штрихдиаграмма (кривая *4*) (*б*), полученные при обработке размытого спектра (кривая *1*).

Произвольное положение по оси ординат, отсутствие информации о постоянной составляющей фона обычно затрудняют обработку и интерпретацию такого спектра. Действительно, штрихдиаграмма ММЭ-оценки спектра содержит целую серию пиков, большинство из которых имеет фоновое происхождение. Характерным, однако, является наличие в ММЭ-оценке двух интенсивных пиков, отражающих истинную структуру зарегистрированного ЯМР-спектра высокого разрешения.

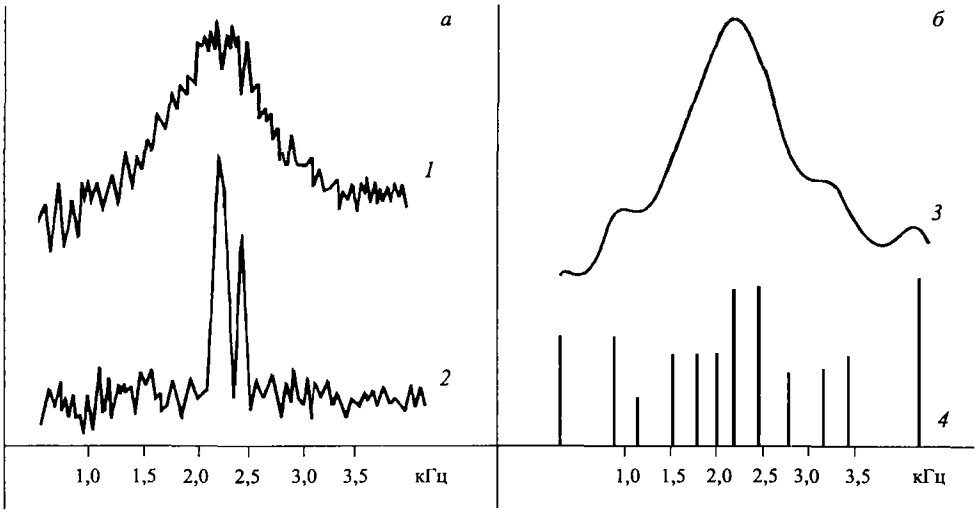


Рис. 4. *а*) ЯМР-спектр $^{13}C$ адамантана, зарегистрированный методом вынужденной прецессии (*1*) и с помощью $\pi/2$-, $\pi$-последовательности РЧ-импульсов (*2*); *б*) ММЭ-оценка кривой *1* (*3*) и ее штрихдиаграмма (*4*)

Пример указывает на необходимость точного учета фона размытого спектра для получения правильных выводов о его структуре, но также демонстрирует возможность определения положения наиболее интенсивных компонент размытого спектра даже при отсутствии информации о постоянной составляющей фона.

## ВЫВОДЫ

1. На основе интерференционного подхода описан метод реконструкции пространственно-временных характеристик области генерации частиц в столкновениях частиц высоких энергий по наблюдаемым распределениям пар вторичных тождественных частиц по разности их импульсов $\mathbf{q}$ и энергий $q_0$. Решение обратной задачи проведено в рамках статической модели источников частиц. В этой модели связь экспериментальных данных с интегральными образами пространственно-временных распределений источников частиц выражена наиболее просто. В более реалистичных моделях процесса множественного рождения частиц [12] эта связь осложнена движением источников и зависимостью координат $q_0$ и $\mathbf{q}_\parallel$. Статистическая обеспеченность современных экспериментов физики высоких энергий способствует применению метода.

2. При поиске барионных резонансов и характерных быстрот в реакциях $\pi^- p$- и $\pi^{-12}C$-взаимодействий при $P_{\pi^-} = 40$ ГэВ/$c$ применение методов фурье-анализа размытых спектров позволило установить особенности структуры экспериментальных распределений и сопоставить их известным $\Delta$-изобарам и областям фрагментации продуктов реакции в пространстве быстрот. Результаты, полученные при анализе спектров эффективных масс $\pi^{\pm} p$-пар с использованием различных схем отбора $\pi$-мезонов в событии, указывают на независимость процессов образования $\Delta$-изобар и испускания кумулятивных

$\pi$-мезонов. Данный подход может быть использован при поиске разнообразных резонансов, мультикварковых систем, экзотических мезонов и чисто глюонных состояний [13].

3. В обратных задачах прикладной ядерной физики, относящихся к области нейтронной дифрактометрии и ЯМР, методы анализа размытых спектров на основе ММЭ привели к результатам, сравнимым с результатами аппаратурных методов высокого разрешения. Высокая информативность ММЭ-методов подтверждена при обработке простых и сложных спектров в условиях, когда информация о постоянной составляющей фона спектра отсутствует.

Авторы выражают благодарность В. Л. Любошицу и С. С. Шиманскому за полезное обсуждение.

## СПИСОК ЛИТЕРАТУРЫ

1. *Копылов Г. И., Подгорецкий М. И.* Функции взаимной когерентности и множественное рождение // ЯФ. 1974. Т. 19. С. 434–446.

2. *Аношин А. И., Любимов В. Б., Сулейманов М. К.* Изучение $\pi^{-}{}^{12}$C-взаимодействий при $P_{\pi^-} = 40$ ГэВ/с, сопровождающихся испусканием кумулятивных $\pi$-мезонов // ЯФ. 1980. Т. 31, вып. 3. С. 668–673.

3. *Белашев Б. З., Сулейманов М. К., Чеплаков А. П.* Определение пространственных характеристик процесса множественного рождения частиц. Препринт ОИЯИ 1-80-150. Дубна, 1980.

4. *Аношин А. И. и др.* Поиск барионных резонансов в спектрах эффективных масс ($\pi^{\pm}p$) пар при помощи модифицированного фурье-алгоритма. Препринт ОИЯИ Р1-80-574. Дубна, 1980.

5. *Аношин А. И. и др.* Анализ спектров эффективных масс ($\pi^{\pm}p$) пар в $\pi^{-}{}^{12}$C-взаимодействиях при помощи фурье-алгоритма. Препринт ОИЯИ Р1-81-680. Дубна, 1981.

6. *Аношин А. И. и др.* Анализ спектров, содержащих резонансы, при помощи фурье-алгоритма. Препринт ОИЯИ Р1-81-679. Дубна, 1981.

7. *Аношин А. И. и др.* Анализ распределений по быстроте $\pi$-мезонов в реакциях $\pi^{-}p$- и $\pi^{-}{}^{12}$C-взаимодействий при помощи фурье-алгоритма. Препринт ОИЯИ Р1-81-68. Дубна, 1981.

8. *Белашев Б. З., Сороко Л. М.* Обработка данных методом максимума энтропии. Препринт ОИЯИ Р10-80-696. Дубна, 1980.

9. *Белашев Б. З.* Методы реконструкции размытого спектра // Журн. прикл. спектроск. 2001. Т. 68, вып. 5. С. 639–644.

10. *Никитин Ю. П., Розенталь И. Л.* Ядерная физика высоких энергий. М., 1980.

11. *Уо Дж.* Новые идеи в ЯМР. М.: Мир, 1975.

12. *Подгорецкий М. И.* Интерференционные корреляции тождественных пионов. Теория // ЭЧАЯ. 1989. Т. 20. С. 628–668.

13. *Adams G. S. et al.* Observation of a New $J = 1$ Exotic State in Reaction $\pi p \to \pi\pi\pi p$ at 18 GeV/c // Phys. Rev. Lett. 1998. V. 81, No. 26. P. 5760–5763.

Получено 6 апреля 2001 г.

Письма в ЭЧАЯ. 2002. №4[113] Particles and Nuclei, Letters. 2002. No.4[113]

УДК (539.143+539.126):539.12...162.8

# THE NUCLEAR MATTER MODIFICATION AT INTERMEDIATE ENERGIES

*Vl. Penev*[1], *A. Shklovskaia*[2]

Joint Institute for Nuclear Research, Dubna

Рассматривается гипотеза о взаимодействии адронов с веществом ядер, где, как предполагается, наряду с нуклонами ядра в качестве мишени для налетающего адрона могут служить известные частицы, резонансы и, возможно, кварки. Проверка гипотезы была проведена на основе экспериментальных данных о CC-, $d$C-, CTa-, $p$C-взаимодействиях при 4,2 ГэВ/с/нуклон. Кроме того, анализ рождения $\Delta(1232)\,P_{33}$-, $N(1440)\,P_{11}$-изобар и $\rho$-мезонов в этих же взаимодействиях обнаруживает некоторое подавление их образования в рассматриваемых ядрах по сравнению с взаимодействиями на нуклонах, что, возможно, связано с образованием в ядре плотной «резонансной» материи.

A new hypothesis on hadron interactions with nuclear matter is discussed. It is supossed that the well-known particles and resonances as well as nucleons might serve as a target in the nucleus. The experimental data on CC, $d$C, CTa, $p$C interactions at 4.2 GeV/c/nucleon are used for the testing of the hypothesis. A certain suppression of production of the $\Delta(1232)\,P_{33}$, $(1440)\,P_{11}$ isobars and $\rho$ mesons is observed in these interactions, compared to the nucleon–nucleon interactions. It may be caused by the formation of the so-called dense «resonance matter» in the nucleus. Special experiments with multiple rising statistics are required to examine the hypothesis.

## INTRODUCTION

During 60–70s of the last century it was accepted that the difference between the free nucleon and the nucleon inside a nucleus is very small. Naturally, the nucleons are bound in the nucleus, but the binding energy is not great and it may affect only the value of the total interaction energy. A lot of models were developed to describe cascade mechanisms of hadron interactions in the nuclear matter.

A few years later, the anomalous number of hadrons with high momentum were registered in hadron–nucleus collisions at LHE and ITEPH, that contradicts the kinematics of the hadron–nucleon interactions. To explain the effect, A.M.Baldin [1] supposed that some nuclei interactions could be descended on a group of nucleons, but the nucleons do not lose their identity in the nuclear matter. Hence, the name «cumulative» appeared for the produced particles with «wrong» kinematics.

On the other hand, the well-known particles — mesons and resonances, realizing the interactions between nucleons, might attend virtually in the nuclei. And, finally, the particles deconfined in nuclei lead to [2] the presence of a small part of «free» quarks and gluons in the nuclei. The same quarks, as well as mesons and resonances may be examined as target objects inside the nucleus (Sec. 1).

[1]e-mail: penev@lhe.jinr.ru

[2]e-mail: alla@lhe.jinr.ru

The problem, how the properties of hadrons in the nuclear matter change in comparison with their free state, attracts a great deal of attention. Yet it is known that the nucleon mass $m_N^*$ in nuclear environment is not equal to $m_N$, although there is no consent about its exact value. Quite approximately it would be accepted that in the middle of the nuclei (where nuclear density is $\rho_0$) $m_N^*(\rho_0)/m_N \approx 0.8$. The remarkable consequence from this estimation is [3] that the quark condensate has dropped by $\sim 50\,\%$ in the middle of nuclei. Other particles also change their masses, and the difference between «free mass» and the «bound mass» increases with the particle mass.

The energy $E$ ($E \geqslant m_N$, where $m_N$ is a nucleon mass) coming in the nuclei can strongly modify the nuclear matter in some part of the nucleus, or in the whole one, changing the particle parameters. But the search for free particles and resonances, with modified parameters, has not been successful so far.

While the high-energy colliders try to probe the hot quark–gluon plasma at the low net baryon density, the matter, possibly the quark-matter, may be produced at rather high baryon density and moderate temperature on the fixed target at the Nuclotron. Reproduction of hadron distributions on the base of central Si + A collisions data at the AGS at freeze-out shows baryon densities exceeding the nuclear matter density five times for a typically extended time of about 5 fm/c [4, 5].

Intensive production or «dressing» of resonances in such conditions increase the matter density even more. Metag [6] on the base of calculations of S. A. Bass et al. [7] and S. Teis et al. [8] concluded that for 30 % of nucleon resonance population at 2 $A \cdot$ GeV, the mean distance between separate constituents becomes $\sim$ 2 fm attaining the boundary in strong interactions. Thus the density of resonances is so high that they start interacting with each other, and then we can speak about these systems as of the resonance matter.

The resonances are produced intensively in elementary particle interactions at 2–4 GeV, whereas in nuclear–nuclear interactions the resonances are hardly found at the same energies. What is the reason? We shall try to give the answer in Sec. 2.

## 1. MODIFICATION OF THE «TARGET»

So, the first hypothesis for testing was the following one: inside one nucleus there are a lot of known objects ready to serve as a target for incident particles. So, the experimental data [10] on CC, $d$C, CTa, $p$C interactions at 4.2 GeV/c/nucleon were analyzed.

**1.1. Method of Testing.** The way of target investigation was prompted by a very handy target–mass analysis, proposed 40 years ago by N. G. Birger and Yu. A. Smorodin [9]. Following [9] we write the target–mass $M_t$ as:

$$M_t = \Sigma_i (E_i - p_{\mathrm{II}i}) - \epsilon_0. \tag{1}$$

Here, $E_i$, $p_{\mathrm{II}i}$ are the energy and the longitudinal momentum of the particles produced in the interaction; $(i = 3, \ldots (n_{\mathrm{ch}} + 2))$, $(\epsilon_0 = E_1 - p_1)$, $E_1$, $p_1$ determine the initial energy and momentum.

In the case of the moving target, $M_t$ distribution looks like a peak at

$$M_{\mathrm{eff}} + \langle T_{\mathrm{eff}} - U_{\mathrm{eff}} \rangle, \tag{2}$$

where $T_{\rm eff}$ and $U_{\rm eff}$ are the kinetic and potential energies of the interacting objects. The width is determined by the target Fermi-momenta inside the nucleus $p_{\rm eff\|}$, and $\langle p_{\rm eff\|}\rangle = 0$.

The invariant target mass square is

$$M_x^2 = (\Sigma P_i - P_1)^2. \tag{3}$$

Here $P_1$ and $P_i$, the four-momenta of the initial and produced particles, were also used for the testing.

**1.2. Background Reduction**

(i) Indeed, in the propane bubble chamber the distinction of protons from $\pi^+$ mesons was successful to the momentum of $\sim 0.7$ GeV/c only. At the higher momenta the identification was made by the statistic weight, $w_p$, [11]. To reduce the neutron contribution, the events with only one well-identified proton were taken into account.

(ii) Bad measured tracks, the lost particles, as well as the events containing unambiguously identified particles were taken into account with the help of the corresponding weights [11].

(iii) Obviously, the proposed consideration requires all particles to be registered thoroughly. To exclude the events, in which neutral particles were not registered, as well as to share out the effect, the test of transverse momentum compensation was applied. The request of the transverse momentum compensation means that a sum of transverse momentum components $p_{xi}$ and $p_{zi}$ does not exceed a small value, designated as the $p_x$ and $p_z$ limits simultaneously. Figure 1 shows transverse momenta of all charged particles produced in CC interactions at 4.2 GeV/c [10]. The events from the narrow stripes were taken for the further analysis.

(iv) *The missing-mass method.* The method was used for the separation of the events which were suitable to the definite process kinematics. The missing mass square was written as:

$$M_{\rm mis}^2 = (\Sigma P_i - (P_1 + P_2))^2, \tag{4}$$

or:

$$M_{\rm mis}^2 = ((E_1 + M_{\rm targ}) - \Sigma E_i)^2 - (\mathbf{p}_1 - \Sigma \mathbf{p}_i)^2, \tag{5}$$

where $P_1$, $P_2$ are the four-momenta of the initial particles; $P_i$ is the four-momentum of the produced particles; also $E_1$, $\mathbf{p}_1$ and $E_i$, $\mathbf{p}_i$ are the energies and momenta of the initial and produced particles, respectively; $M_{\rm targ}$ is the mass of the object, on which the interaction took place. The width of the maximum at $M_{\rm mis}^2 = 0$ is determined by target Fermi-momenta, by the measured errors and, of course, by a natural width of resonance, if it occurs to be a target.

Separation of definite reactions (CC and C$p$ from C-$C_3H_8$ or $p$C and $pp$ interactions from $p$-$C_3H_8$) was made by the weights, calculated in [11] on the base of the known inelastic cross section and some additional criteria. Figure 2 demonstrates the spectra of some separate channels. All necessary weights are used here and the nucleon mass is taken as $M_{\rm targ}$. Further, the missing mass spectra, received in different assumptions about $M_{\rm targ}$ value: $M_{\rm targ} = M_N$, $M_\rho$, $M_\pi$, and $\sim M_q$, were calculated. The events having the $M_{\rm mis}^2$ values inside the narrow region near zero of the appropriate distribution correspond to the process, which is searched for.

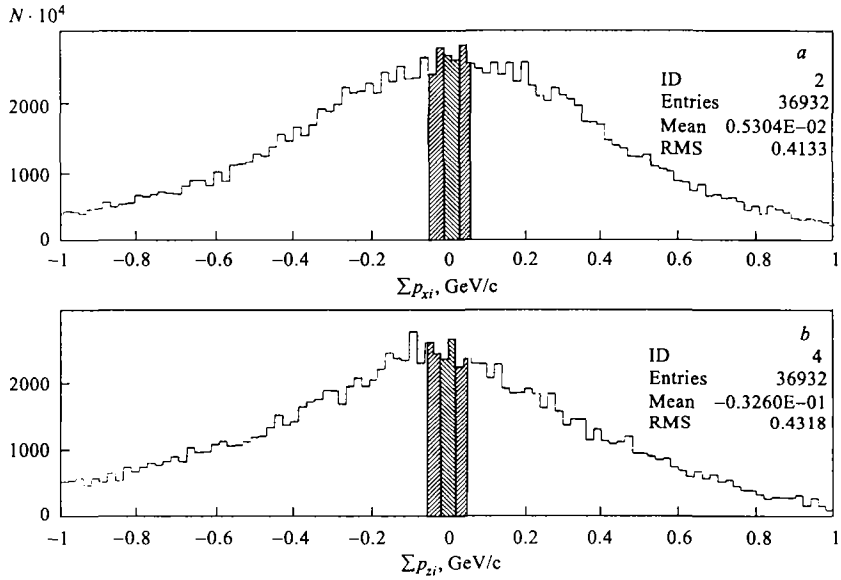


Fig. 1. Summary transverse-momentum components $\sum p_{xi}$ (*a*) and $\sum p_{zi}$ (*b*) for all measured CC interactions. The request of the transverse momentum compensation means that the $\sum p_{xi}$ and $\sum p_{zi}$ do not exceed any small value simultaneously — only the events from the narrow stripes of $\sum p_{xi}$ and $\sum p_{zi}$ are taken for the analysis

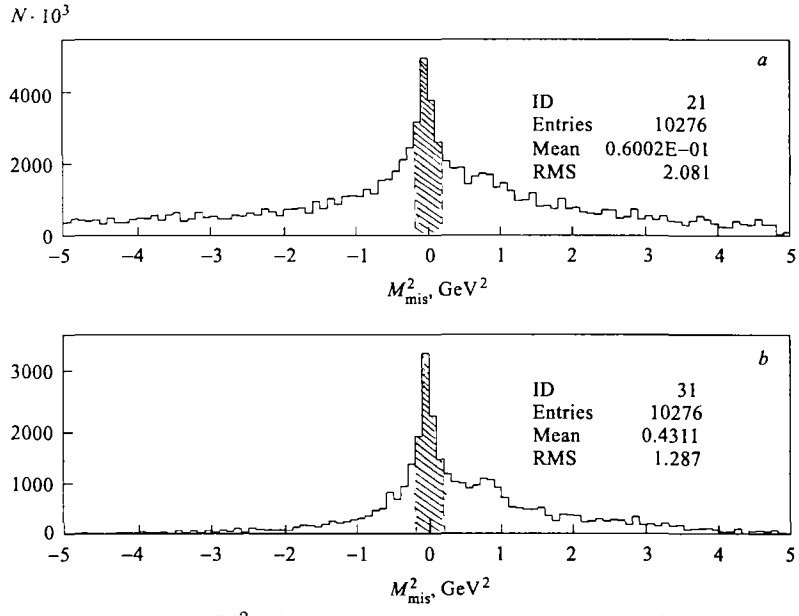


Fig. 2. Missing-mass spectrum $M^2_{\rm mis}$ for $p$C (*a*), $p$C and $pp$ interactions (*b*) from $p$-Pr with weights $w_t$ and $w_p$. The mass of the target is: $M_{\rm targ} = M_N$

**1.3. «Targets» Inside the Target.** The mass-targets $M_t$ for different demands on transverse momentum balance are shown in Fig. 3, *a, b, c, d*. All criteria besides «missing mass»

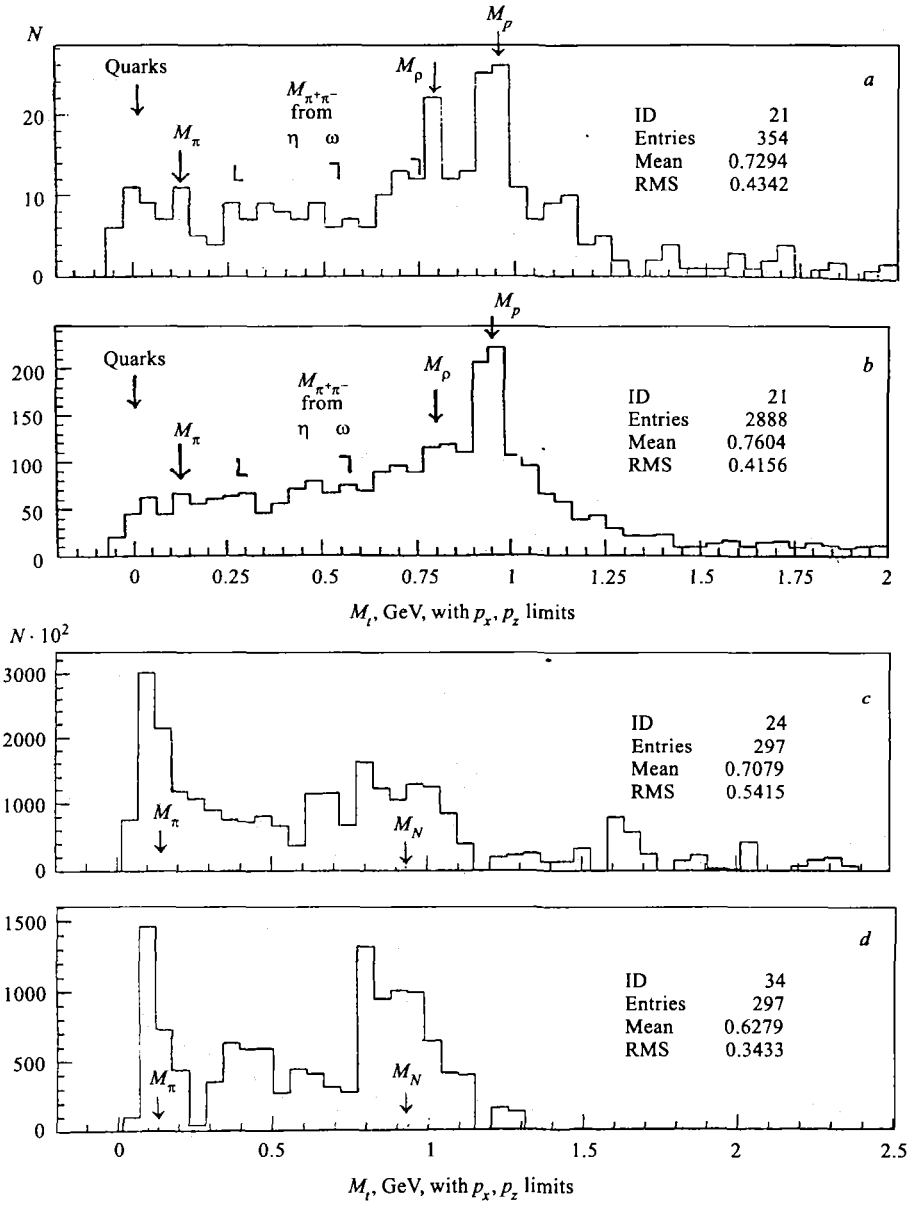


Fig. 3. Mass-target ($M_t$) distributions with transverse momentum balance: *a*) $\Delta\sum p_t$ = sqrt $((\sum p_{xi})^2 + (\sum p_{zi})^2) = \pm 70$ MeV/c; *b–d*) $\Delta\sum p_t$ = sqrt $((\sum p_{xi})^2 + (\sum p_{zi})^2) = \pm 140$ MeV/c. C-$C_3H_8$ interactions without weights (*a, b*); *p*C (*c*) and *pp* interactions (*d*) from *p*-$C_3H_8$ interactions with weights $w_t$, $w_p$, and $w_e$

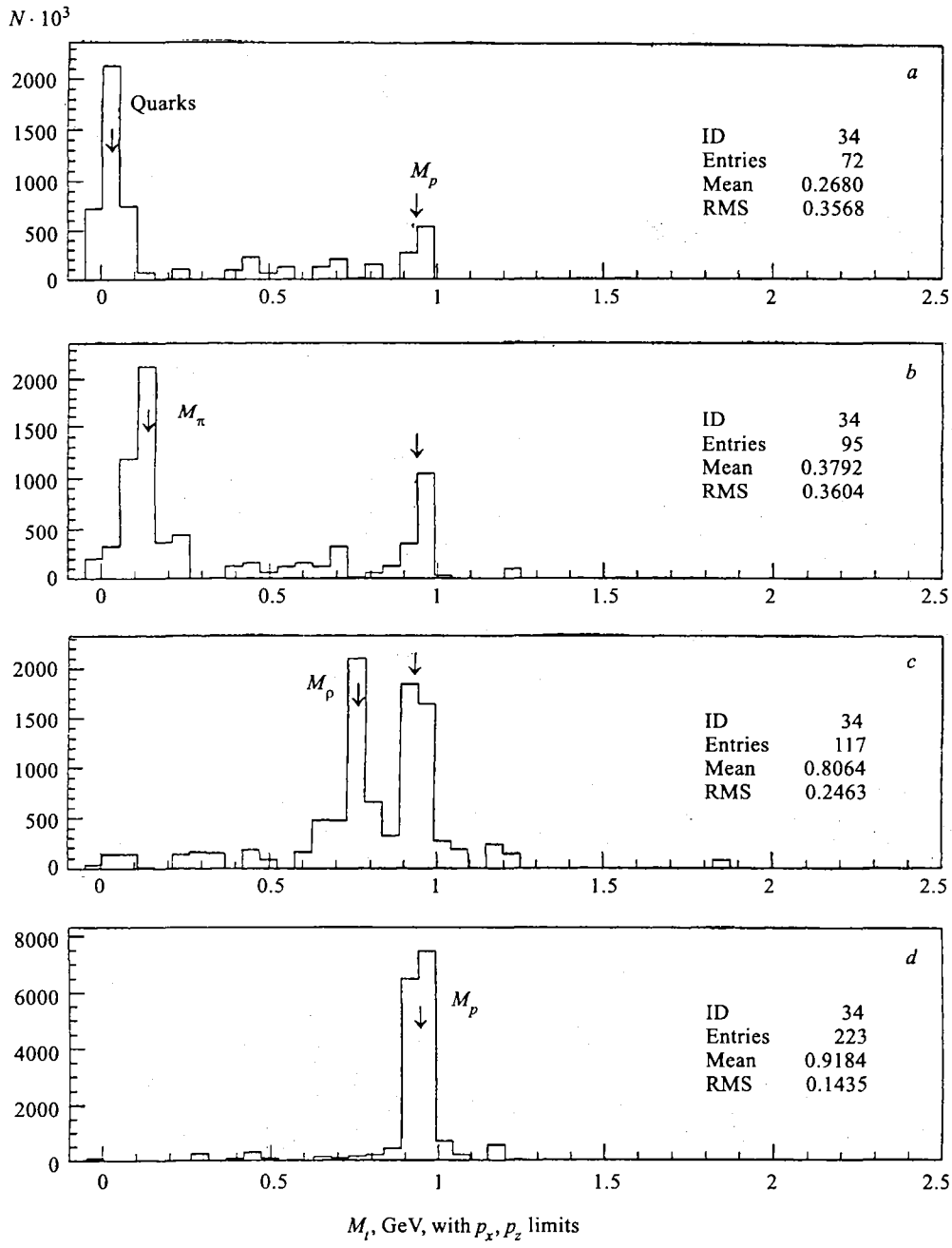


Fig. 4. Mass–target ($M_t$) distributions of the candidates for separate reactions of protons with quarks (*a*), $\pi$ mesons (*b*), $\rho$ mesons (*c*) and nucleons (*d*) for C*p* interactions

were used here. As seen from the figure, the nucleon was used as a target approximately in 30 % of the events, a lot of them (~ 20 %) have the mass–target less than a proton mass. For

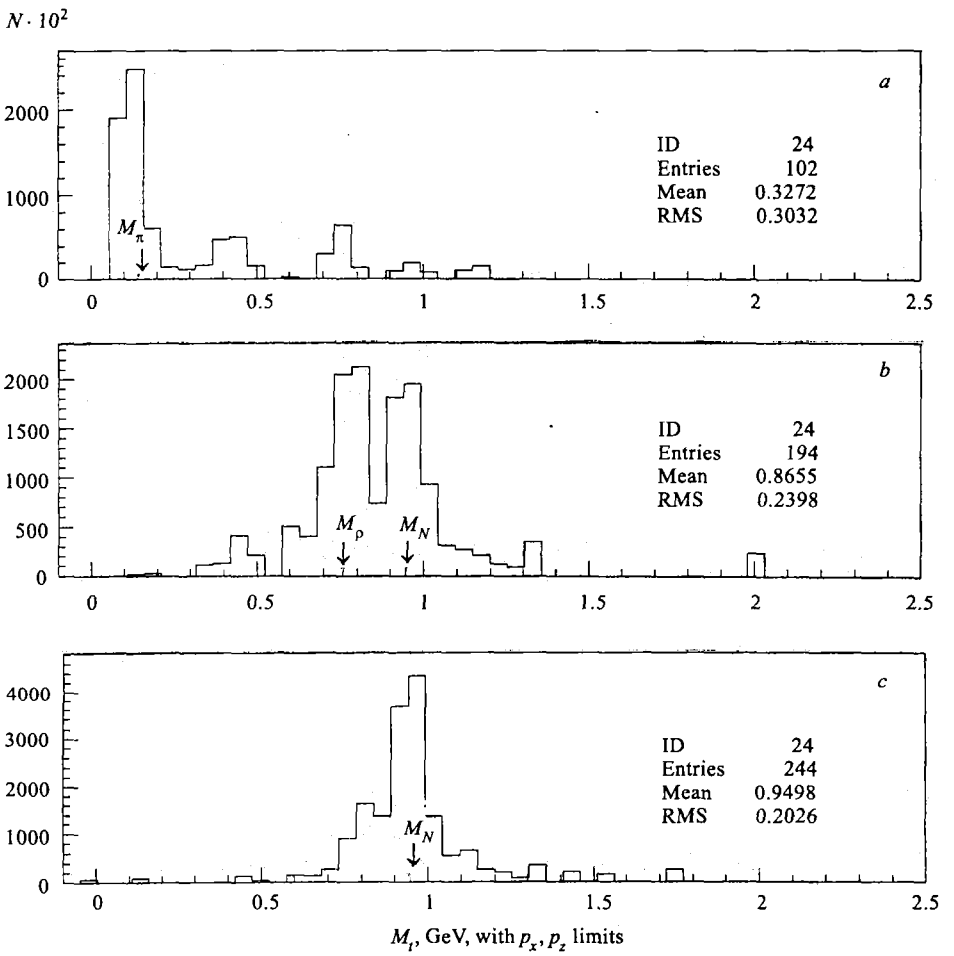


Fig. 5. Mass–target ($M_t$) distributions of the candidates for separate reactions of protons with $\pi$ mesons (*a*), $\rho$ mesons (*b*) and nucleons (*c*) for *p*C interactions

those last events the separate groups may be identified with the ones where quarks or $\pi$ mesons, pairs $\pi^+\pi^-$, rest from $\omega$, $\eta$ mesons, or $\rho$ mesons, are used as a target.

Further the missing-mass method (iv) was applied to C*p*, *p*C, and *pp* interactions. The results are shown in Figs. 4, 5, 6. The groups of events where initial particles interacted with objects having the mass equal or less than the nucleon mass, are separated clearly.

$M_x^2$ distributions demonstrate the same effects, but they are not so descriptive as at the $M_t$ spectra.

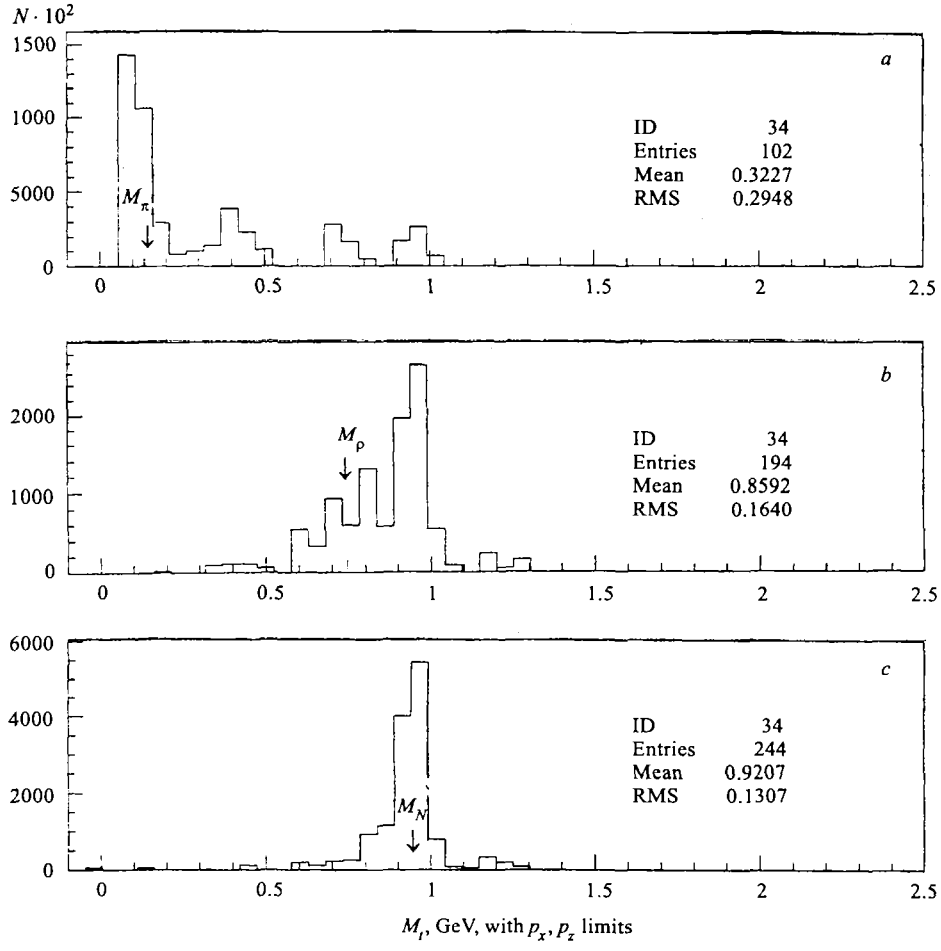


Fig. 6. The same as in Fig. 5 for *pp* interactions

## 2. RESONANCE MATTER — DOES IT EXIST?

The energy of interactions puts in action the resonances, already existing in the nucleus, or excites the new ones. If the region of the produced resonances occupies a small value, then, perhaps, in that region the dense resonance matter is produced.

**2.1. Resonance Source Dimensions.** The question is: what is the dimension of the resonance source $R_{\rm sp}$ in the nuclei determined in experiments?

Many of the particles produced can be the result of resonance decay. Thus, the measuring radii $R_{\rm sp}$ or $R_{\rm tr}$ include, besides dimensions of the original producing region, the decay range of intervening particle, the path of the particle to eventual secondary interactions, etc. Therefore the $R_{\rm sp}$ or $R_{\rm tr}$, obtained up to now are not exact values.

The interference effect between identical particles is used to measure the source dimensions. But the resonances prefer to decay into nonidentical particles.

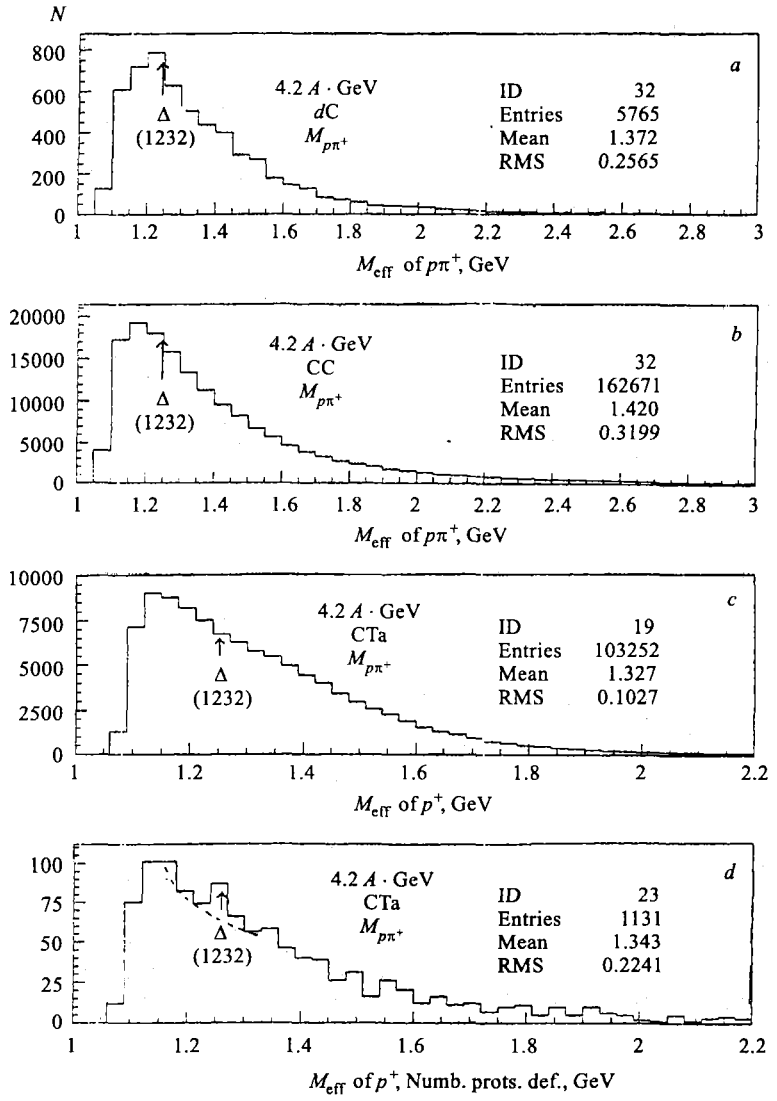


Fig. 7. Effective mass ($M_{p\pi+}$) distributions for nuclear–nuclear interactions at 4.2 GeV: *a*) for *d*C interactions; *b*) for CC interactions; *c*) for CTa interactions; *d*) for CTa events with multiplicities of charged particles $n_s < 6$

In the case, when one of the two identical particles comes directly from its source and the other one comes from the decay of intervening particle (or resonance), the correlation between these particles is determined by the intervening particle decay range $L$ and by the dimension $R$ of the production region.

Proposed by Podgoretsky and Lednitsky [12] and by Grassberger [12], the method of $R_{\text{sp}}$ or $R_{\text{tr}}$ determination with the use of decay range ($L$), was tested in [14] for $Z$-bosons

production and decay into muons in CMS set-up. The results have shown that the interference effects, coming from $Z$ bosons, could be clearly determined, if the source radius of produced $Z$ bosons is small.

Similar research may be applicable to $\phi$, $\eta$, $\rho$ mesons and $\Delta$ resonances at the Nuclotron energies. New putting-up of the precise experiment is necessary. A long base ($\sim$ 50 m) would guarantee precise measurements of moments and angles of both identical particles.

**2.2. Resonance Production in Nuclear–Nuclear Interactions at 4.2 $A \cdot$ GeV.** Middle numbers of positive and negative mesons produced in carbon–carbon interactions are nearly two and seven times correspondingly greater than the ones, produced in proton–proton interactions. Usually the increase of the charged particle multiplicity, particularly $\pi$ mesons, happens due to the plenty of resonances. They are effectively produced, apparently in all types of interactions considered here. So, the observation of abundance of a small $\pi$-meson $p_t$ momentum confirms this approval [15].

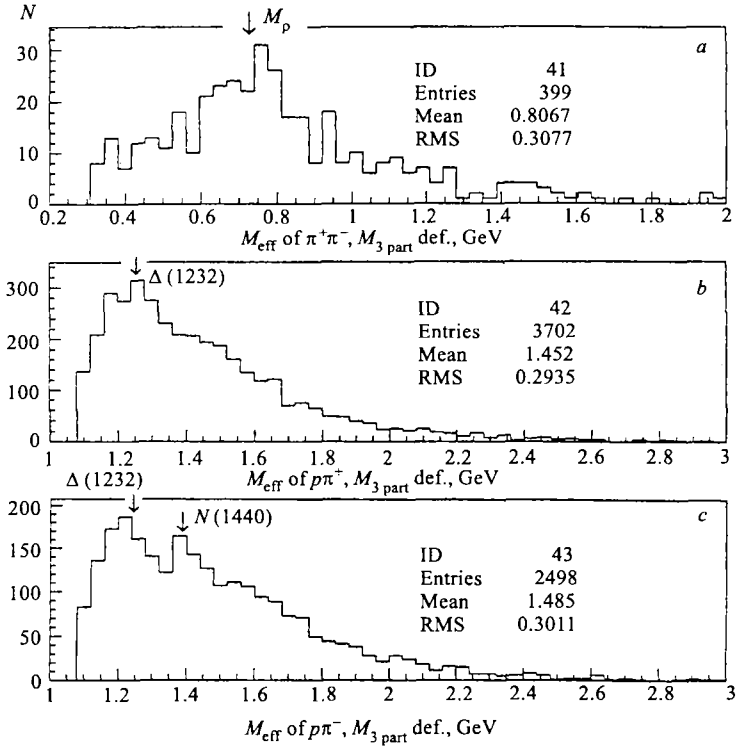


Fig. 8. Effective mass distributions for $pp$ quasi-interactions shared out from C-$C_3H_8$ interactions on the base of $M_t$ spectrum and of summary charge of all produced particles analysis. *a*) $M_{\pi+\pi-}$; *b*) $M_{p\pi^-}$; *c*) $M_{p\pi-}$. The meaning of the $M_{3\text{part}+}$ restriction consists in the following: all two-particle effective mass values coming from three-particle combinations «decays» having the effective mass less than minimal mass (the boundary for the «correspondent reaction») are rejected. The «correspondent reaction» is the reaction which produces the resonance being searched for

The spectra of effective-mass $\pi^+\pi^-$ mesons and $p\pi^+$ particles indicate the presence of the $\Delta^+$ isobars and, maybe, of $\rho$ mesons in $d$C interactions. They disappear, however, in CC and CTa interactions with high charge particle multiplicity entirely (Fig. 7). Here the combinatorial background prevented to observation of the resonances. To reduce the number of bad combinations, the analysis of many-particle effective-mass spectra was applied [16]. In this case, as is seen from Figs. 8, 9, the situation improves significantly.

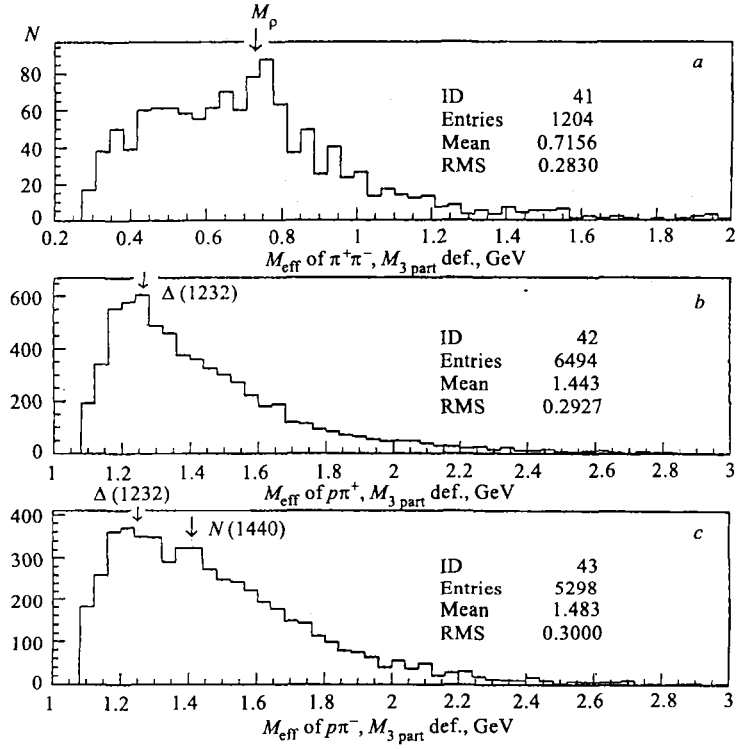


Fig. 9. Effective mass distributions for CC interactions at 4.2 $A \cdot$ GeV/n. See description of Fig. 8 for details

## CONCLUSION

In consequence of some expounded speculations we can conclude that the hypothesis on the presence in the nucleus of the objects other than nucleons, which can serve as the target, has some confirmation. At 4.2 GeV/c/nucleon the results for CC interactions do not contradict the following evidence: initial nuclear collisions between particles, having a mass less than the nucleon one, may happen in a large part ($R \sim 20\,\%$) of all events. Many known resonances or particles and, possibly, quarks can be used as the target. Separate groups of such events are clearly seen.

The production of the so-called cumulative particles [1] can be explained by the interaction of the incident particle with heavy resonances. Heavy resonances have the great binding energy, and it may change its mass in rather wide boundaries.

The testing of the second hypothesis — resonance production suppressing in nuclear–nuclear interaction — has not obtained full confirmation.

But, the $\Delta(1232)\,P_{33}$ and $N(1440)\,P_{11}$ isobars and $\rho$ mesons are produced in the CC and CTa interactions with the same intensity as in nucleon–nucleon interactions. Hence it follows that some suppression exists, particularly for more «central» events (with high $N_{\mathrm{part}}$).

The nature of this suppression is not clear so far. It is known that the secondary interactions may suppress resonances not more than by 20–30 %. It is necessary to perform a more detailed study of this problem. Probably, the resonance matter model with anomalously high cross sections of the interaction between constituents in superdense matter will help to perform it. However, obviously the development of such researches requires to enlarge statistics.

**Acknowledgements.** The authors are grateful to Dr. E. N. Kladnitskaya and O. V. Rogachevsky for assistance in discussions and comments.

We would like to thank Prof. V. G. Kadyshevsky and Prof. A. I. Malakhov for helpful discussions.

We are much indebted to LHE Propane Bubble Chamber Collaboration, who presented the experimental data for testing.

## REFERENCES

1. *Baldin A. M.* // Proc. of Intern. Conf. on Extreme States in Nuclear Systems, Dresden, 1980. V. 2. P. 35;
   *Litvinenko A. G., Malakhov A. I., Zarubin P. I.* // JINR Rapid Commun. 1993. No. 1[58]. P. 27.
2. *Hung C. M., Shuryak E. V.* // Phys. Rev. Lett. 1995. V. 75. P. 4003;
   *Nikonov E. G., Toneev V. D., Shanenko A. A.* // Phys. Rev. of At. Nucl. 1999. V. 62. P. 7.
3. *Brown G. E., Rho M.* // Phys. Rev. Lett. 1991. V. 66. P. 2720.
4. *Sorge H. et al.* // Phys. Lett. B. 1990. V. 243. P. 7.
5. *Pang Y., Sclagel T., Kahana S. K.* // Phys. Rev. Lett. 1992. V. 68. P. 2743.
6. *Metag V.* // Nucl. Phys. A. 1998. V. 638. P. 45.
7. *Bass S. A. et al.* // Phys. Lett. B. 1994. V. 335. P. 289.
8. *Yeis S. et al.* // Z. Phys. A. 1997. V. 356. P. 421.
9. *Birger N. G., Smorodin Yu. A.* // JETF. 1959. V. 37. P. 511 (in Russian).
10. *Agakishiev G. N. et al.* // Yad. Fiz. 1984. V. 40. P. 1209;
    *Armutliiski D. et al.* // Z. Phys. A. 1987. V. 328. P. 455;
    *Simic L. J. et al.* // Phys. Rev. D. 1986. V. 34. P. 692.
11. *Bondarenko A. I. et al.* JINR Commun. P1-98-292. Dubna, 1998.
12. *Lednitsky P., Podgoretsky M. I.* JINR Commun. P2-12302. Dubna, 1979.

13. *Grassberger P.* // Nucl. Phys. B. 1977. V. 120. P. 221–230.

14. *Penev V. N., Chklovskaya A. I.* JINR Commun. E1-2001-149. Dubna, 2001.

15. *Hong B. et al.* (FOPI-Collaboration) // Phys. Lett. B. 1997. V. 407. P. 115–122.

16. *Penev Vl., Shklovskaia A. I.* JINR Commun. E1-2002-172. Dubna, 2002.

Received on April 27, 2002.

Письма в ЭЧАЯ. 2002. №4[113] Particles and Nuclei, Letters. 2002. No.4[113]

УДК 539.171.115

# EXPERIMENTAL RESEARCH OF THE *NN* SCATTERING WITH POLARIZED PARTICLES AT THE VdG ACCELERATOR OF CHARLES UNIVERSITY. PROJECT «*NN* INTERACTIONS»

*N. S. Borisov* [a], *J. Brož* [b], *J. Černý* [b], *Z. Doležal* [b], *A. N. Fedorov* [a], *G. M. Gurevich* [c], *M. P. Ivanov* [b], *P. Kodyš* [b], *P. Kubík* [b], *E. S. Kuzmin* [a], *A. B. Lazarev* [a], *F. Lehar* [d], *A. A. Lukhanin* [e], *V. N. Matafonov* [a], *A. B. Neganov* [a], *I. L. Pisarev* [a], *Yu. A. Plis* [a], *S. N. Shilov* [a], *J. Švejda* [b], *A. I. Tsvetkov* [b], *Yu. A. Usov* [a], *I. Wilhelm* [b]

[a] Joint Institute for Nuclear Research, Dubna

[b] Institute of Particle and Nuclear Physics, Charles University, Prague

[c] Institute for Nuclear Research, Russian Academy of Sciences, Moscow

[d] DAPNIA, CEA/Saclay, France

[e] Kharkov Institute of Physics and Technology, Kharkov, Ukraine

The purpose of the project is to study three-nucleon interactions using 14–16 MeV polarized neutron beam in conjunction with polarized deuteron target. Spin-dependent total cross-section differences $\Delta\sigma_L$ and $\Delta\sigma_T$ will be measured in the energy range, where there are no experimental data, with sufficient accuracy to check the contribution of the three-nucleon forces. In the test run, the obtained deuteron vector polarizations were $P_- = (-39.5 \pm 2)\,\%$ and $P_+ = (32.9 \pm 2)\,\%$. The proposed experiment is the continuation of the preceding measurements of the same quantities in the $np$ scattering at the Van de Graaff accelerator of Charles University.

Целью проекта является изучение трехнуклонных взаимодействий с использованием поляризованного нейтронного пучка с энергией 14–16 МэВ совместно с поляризованной дейтронной мишенью. Спинзависящие разности полных поперечных сечений $\Delta\sigma_L$ и $\Delta\sigma_T$ будут измерены в области энергий, где нет экспериментальных данных, с точностью, достаточной для проверки вклада трехнуклонных сил. В методическом сеансе были достигнуты значения векторной поляризации дейтронов $P_- = (-39,5 \pm 2)\,\%$ и $P_+ = (32,9 \pm 2)\,\%$. Предлагаемый эксперимент продолжает предшествующие измерения тех же самых величин в $np$-рассеянии на ускорителе Ван-де-Граафа Карлова университета.

## INTRODUCTION

It has now become possible to carry out exact experiments and perform numerical calculations of the Faddeev equation for neutron–deuteron scattering using present-day $NN$ forces [1]. There are theoretical predictions of the Bochum–Cracow group concerning 3N system [2]. It is proposed to measure spin-dependent total neutron–deuteron cross-section differences with both neutron and deuteron polarized ($\Delta\sigma_T$ and $\Delta\sigma_L$) at incoming neutron

energies smaller than $\approx 20$ MeV. In [2] $\Delta\sigma_T$ and $\Delta\sigma_L$ were calculated with four recent $NN$ potentials: AV18, CD Bonn, Nijm I, and Nijm II. As the 3NF, the $2\pi$-exchange Tucson–Melbourn (TM) model [8] was adjusted to the triton binding energy. It was shown that the 3NF change the magnitudes of the longitudinal and transversal asymmetries of the total nd cross sections, and the value of the effect is large enough to be measured. The results of such measurements will form the data basis to test the present 3NF models.

The total cross-section difference ($\Delta\sigma_L$) between parallel and antiparallel configurations of neutron and deuteron spins was measured at TUNL [3] for incident neutron energies of 5.0, 6.9, 8.9, and 12.3 MeV. The data were compared to the theoretical predictions based on the CD Bonn $NN$ potential calculations, with and without the inclusion of the TM–3NF. The authors found that the data were greater by a factor of $\sim 1.5$, and noted that, «given reasonable agreement with other $nd$ observables, a sizable discrepancy between experimental and calculational values would be a large surprise». The origin of this discrepancy with the calculations remains unknown.

The experiment on the $\mathbf{d}p$ elastic scattering has been carried out at $E_{\rm lab} = 270$ MeV in RIKEN [4]. A discrepancy with Faddeev calculations using recent $NN$ forces was found. This discrepancy can be completely removed for the cross-section data and for $A_y^d$, by including the TM–3NF in the calculation. In contrast, the inclusion of the 3NF does not lead to a better description of the $A_{ij}$ data, in comparison with the predictions using $NN$ forces only. These facts clearly indicate deficiencies in the TM–3NF spin-dependence calculations. At RCNP the cross-sections and polarization parameters have been measured for $\mathbf{p}d$ scattering at 250 MeV [5].

It is important to note that the $nd$ scattering is interesting in view of the 3NF effects, as there is no Coulomb interaction, and a direct comparison with a Faddeev type calculation is possible. Such experiment on the backward $\mathbf{n}d$ scattering at $E_{\rm lab}(n) = 250$ MeV was carried out at RCNP [6]. The review of the present situation is contained in paper [7].

The aim of the Project is to study 3N interactions in the final state, using the 14–16 MeV polarized neutron beam in conjunction with the polarized deuteron target (PDT).

We propose to measure $\Delta\sigma_L$ and $\Delta\sigma_T$ in the $nd$ transmission experiment at neutron energies up to 16.2 MeV, where no experimental data exist. The proposed experiment is the continuation of the previous measurements of the same quantities in neutron-proton transmission [9, 10].

## 1. EXPERIMENTAL EQUIPMENT

An apparatus measuring the spin-dependent total cross-section differences has been constructed in Charles University. The set-up used in this experiment includes a tritium target for the polarized neutron production, a collimator, a background protection system, a magnet rotating neutron spins, a polarized deuteron target with the frozen nuclear polarization, and data acquisition equipment.

**1.1. Polarized Target.** The authors of the Project propose to use the existing frozen-spin target [11] for $nd$ spin-dependent experiments used earlier for the $np$ experiment (Fig. 1).

The target includes a stationary cryostat with a dilution refrigerator, a movable magnetic system including a superconducting magnet with a large aperture, a superconducting solenoid,

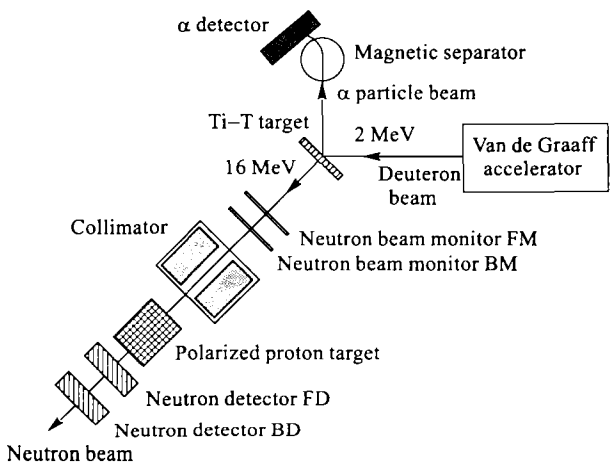


Fig. 1. The layout of experiment

a high-frequency generator providing the dynamic polarization and a NMR-signal detection array.

As target material, 1,2-propanediol $C_3H_8O_2$ (volume 20 $cm^3$) with a paramagnetic Cr(V) impurity was used. The maximum obtained polarization was 93 and 98 % for positive and negative values, respectively. The target was maintained at a temperature of $\sim$ 20 mK in the holding magnetic field of 0.37 T. Under these conditions, the spin relaxation time was approximately 1000 h for positive polarization and 300 h for negative polarization.

The polarization direction is defined by the orientation of the holding field. The experiments with longitudinal polarization are performed with the superconducting solenoid. For the experiments with vertical polarization the superconducting dipole is used.

The target polarization measurement is carried out using a $Q$-meter of Liverpool type with operating frequency of about 17 MHz. An ATT diode generator with output power of $\sim$ 200 mW at a frequency of $\sim$ 75 GHz is used for the dynamic build-up of polarization.

The polarized target was upgraded in order to use deuterated propanediol $C_3D_8O_2$. This target material, in the form of small balls $\approx$ 2 mm in diameter, is placed in a teflon container, 2 cm in diameter and 6 cm long.

The test run was carried out in 2001. The following deuteron vector polarizations were obtained: $P_- = (-39.5 \pm 2)\,\%$ and $P_+ = (32.9 \pm 2)\,\%$ (Fig. 2).

As the nuclear magnetic resonance (NMR) signal from deuterons is much weaker than from protons, it is necessary to accumulate the signals and to use a PC for registration. The

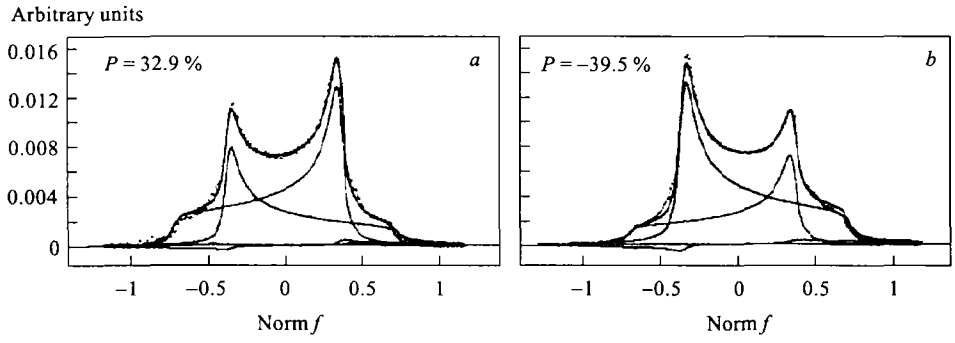


Fig. 2. Deuteron NMR spectra for a positive polarization (*a*) and a negative one (*b*)

upgraded polarization measurement system permits one to measure $\Delta\sigma_T$ and $\Delta\sigma_L$ for the $nd$ scattering and to increase the sensibility for other experiments.

**1.2. Polarized Neutron Beam and Detection System.** As in the previous $\Delta\sigma_{L,T}(np)$ experiments, the exoenergetic two-body reaction $T(d,\mathrm{n})^4\mathrm{He}$ should be used for the neutron production [12]. Unpolarized incident particles provide the transversally polarized outgoing neutrons. Their polarization value $P_n$ depends on kinematic conditions of the reaction.

The Van de Graaff accelerator HV-2500 AN produces the deuteron beam $\sim$ 1 mm in diameter, with the maximum current of 30 $\mu$A at the energy of $(1.820 \pm 0.005)$ MeV. The beam strikes the production target, where tritium was absorbed on Ti, under 45°. The neutrons emitted at the angle $\theta_{\mathrm{lab}} = (62.0 \pm 0.7)^\circ$ have the kinetic energy $E_n = (16.2 \pm 0.1)$ MeV and $P_n = (-13.5 \pm 1.4)\,\%$.

Neutrons, together with $\gamma$ rays, incident on the polarized target, are monitored by two neutron detectors. Two other counters behind the target are used as neutron transmission detectors.

The conjugate $\alpha$ particles, emitted with the energy $E_\alpha = 3.2$ MeV at $\theta_{\mathrm{lab}} = -90^\circ$, together with deuterons elastically scattered at the same angle, pass through the magnetic separator with a field of 0.5 T. They are registered by a silicon surface-barrier detector (8 × 5 mm). The $\alpha$ detector was adjusted to the position corresponding to the desired $\alpha$-particle curvature in the separator magnetic field. It detected only a small amount of scattered deuterons. The tagging of neutrons is obtained by the coincidence of $\alpha$-detector signals with signals from any neutron detector. In addition, for the background reduction, the time-of-flight (TOF) method, with a time resolution better than 2.5 ns, is used. Typically, $2 \cdot 10^4$ neutrons/s in a well collimated beam were obtained.

For the $\Delta\sigma_L$ experiments, the transversal neutron beam polarization is rotated into the longitudinal direction by the permanent magnet, having a field of 1.8 T at the length of 26 cm.

In order to increase the number of events and improve the effect/background ratio, the neutron detectors were upgraded to discriminate against $\gamma$ counts more efficiently. Several liquid scintillator containers with high reflective ability and a reliable atmosphere insulation have been designed and manufactured.

To increase the light collection factor, a method was developed consisting of pure aluminium covering of the container inner surface, with high vacuum evaporation technology. An aging test was carried out of the counter equipped with the new-type container. Good $n/\gamma$ discrimination parameters were observed still after one year of storage. A new movable support was used for the flat liquid scintillation counters, filled with NE-213 scintillator. The neutron beam incident on the polarized target is monitored by two beam detectors. Two other detectors are placed behind the target.

For the signal processing and the data acquisition the CAMAC system was used. This system includes the fast-slow coincidence circuits and the pulse-shape discriminator (PSD). The PCD module was constructed in order to suppress the unwanted $\gamma$ background. This method reduces the background 40 times and enables us to set the neutron signal threshold quite low and to reach a maximum detection efficiency.

**1.3. Minimum Statistics and Estimated Data Taking Time.** For the purpose of this subsection, we treat the simplified case of $\Delta\sigma_{L,T}$ measurement using the vector polarized deuteron target, the beam and target polarizations in one parallel and one antiparallel directions. We set the neutron beam diameter to be smaller than the target diameter. The transmission method for the total cross-section differences needs relative measurements only,

and the knowledge of unique absolute value, i.e., the number of polarizable deuteron per unit of the target cross section.

For $\Delta\sigma_{L,T}$ we find

$$\Delta\sigma_{L,T} = \frac{\ln(\xi(\text{parallel})) - \ln(\xi(\text{antiparallel}))}{\omega P_b P_t}, \tag{1}$$

where $\omega$ is the number of deuterons per unit area of the target; $P_b$ and $P_t$ are the beam and target polarizations, respectively; and $\xi = N_d/N_{\text{mon}}$, where $N_d$ and $N_{\text{mon}}$ are net counts in the detector and monitor.

The statistical error of $\Delta\sigma$ is

$$\delta_{\text{stat}}(\Delta\sigma) = \frac{\sqrt{2}}{\omega P_b P_t}\sqrt{\frac{1}{\bar{N}_{\text{mon}}} + \frac{1}{\bar{N}_d}}, \tag{2}$$

where $\bar{N}_{\text{mon}} = (N_{\text{mon}}(\text{parallel}) + N_{\text{mon}}(\text{antiparallel}))/2$; $\bar{N}_d = (N_d(\text{parallel}) + N_d(\text{antiparallel}))/2$. For $E_n = 16.2$ MeV and D-propanediol $\omega = 3 \cdot 10^{-4}$ mb$^{-1}$, $P_b = 13.5$ %, $P_t = 36$ %, we have $1/\omega P_b P_t = 6.9 \cdot 10^4$ mb.

Demanded values for $E_n = 16.2$ MeV are: for $\Delta\sigma_L\delta = \pm 10$ mb, for $\Delta\sigma_T\delta = \pm 30$ mb.

To get the statistical errors of such values, with $N_{\text{mon}} \simeq N_d = 100$ events/s (considering that the accelerator functions 18 hours/day $\simeq$ 65000 s), it is necessary to have a run of 30 days for measuring $\Delta\sigma_L$ and a run of 4 days for $\Delta\sigma_T$.

For a systematic error of $\Delta\sigma$:

$$\delta^2_{\text{syst}}(\Delta\sigma) = \delta^2_{P_b} + \delta^2_{P_t} + \delta^2_{\omega} + \delta^2_{\text{geom}}, \tag{3}$$

or

$$\delta^2_{\text{syst}}(\Delta\sigma) = (0.104)^2 + (0.05)^2 + (0.03)^2 + (0.01)^2 = (0.12)^2. \tag{4}$$

## 2. PROPOSED POLARIZED NEUTRON SOURCE

It is known that $T(\mathbf{d},\mathbf{n})^4$He is a good source of polarized neutrons for deuteron energies of less than 1 MeV [18]. The notations are taken from paper [18] (Fig. 3). Below approximately 0.5 MeV, the reaction is almost completely described by $S$ wave $J = \frac{3}{2}$ resonance. At scattering angle of 0°, the outgoing $n$ polarization for a deuteron beam polarized along the $y$ axis is given by

$$p_{y'}(\mathbf{n}) = \frac{\frac{3}{2}p_y K_y^{y'}}{1 + \frac{1}{2}p_{yy}A_{yy}}. \tag{5}$$

For pure $J = \frac{3}{2}^+$ interaction, the analyzing power $A_{yy}$ tends to $\frac{1}{2}$ and the polarization transfer coefficient $K_y^{y'}$ tends to $\frac{2}{3}$. If tensor polarization $p_{yy}$ equals zero, $p_{y'}$ tends to $p_y$.

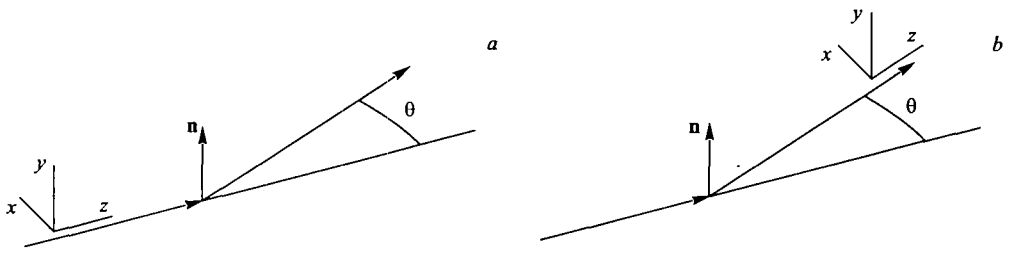


Fig. 3. *a*) Projectile helicity frame; *b*) outgoing reactant helicity frame

If the incident beam is polarized along the $z$ direction,

$$p_{x'} \to \frac{p_z \sin\theta}{1 - \frac{1}{4}(3\cos^2\theta - 1)p_{zz}}, \tag{6}$$

$$p_{z'} \to \frac{\frac{1}{2}p_z \cos\theta}{1 - \frac{1}{4}(3\cos^2\theta - 1)p_{zz}}, \tag{7}$$

$$p_{y'} \to 0. \tag{8}$$

There are severe difficulties in mounting the polarized ion source at the Van de Graaff accelerator. These difficulties are connected with the shortage of space and energy at the high voltage terminal. But it is possible to test the early proposal made by Zavoiskii [13] on the ion polarization, using the capture of polarized ferromagnetic electrons in a thin foil. The first such experiment was carried out by Kaminsky in 1969 [14, 15]. His results were confirmed by Feldman et al. [16].

The success of the experiments made by Kaminsky is related to the use of the channeling through a single crystal foil. The technique investigated here is to direct the incident deuterons in one of the channeling direction of a monocrystalline nickel foil magnetized to saturation.

After passing the weak magnetic field region, the tensor polarization of the well-channeled deuterium atoms (now polarized in electron spin and nuclear spin) can be determined by measuring the angular distribution of the $\alpha$ particles emitted in the reaction $T(d,n)^4$He.

In Kaminsky's experiments the direction of magnetization was parallel to the axes of easy magnetization in the plane of the Ni foil. Saturation is reached at fields of approximately 30 G.

The measured value of $P_{33}$ was $-0.32 \pm 0.01$, which corresponds to a fractional population of $m_I = 0$, $N_0 = 0.440 \pm 0.003$. A beam of 0.5 $\mu$A/cm$^2$ of channeled deuterium atoms was obtained with nuclear spin polarization (without significant lattice damage for $\approx$ 25 h of operating time).

It is possible to produce a relatively cheap polarized neutron source at the Van de Graaff accelerator at Charles University [17] (Fig. 4). The nickel foil should be mounted in the

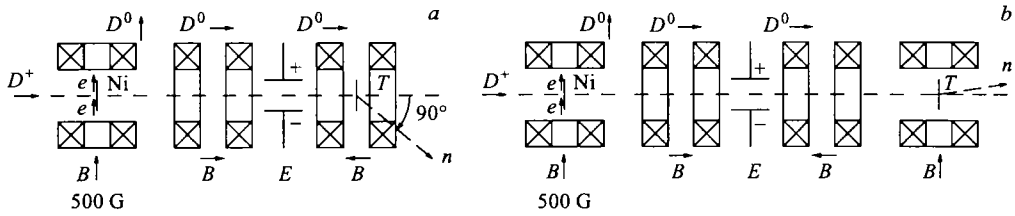


Fig. 4. Polarized neutron production: *a*) transversal horizontal polarization; *b*) transversal vertical polarization

transversal magnetic field of $\approx 500$ G in the plane of the foil. Deuterium atoms with polarized electrons are directed into the longitudinal magnetic field of the same value. The calculations show that the electron polarization adiabatically follows the magnetic field direction. At the length of 50–70 cm, the reversal of the magnetic field takes place (Sona transition method [19]), and the electron polarization is transferred to the deuterons. In the ideal case, the vector polarization should be $p_z = -2/3$ and the tensor polarization $p_{zz} = 0$, where the $z$ axis is in the direction of the magnetic field of the second magnet (e. g., along the beam direction). If the Titanium–Tritium target is mounted in a strong magnetic field, the neutrons produced at the angle of 90° (CM) have the same value of vector polarization, but are transversal in the horizontal plane, in the same way as the primary beam.

It it also possible to rotate the longitudinal vector polarization adiabatically into the vertical direction by the magnetic field of an additional magnet. Then, the neutrons produced at 0° will have, ideally, the vertical polarization equal in value to the deuteron polarization $P_n \approx 2/3$.

As shown in paper [20], the transversal vector polarization of deuterons at an energy of $\approx 200$ keV can be measured using $^2\mathrm{H}(\mathbf{d}, p)^3\mathrm{H}$ reaction. The vector analyzing power of this reaction with 200 keV deuterons at 120° lab angle of $0.224 \pm 0.017$ was measured in paper [21].

Numerical calculations have been carried out using Schrödinger equation for six-component wave function, describing the state of the atom as a superposition of the six states at a high magnetic field, which have a definite nuclear spin.

With the use of data known from the cited papers and the results of calculations, it is possible to expect that the polarized deuteron current may reach 0.5 $\mu$A with an energy of $< 200$ keV and the vector polarization $P_3$ reaching 2/3 and $P_{33} = 0$. These values, if reached, will allow one to upgrade considerably the parameters of the current polarized neutron beam.

The polarization of the neutron beam will be measured using $^4\mathrm{He}(n, n)^4\mathrm{He}$ scattering, where $A_y(\theta)$ reaches the theoretical maximum ($= 1$) (near $\theta = 110°$ and around $E_n = 12$ MeV) and varies slowly with the energy and angle [22].

## CONCLUSION

The Van de Graaff accelerator at Charles University, Prague provides the 16.2 MeV polarized neutron beam. In conjunction with the polarized deuteron target it is possible to measure, for the first time, the observables $\Delta\sigma_{L,T}(nd)$ at this energy.

It is of particular interest to compare the experimental results with the recent phenomenologic predictions for the same quantities, calculated in the neutron kinetic energy interval up to 20 MeV. Such a comparison checks a contribution of the three nucleon forces (3NF) in the final state.

It is proposed to use equipment considerably upgraded with respect to that used in previous $\Delta\sigma_{L,T}(np)$ measurements.

It is planned to reduce the relative errors of measurements from 12 to 5 %, which should help to determine a possible 3NF contribution.

It is proposed to extract polarized deuterons for the production of the neutron beam with an energy of about 14 MeV and to increase its polarization.

**Acknowledgments.** Authors thank E. Tomasi-Gustafsson, M. Yu. Liburg, L. S. Azhgirey, K. Hatanaka, and H. Sakai for their interest and useful discussions, and L. Paukert for the help in the preparation of the paper.

REFERENCES

1. *Glöckle W. et al.* // Phys. Rep. 1996. V. 274. P. 107.
2. *Witala H. et al.* // Phys. Lett. B. 1999. V. 447. P. 216–220.
3. *Foster R. D. et al.* TUNL Progress Report. 2001. V. XL. P. 24.
4. *Sakai H. et al.* // Phys. Rev. Lett. 2000. V. 84. P. 5288.
5. *Hatanaka K. et al.* // Proc. of the 9th Intern. Workshop on High Energy Spin Physics (SPIN 2001), Dubna, 2001. To be published.
6. *Sakai H. et al.* // Ibid.
7. *Sekiguchi K. et al.* // Phys. Rev. C. 2002. V. 65. P. 034003-1-16.
8. *Coon S. A. et al.* // Nucl. Phys. A. 1979. V. 317. P. 242.
9. *Brož J. et al.* // Z. Phys. A. 1996. V. 354. P. 401.
10. *Brož J. et al.* // Z. Phys. A. 1997. V. 359. P. 23.
11. *Borisov N. S. et al.* // Nucl. Instr. Meth. A. 1994. V. 345. P. 421.
12. *Wilhelm I. et al.* // Nucl. Instr. Meth. A. 1992. V. 317. P. 553.
13. *Zavoiskii E. K.* // JETP. 1957. V. 32. P. 408 (English translation: JETP. 1957. V. 5. P. 338).
14. *Kaminsky M.* // Phys. Rev. Lett. 1969. V. 23. P. 819.
15. *Kaminsky M.* // Proc. of the 3rd Intern. Symp. on Polarization Phenomena in Nuclear Reactions, Madison, 1970. The University of Wisconsin Press, 1970. P. 803.
16. *Feldman L. C. et al.* // Radiation Effects. 1972. V. 13. P. 145.
17. *Borisov N. S. et al.* // Czech. J. Phys. 2002. V. 52 (Suppl. C). P. 707.
18. *Ohlsen G. G.* // Rep. Pr. Phys. 1972. V. 35. P. 717.

19. *Sona P. G.* // Energia Nucl. 1967. V. 14. P. 295.

20. *Naqvi A. A., Clausnitzer G.* // Nucl. Instr. Meth. A. 1993. V. 324. P. 429.

21. *Pfaff E. et al.* // Proc. of the 7th Intern. Conf. on Polarization Phenomena in Nuclear Physics, Paris, 1990. Contr. paper 58B.

22. *Fujita T. et al.* // Proc. of the 14th Intern. Spin Physics Symp., Osaka, 2000. AIP Conf. Proc. 2001. V. 570. P. 709.

Received on July 7, 2002.

Письма в ЭЧАЯ. 2002. №4[113] Particles and Nuclei, Letters. 2002. No.4[113]

УДК 539.1.07

# THE FORWARD DETECTOR OF THE ANKE SPECTROMETER. SCINTILLATION AND CHERENKOV HODOSCOPES

*B. Chiladze* [a], *S. Dymov* [b], *R. Esser* [c], *M. Hartmann* [c], *R. Koch* [c], *V. Komarov* [b], *A. Kulikov* [b], *G. Macharashvili* [b], *S. Merzlyakov* [b], *M. Nioradze* [a], *A. Petrus* [b], *B. Rimarzig* [d], *R. Schleichert* [c], *H. Seyfarth* [c], *A. Volkov* [b], *B. Zalikhanov* [b], *N. Zhuravlev* [b]

[a]High Energy Physics Institute, Tbilisi State University, Tbilisi, Georgia
[b]Joint Institute for Nuclear Research, Dubna
[c]Nuclear Physics Institute, Research Center, Jülich, Germany
[d]Central Institute for Nuclear Research, Rossendorf, Germany

The scintillation and Cherenkov counter system of the forward detector of ANKE, magnetic spectrometer at the internal beam of the accelerator COSY in Jülich, is described. The timing and amplitude characteristics are presented as well as the capabilities to select physical processes of interest.

Описывается система сцинтилляционных и черенковских счетчиков переднего детектора ANKE, магнитного спектрометра на внутреннем пучке ускорителя COSY в Юлихе. Приведены их временные и амплитудные характеристики, а также возможности их применения для выделения интересующих физических процессов.

## INTRODUCTION

The experimental facility ANKE [1] is in operation at COSY, the COoler SYnchrotron at the Forschungszentrum Jülich, Germany. It is used for study of proton- and deuteron-induced processes at intermediate energies of up to 2.8 GeV. The ANKE setup (Fig. 1) consists of a three-dipole magnet system installed in the accelerator ring, an internal target and a set of detector groups which select the interaction products in various kinematical regions. One of these groups is the forward detector (FD) which provides detection of fast forward-emitted particles with momenta from 30 to 130 % of the beam momentum in the polar angle range $0° < \phi < 12°$.

The FD acceptance covers a significant part of the phase space of secondaries produced in nuclear interactions at COSY energies. Therefore, being used alone or in coincidence with the other detector groups, the FD allows one to investigate a wide range of processes, including the cumulative deuteron breakup, the $\omega$ and $\phi$ meson production, the subthreshold kaon production and others.

The forward detector comprises a set of fast multiwire proportional chambers and hodoscopes of scintillation and Cherenkov counters. We describe here the design and performance of these hodoscopes used for triggering and particle identification in experiments with ANKE.

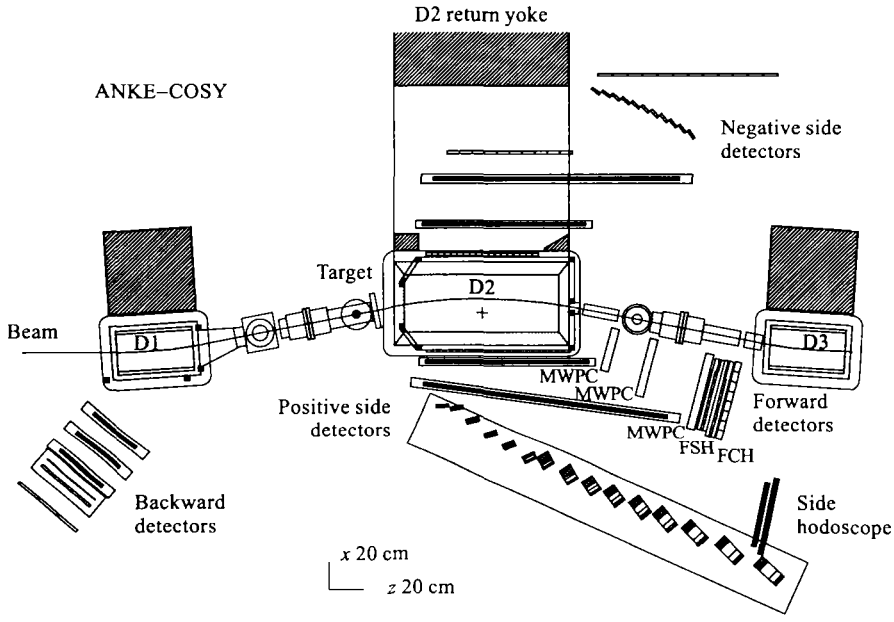


Fig. 1. Scheme of the ANKE setup

## 1. SCINTILLATION HODOSCOPE

The forward scintillation hodoscope (FSH) consists of two planes (A and B) with eight and nine vertically oriented counters in the planes A and B, respectively (Fig. 2). The counters in the plane B are half-width shifted with respect to the A-plane counters. The length of all scintillators is 360 mm, the width is 80 mm for most counters and gradually decreases to 40 mm for the counters in the high-momentum region near the beam pipe, where their occupancy increases. The scintillator thickness is 20 mm for the counters 80 mm wide and 15 mm for the others. The scintillators are viewed from both ends via lightguides with photomultipliers (PM) of the types XP4222 and XP2972 for the 20-mm and 15-mm counters, respectively. The counters, designed as independent units, are assembled on a common frame.

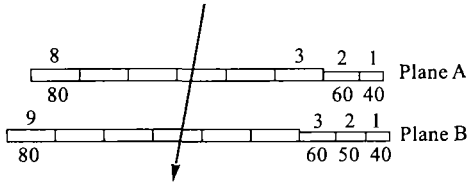


Fig. 2. Schematic top view of the forward scintillation hodoscope. The numbers above the planes are the counter numbers, those below the planes give the widths in millimeters

The front-end electronic channel for each counter (Fig. 3) includes a linear fan-out and a constant fraction discriminator/meantimer (CFD/MT) [2]. Hence, from each counter two analog signals (from the upper and lower PMs) and three logical signals (two from CFDs of the upper and lower PMs and one from MT) are available for further digitization in ADC and TDC and recording as well as for triggering purposes [3].

The time resolution of the counters measured in real beam conditions is in the range $\sigma = 100 \div 150$ ps, the lower value being for the counters with thicker scintillators. This provides the time-of-flight (TOF) measurements if the FSH is used together with one of other detector groups or if two particles hit different counters of the FSH. (As a matter of fact, in both cases not the TOF is measured but the relative timing of two detected particles which may have quite different trajectories. Nevertheless, this delivers information for the off-line particle identification which is equivalent to the TOF.)

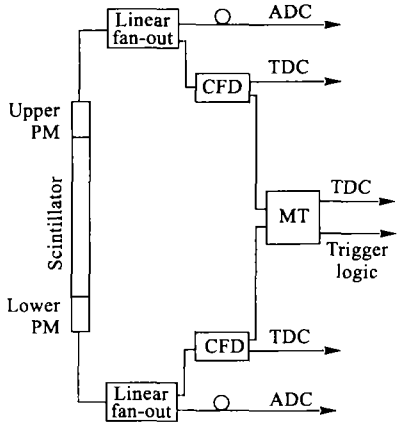


Fig. 3. Scheme of the electronic channel of an FSH counter

Using the timing information from the CFD channels of the upper and lower ends of a counter, one can find the value of the vertical coordinate $y$ of the detected particle. The spatial resolution along the $y$ direction obtained with this method is in the range $\sigma_y = 1.5 \div 2.2$ cm. The accuracy of the $x$-coordinate measurement in the hodoscope is defined by the counter widths. Taking into account the shift between the planes A and B, the uncertainty of the $x$-coordinate is close to a half of the counter width if the both plane signals are used (or slightly more for the inclined tracks). The $x$ and $y$ coordinates obtained in this way are used at the first step of the track reconstruction procedure in the forward detector proportional chambers. The achieved coordinate resolution of the FSH is sufficient to define a limited track search corridor and thus to exclude most of the spurious tracks.

The amplitude information from the FSH is used in the off-line analysis for particle identification and event selection of the processes under study. At intermediate energies the energy losses in the counters depend considerably on the particle type and momentum. For this reason a special amplitude calibration procedure has been developed [4]. The aim of this calibration is to obtain for each counter the relation between the measured amplitude in ADC channels and the real energy losses $\Delta E$ in the units MeV/cm.

The amplitude calibration procedure is the following. Events from several binary processes (i.e., when all the momenta are well defined) are identified and the most probable (m.p.) values of the corresponding peaks in the amplitude distributions are calculated. The processes used are the $pp \to d\pi^+$ reaction at a beam energy of 0.5 GeV with detection of the forward or backward emitted deuteron (in the c.m.s. frame) and the elastic $pp$ scattering at a beam energies of 0.5, 1.0 and 2.0 GeV. The m.p. values can be related to the energy losses in MeV as the particle's type and momentum are defined and hence the energy losses are well known. These sets of the five m.p. values for each counter (independently for the signals of the upper and lower photomultipliers) are fitted with polynomial functions of $\Delta E$, and corrections for the dependence of the amplitude on the coordinate are applied. The final calibration function for a counter is an average of the two functions obtained from independent fits for both counter amplitudes.

In Fig. 4 an example of the energy loss distribution in the counter A-3 and the corresponding counter B-4 is shown. The data were collected for a hydrogen target at a beam energy of 0.5 GeV. Among the three intensive peaks in the spectrum the lower losses correspond to

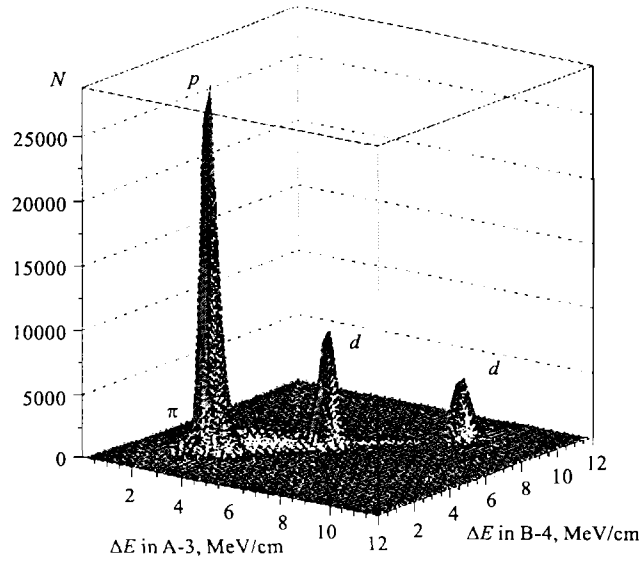


Fig. 4. Energy loss distribution in two matching counters of the scintillation hodoscope measured at a beam energy of 0.5 GeV with a hydrogen target

protons from the $pp$ elastic scattering, while the medium and the rightmost peaks correspond to deuterons from the two kinematical branches of the process $pp \to d\pi^+$ (the forward and backward deuteron emission in the c. m. s. frame, respectively). A small peak at the left of the distribution is due to pions which have lower $\Delta E$. The spectrum contains also the continuum caused by detection of protons from the pion production processes in which the protons are widely distributed over energy. So, the energy loss distribution as a whole reflects fairly well the dominant physical processes for the given conditions. The widths (FWHM) of the peaks in the $\Delta E$ distribution vary from 11 to 17 % for deposited energies from 9.6 to 2.8 MeV/cm, respectively.

## 2. CHERENKOV HODOSCOPE

Cherenkov counters in the forward detector help to distinguish between the particles of different velocities, especially in the high-momentum region where $\Delta E$ and TOF methods become less efficient. The counters in the forward Cherenkov hodoscope (FCH) make use of the total internal reflection of the Cherenkov light inside the radiators. The prototype of such counters for ANKE was tested in [5].

The counter radiator made of lucite is oriented at a predetermined variable angle to the direction of the particle flux. Particles of the same momentum but of different masses have different velocities and, as a result, radiate Cherenkov light at different angles. Hence, one can choose the value of the counter inclination angle such that the Cherenkov light for one of the particles leaves the radiator, but for another one, of less mass and hence faster, part of the light is «trapped» inside the radiator due to the total internal reflection and reaches the photomultiplier at the counter end. This is illustrated in Fig. 5 for the case of protons and

deuterons. To absorb any but the total internal reflection light, the radiator is wrapped with a black paper.

The FCH consists of 16 identical counters assembled as two groups placed symmetrically with respect to the median plane of the forward detector (like in Fig. 5). Each counter has a lucite radiator of cross section $8 \times 5$ cm ($w \times t$) and length 30 cm. The counter is viewed by a photomultiplier XP2020 at the radiator end. The inclination angle can be set independently for any counter. The counters are mounted behind the forward scintillation hodoscope on a common supporting frame and cover approximately the same solid angle. For each counter the amplitude and the timing information are measured. The FCH signals are not used for triggering, so the particle identification is made in the off-line analysis.

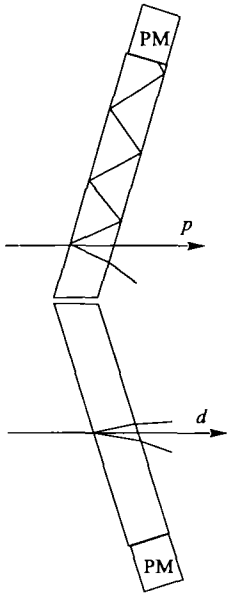


Fig. 5. Cherenkov light propagation in the total internal reflection counters. With a proper inclination angle the light from a deuteron leaves the counter, while part of the light caused by a proton is detected in a photomultiplier

The efficiency of the FCH to protons was investigated in a wide momentum range from 0.5 to 2.7 GeV/c (to cover this range the measurements were done at three beam energies). From these data the efficiency to deuterons can be easily deduced, since deuterons with twice higher momenta have the same velocity as protons and hence radiate the Cherenkov light identically.

The FCH performance with respect to proton/deuteron separation was obtained in an experiment on $\omega(782)$-meson production in the process $pd \to p_{\rm sp} d\omega$ (here $p_{\rm sp}$ is a slow spectator proton) at a beam energy of 2 GeV. The deuterons from this reaction, detected in the FD, have momenta in the range $1.7 \div 2.3$ GeV/c and should be separated from the background of protons. The FCH detection efficiency of deuterons in this momentum interval is equal to that of protons with momenta of $0.85 \div 1.15$ GeV/c. The counters' inclination angle was set at 10°. This angle, according to Monte-Carlo simulation, provides the best separation between the deuterons and protons at these momenta.

Note that the efficiency obtained in the off-line analysis depends on the applied software cut. The Cherenkov counter amplitude is compared with a software threshold and, depending on whether the amplitude is above or below this threshold, the event is classified as «signal is present» or «no signal». For protons the lower the threshold, the higher the efficiency, but simultaneously the efficiency for deuterons increases and the proton/deuteron separation becomes worse. For this reason the threshold is chosen as a reasonable compromise between efficiency and separation capability. The events of the type «signal is present», which include background protons as well as misidentified deuterons, are rejected in the analysis of the experimental data.

The dependence of the proton detection efficiency on the momentum measured with various software thresholds $Q_{\rm th}$ for one of the FCH counters is shown in Fig. 6. For each event the track in the forward detector proportional chambers is reconstructed and the value of momentum is obtained. The efficiency is defined as the ratio $N_{Q>Q_{\rm th}}/N$, where $N_{Q>Q_{\rm th}}$ is the number of entries in the spectrum with an amplitude above the threshold $Q_{\rm th}$ and $N$ is the total number of entries. The efficiency plateau is reached between 1.5 and 1.8 GeV/c

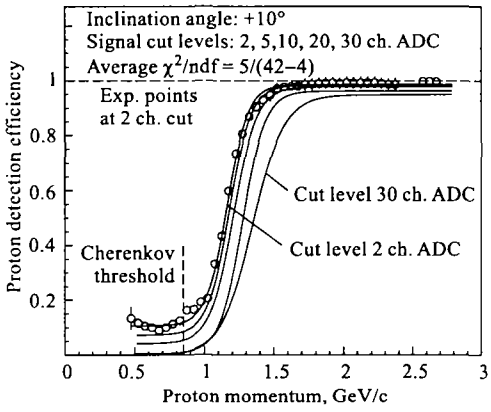


Fig. 6. Proton detection efficiency as a function of the momentum for various values of the software thresholds

and its level varies from 98.6 to 94.8 % for threshold setting between 2 and 30 ADC channels, respectively. This efficiency corresponds to a proton rejection factor from about 70 to 20. The maximum deuteron momentum in the process of the $\omega$ production under study is 2.3 GeV/c, and such deuterons are detected in FCH with the same probability as protons with a momentum of 1.15 GeV/c. Hence, the efficiency to detect deuterons in the whole momentum range $1.7 \div 2.3$ GeV/c is estimated from Fig. 6 to be $\leq 10\,\%$. These deuterons with an amplitude above the threshold are treated as protons and rejected.

The obtained results show that the Cherenkov counters of the forward detector provide a significant suppression of protons at rather small deuteron losses.

## CONCLUSION

The performance of the scintillation and Cherenkov hodoscopes of the forward detector meets the requirements of the experiments at ANKE. The developed procedure for the hodoscope data analysis provides the particle identification and the event selection of the processes under study.

## REFERENCES

1. *Barsov S. et al.* ANKE, a new facility for medium energy hadron physics at COSY-Jülich // Nucl. Instr. Meth. A. 2001. V.462. P.364.

2. *Schleichert R., Selikov A., Seyfarth H.* Development of a constant fraction discriminator and meantimer. IKP Annual Report 1995. Jülich, 1996. P.65.

3. *Dymov S. et al.* Trigger electronics for the forward and backward hodoscopes of ANKE. JINR Commun. E10-2002-19. Dubna, 2002.

4. *Komarov V., Macharashvili G.* Binary process registration in the forward scintillation hodoscope at ANKE. IKP Annual Report 2000. Jülich, 2001. P.21.

5. *Kacharava A. et al.* Beam test of Cherenkov counter prototypes for the ZDF setup // Nucl. Instr. Meth. A. 1996. V.376. P.356.

Received on July 24, 2002.

# ПРАВИЛА ОФОРМЛЕНИЯ АВТОРСКОГО ОРИГИНАЛА СТАТЬИ В ЖУРНАЛ «ПИСЬМА В ЭЧАЯ»

1. *Оригинал статьи* предоставляется автором в двух экземплярах. Необходимо предоставить дискету с текстовым файлом в формате LaTex-2e (не следует вводить свои макрокоманды) и файлами рисунков, таблиц, подрисуночных подписей. Оригинал должен включать все необходимые элементы статьи, иметь сквозную нумерацию страниц и быть подписан всеми авторами.

2. *На первой странице* статьи указывается индекс УДК, название статьи, инициалы и фамилии авторов на двух языках (русском и английском), место работы.

Затем следует *аннотация* на русском и английском языках, включающая характеристику основной темы, цели работы и ее результаты. В аннотации указывают, что нового несет в себе данная статья. Аннотация должна быть краткой, 5–8 строк.

3. *В формулах* все буквы латинского алфавита, обозначающие физические величины, набирают светлым курсивным шрифтом (*E, V, m* и др.). Векторы следует набирать прямым полужирным шрифтом, без стрелок сверху.

Шрифтом прямого светлого начертания набирают следующие обозначения: чисел подобия (Ar, Re и др.); функций (sin, arcsin, sh и др.); условных математических сокращений (max, min, opt, const, idem, lim, lg, ln, log, det, exp) и др.

Латинские буквы в индексах набирают строчным курсивом, кроме сокращений, в том числе и от фамилий (их набирают шрифтом прямого начертания): $f_{abc}$, $\zeta_{xy}$, $G_{\mathrm{Yuk}}$, $\lambda_{\mathrm{eff}}(t,\beta)$, $x_{\max}$. Буквы русского алфавита в индексах используют, когда отсутствуют стандартизованные международные индексы, и набирают строчным шрифтом прямого начертания: $U_{\text{ф}}$ — фазное напряжение; $P_{\text{в}}$ — мощность возбуждения.

Символы химических элементов набирают шрифтом прямого светлого начертания: Cl, Fe.

4. *Рисунки* должны быть четкими и качественными. Желательно, чтобы файл рисунка был подготовлен в формате .eps (Encapsulated PostScript). Не рекомендуется предоставлять цветные рисунки. Рисунки должны быть одного масштаба, их максимальная ширина 13,5 см, максимальная высота 19,5 см (с учетом подписи). Размеры небольших рисунков не должны превышать 7 см по ширине.

Не следует загромождать рисунок ненужными деталями: надписи выносятся в подпись, а на рисунке заменяются арабскими цифрами или буквами. Если рисунок предоставлен на отдельном листе, то необходимо указать фамилии авторов, название статьи и номер рисунка.

5. *Библиографические ссылки* приводят в конце статьи в порядке их упоминания в тексте под рубрикой «Список литературы». Ссылки на неопубликованные работы не допускаются. Ниже следуют примеры оформления:

- книги:
  *Кокорева Л. В.* Проектирование банков данных. М.: Наука, 1998. 241 с.
- статьи из сборника:
  *Быстрицкий В. М. и др.* Исследование температурной зависимости скорости образования мезомолекул $dd\mu$ в газообразном дейтерии // Мезоны в веществе: Тр. Междунар. симпоз. Дубна. 1977. С. 199–205.
- статей из журналов:
  *Афанасьев Ю. В. и др.* Лазерное инициирование термоядерной реакции в неоднородных сферических мишенях // Письма в ЖЭТФ. 1975. Т. 21, вып. 2. С. 150–155.
  *Barbashov B. M., Pestov I. B.* On Spinor Representations in the Weyl Gauge Theory // Mod. Phys. Lett. A. 1997. V. 12, No. 26. P. 1957–1968.
- препринта и сообщения:
  *Тяпкин А. А.* Экспериментальные указания о существовании тахионов, полученные при исследовании черенковского излучения. Препринт ОИЯИ Д1-99-292. Дубна, 1999. 4 с.
  *Muzychka Al. Yu., Pokotilovski Yu. N., Geltenbort P.* Search for an Anomalous Transmission of Ultracold Neutrons Through Metal Foils. JINR Commun. E3-98-18. Dubna, 1998. 10 p.

**Более подробные правила оформления Вы найдете на странице издательского отдела ОИЯИ: www1.jinr.ru**

**Письма о физике элементарных частиц и атомного ядра № 4[113]-2002**

Учредитель и издатель — Объединенный институт ядерных исследований.

Журнал зарегистрирован в Министерстве РФ по делам печати,
телерадиовещания и средств массовых коммуникаций.

Регистрационное свидетельство ПИ № 77-1338 от 10.12.99.

Редакторы: *М. И. Зарубина, Э. В. Ивашкевич, Е. И. Кравченко*
Технический редактор *Е. Н. Водоватова*
Корректор *Е. В. Сабаева*

Подписано в печать 12.11.2002.
Формат 70×100/16. Бумага офсетная. Гарнитура Таймс. Печать офсетная.
Усл. печ. л. 8,29. Уч.-изд. л. 11,03. Тираж 650. Заказ 53615.

Издательский отдел Объединенного института ядерных исследований
141980, г. Дубна, Московская обл., ул. Жолио-Кюри, 6.